SUPPORTING INFORMATION

Structure and Solvation of Confined Water and Water-Ethanol Clusters within Microporous Brønsted Acids and their Effects on Ethanol Dehydration Catalysis

Jason S. Bates†, Brandon C. Bukowski†, Jeffrey Greeley*, Rajamani Gounder*

Charles D. Davidson School of Chemical Engineering, Purdue University, 480 Stadium Mall Drive, West Lafayette, IN 47907, USA.

†J. S. B. and B. C. B. contributed equally to this work.

*Corresponding authors. E-mails: jgreeley@purdue.edu, rgounder@purdue.edu

S.1. Supplementary Methods

S.1.1. Hydrothermal syntheses of zeolites and post-synthetic treatments

Si-Beta-F was synthesized using tetraethylammonium fluoride dihydrate (TEAF) as the structure-directing agent and fluoride source following reported procedures.[1] TEAF (Alfa Aesar, 97%, 5.1 g) was dissolved in deionized water (18.2 MΩ cm, 5.5 g) in a perfluoroalkoxy alkane (PFA) container with a Teflon stir bar. Tetraethyl orthosilicate (TEOS, Sigma Aldrich, 98%, 10.3 g) was added to the PFA container, and the mixture was covered and homogenized overnight at ambient conditions to completely hydrolyze TEOS. Then, the mixture was uncovered until ethanol completely evaporated from the mixture, and some water. Deionized water was added to the mixture to achieve a gel with molar composition 1 SiO_2/0.55 TEAF/6.7 H_2O, and the mixture was transferred into a 45 cm^3 Teflon-lined stainless-steel autoclave and heated to 413 K for 11 days in an isothermal rotating oven (Yamato DKN-402C).

H-Al-Beta-F zeolites were synthesized following the procedure of Camblor et al.[2] TEOS (10 g) was mixed with tetraethylammonium hydroxide (TEAOH, Sachem, 35%, 10.7–11.7 g) in a PFA container and homogenized while covered for 2 h. Aluminum isopropoxide powder ($Al(O\text{-}i\text{-}Pr)_3$, Sigma Aldrich, 98%, 0.03–0.5 g) and excess deionized water (> 10 g) were added to the mixture, which was covered and stirred overnight to completely hydrolyze TEOS and $Al(O\text{-}i\text{-}Pr)_3$. The mixture was uncapped in order to completely evaporate ethanol and isopropanol and partially evaporate water to reach the desired molar ratio. Then, hydrofluoric acid solution (Sigma Aldrich, 48%, 1.1 g) was added and the mixture was homogenized with a PTFE spatula to yield a thick gel with molar composition 1 SiO_2/(0.54+x) TEAOH/(0.54+x) HF/x Al/(7+x) H_2O, where $x = 0.0025$–0.05 to achieve molar ratios of Si/Al = 20–500 in synthesis gels. (Caution: when working with hydrofluoric acid, use appropriate personal protective equipment, ventilation, and other engineering controls.) The gel was loaded into a 45 cm^3 Teflon-lined stainless-steel autoclave and heated to 413 K for 7 days in an isothermal rotating oven.

Al-Beta-OH was synthesized hydrothermally in hydroxide media as reported in the literature.[3] TEAOH (15.1 g) and Ludox HS-30 colloidal silica (Sigma Aldrich, 30%, 20 g) were added to a PFA container and stirred covered for 1 h at ambient conditions. Then, sodium hydroxide (NaOH, Avantor, 98%, 0.11 g) was dissolved in deionized water (4.4 g), and this mixture was added to the gel, followed by Al(O-i-Pr)$_3$ (0.21 g). The gel was stirred covered for 24 h at ambient conditions, then uncovered to completely evaporate isopropanol, and partially evaporate water to achieve the desired molar composition of 1 SiO_2/0.01 Al_2O_3/13.24 H_2O/0.18 TEAOH/0.014 Na_2O. The gel was transferred into a 45 cm^3 Teflon-lined stainless-steel autoclave and heated statically in an isothermal oven at 413 K for 7 days.

As-synthesized zeolites were recovered from synthesis gels by centrifugation, washed thoroughly with deionized water (18.2 MΩ cm) and acetone (Sigma-Aldrich, ≥99.5%), and dried overnight in an oven at 353 K. The dried materials were then treated at 853 K (0.0167 K s^{-1}) for 10 h in air (UHP, Indiana Oxygen, 1.67 cm^3 s^{-1} (g zeolite)$^{-1}$) in a muffle furnace (Nabertherm LE 6/11).

H-Al-Beta-F(0.57) (0.4 g) was exchanged with 1M NaCl (165 g solution (g zeolite)$^{-1}$) for 24 h at ambient temperature in a stirred, sealed PFA container. The final pH of the exchange solution was 3.0. The solid was recovered by centrifugation and washed four times with deionized water (~35 cm^3 per wash), and dried overnight in a 353 K oven. The resulting solid is referred to as Na-Al-Beta-F(0.57).

H-Al-Beta-F zeolites were dealuminated in concentrated nitric acid (HNO_3, Avantor, 69%). The zeolite was added to a PFA container, followed by HNO_3 (25 cm^3 (g zeolite)$^{-1}$), then the container was covered and stirred for 16 h at 353 K. The solids were recovered by centrifugation and washed thoroughly with deionized water until the pH of the supernatant was constant, then dried overnight in a 353 K oven. The Al AAS signal (procedures in Section S.1.4) was below the detection limit for deAl-Beta-F(0.78), consistent with complete dealumination (Si/Al>1500; H^+ u.c.$^{-1}$<0.04).

H-Al-TON (Si/Al = 43) was purchased from ACS Materials (MSZ22H12) and used as-received. H-Al-FAU (Si/Al = 56) was provided by Zeolyst (CBV780) and used as-received. H-Al-MFI (Si/Al = 43) was provided by Zeolyst (CBV8014) and used after liquid-phase NH_4-exchange (1 M NH_4NO_3, ambient temperature, 24 h). The H-Al-CHA sample (Si/Al=15) was synthesized hydrothermally by Di Iorio and Gounder[4] and thoroughly characterized in previous work (SSZ-13(15,0) in Table 1 of Ref. [4]). The H-Al-AEI sample (Si/Al = 9.5) was synthesized hydrothermally by Albarracin-Caballero et al.[5] and thoroughly characterized in that work (H-AEI in Table 2 of Ref. [5]).

Phosphotungstic acid polyoxometalate clusters were supported on Si-MCM-41 (Sigma-Aldrich #643645, 0.98 cm^3 g^{-1} total pore volume) using incipient wetness impregnation. Si-MCM-41 was dried in a 353 K oven prior to use. $H_3[P(W_3O_{10})_4]\cdot xH_2O$ (Sigma-Aldrich #P4006) was dissolved in deionized water to generate a 5 wt% solution. This solution was added dropwise to 1.11 g of dried Si-MCM-41 to the point of incipient wetness (1.15 g solution total). The resulting solid was dried overnight in an oven at 353 K and stored in a vial at ambient conditions prior to use.

S.1.2. X-Ray diffraction

Powder X-ray diffraction (XRD) patterns were collected with a Rigaku Smartlab X-ray diffractometer with a Cu Kα X-ray source in the range of $2\theta = 4–40°$ with a step size of 0.01° and scan speed of 0.005° s^{-1}.

S.1.3. Volumetric N_2 and H_2O adsorption isotherms

N_2 and H_2O adsorption isotherms were collected on a Micromeritics ASAP 2020 instrument. Samples were pelleted and sieved to retain 180–250 μm aggregates, and 0.010–0.040 g were degassed by heating to 393 K for 2 h then 623 K for 10 h under dynamic vacuum (<0.67 Pa) before adsorption measurements. N_2 adsorption isotherms were collected at 77 K by immersion in a liquid N_2 bath, and H_2O adsorption isotherms were collected at 283–302 K by immersion in a recirculating chiller bath held at 283–302 K. H_2O was introduced from the vapor phase generated from a flask held at 313 K containing deionized water, after degassing by three freeze-pump-thaw cycles. N_2 micropore volumes were determined at the uptake corresponding to the minimum value of $\partial V_{ads}/\partial \log(P/P_0)$.

S.1.4. Atomic absorption spectroscopy and inductively coupled plasma optical emission spectrometry

The bulk mass fraction of Al in zeolite samples was obtained by atomic absorption spectroscopy (AAS). 0.03 g of powder were digested with 2 g of HF (Sigma Aldrich, 48%) overnight, then diluted with 50 g of deionized water. Calibration standards were prepared by diluting a stock solution (Sigma Aldrich, 1000 ± 4 ppm Al) with deionized water. A PerkinElmer AAnalyst 300 instrument equipped with a lamp for Al (309.3 nm) was used to measure the absorbance of the standards and digested samples. Si/Al ratios were calculated assuming the unit cell formula of each zeolite.

For ICP-OES, the same digestion procedures were performed, then in addition 1.5 g of HNO_3 (70%, Sigma-Aldrich) were added to the solutions. In some cases, these solutions were further diluted with deionized water to reach the desired concentration range of the calibration standards. ICP-OES measurements were performed on a Thermo Scientific iCAP 7000 Plus Series spectrometer. ICP-OES was used to quantify P (177.5 nm) and W (224.9 nm) in HPW/Si-MCM-41, and the mol POM g^{-1} was assumed to be equivalent to the mol P g^{-1}. Al (309.3 nm) was also quantified by ICP on H-Al-FAU and H-Al-TON. All other reported elemental analyses were performed by AAS.

S.1.5. Temperature-programmed desorption of NH_3

NH_3-TPD was performed on H-Al-Beta samples after aqueous-phase ion-exchange at 353 K with 1 M NH_4NO_3 in deionized water (24 h, 100 cm^3 solution (g zeolite)$^{-1}$). All other zeolite topologies were exchanged at ambient temperature in aqueous 1 M NH_4NO_3 (24 h, 100 cm^3 (g zeolite)$^{-1}$). Zeolites were recovered from ion-exchange solutions by centrifugation and washed thoroughly with deionized water, then dried in a 353 K oven overnight. NH_3-TPD was performed as described by Di Iorio et al.[6] In short, zeolites were supported between two quartz wool plugs within a U-shaped quartz tube, loaded into a Micromeritics Autochem II 2920, and heated in flowing He to 873 K (0.167 K s^{-1}). The NH_3 evolved was detected using an Agilent 5975C mass selective detector, and quantified by the m/z = 17 signal, after correction for the contribution from water present in a constant proportion to its signal at m/z = 18. A pulse of Ar (m/z = 40) was used as an external standard for calibration to correct for drift in the MS signal over time.

S.1.6. Infrared spectra of H_2O adsorbed within zeolites

Infrared spectra of H_2O adsorbed within zeolites were collected as a function of relative pressure (P/P_0 = 0.1–0.75) using procedures described previously.[7,8] Spectra were collected at 293 K on a Nicolet 4700 spectrometer using a quartz cell and heated block assembly[9] described in our prior work.[7,8] Si-Beta-F, H-Al-Beta-F, and deAl-Beta-F zeolites (0.020–0.050 g) were pressed into self-supporting wafers with a 0.9 cm radius, loaded into the IR cell, and pretreated in flowing dry air (<1 ppm of CO_2, 200 K water dew point, Parker Balston, 18–45 cm^3 g^{-1} s^{-1}) to 823 K (0.083 K s^{-1}) for 1 h, then cooled in flowing He (UHP, Indiana Oxygen, 18–45 cm^3 g^{-1} s^{-1}) to 293 K. Temperature was controlled at 293 K by flowing H_2O at 288 K through channels in the block with a recirculating chiller, and resistive heating.

A spectrum was collected of the wafer at 293 K under flowing He (18–45 cm^3 g^{-1} s^{-1}) to be used as a reference before H_2O adsorption. Then, the same He flow was redirected through a heated (>363 K) line connected to a glass syringe (1 cm^3, Hamilton) containing deionized water. Transfer lines after the syringe leading to the cell were heated to >363 K to prevent condensation. The flow rate of the liquid H_2O was controlled via syringe pump (KD Scientific Legato 100) to give an H_2O pressure of 0.2 kPa (P/P_0 = 0.1, 293 K). Care was taken to slowly introduce the liquid H_2O through the dead volume (~20–100×10^{-3} cm^3) connecting the syringe to the line to prevent exposing the wafer to a H_2O partial pressure higher than 0.2 kPa. Spectra were collected continuously (600 s per scan), and the wafer was held at 293 K in the 0.2 kPa H_2O stream for 4 h after H_2O introduction to ensure equilibration, which was verified by invariant spectra collected at the end of this time period. The H_2O flow rate was adjusted to give partial pressures of 0.5 kPa, 1.2 kPa, and 1.7 kPa, corresponding to P/P_0 = 0.2, 0.5, and 0.75 (at 293 K), and 2 h were allowed at each condition for equilibration (verified by invariant spectra). This procedure was first performed with an empty cell to obtain signals for gas-phase H_2O at each P/P_0 value. A background spectrum of the empty cell before H_2O introduction was used as the reference for all other collected spectra. The processing of spectra to give the signal for adsorbed H_2O, and any changes to the vibrations associated with the zeolite, is illustrated in Figure S37.

Spectra were collected in separate experiments at 373 K on a Bruker Vertex 70 spectrometer using a low-dead-volume cell developed by Ribeiro and coworkers.[10] Self-supporting wafers of H-Al-zeolites (0.015–0.030 g) were loaded into a 304 stainless-steel sample holder with a 1.5 cm diameter hole through the center to allow the IR beam to pass through, and gas inlet and outlet channels that direct flow over the wafer. The sample holder is loaded within the cell body, followed by a retainer ring and CaF_2 window. A custom-made graphite ferrule placed around the window in contact with the retainer ring is held in place by a ferrule backer with 8 screws tightened with a torque screwdriver to 14 in lb_f. The same CaF_2 window-ferrule-backer assembly completes the seal on the reverse side of the cell. The cell is housed within an aluminum block equipped with cartridge heaters, and a thermocouple within the cell in contact with the sample holder is used for temperature control. Wafers were pretreated in flowing N_2 (UHP, Indiana Oxygen, 22–44 $cm^3\ g^{-1}\ s^{-1}$) to 573 K (0.083 K s^{-1}) for 1 h, then cooled to 373 K (0.033 K s^{-1}). All transfer lines before and after the cell were heated to >383 K to prevent H_2O condensation. Two three-way valves were switched to redirect the N_2 flow through lines connected at a tee to a 50 cm^3 syringe containing liquid H_2O, which was infused by syringe pump (Legato 100) to give a pressure of 10 kPa H_2O. The flow rate was adjusted to give pressures of 20, 50, and 75 kPa H_2O, and equilibration times, collection, and processing of spectra were identical to those described at 293 K. In some experiments, lower H_2O pressures were initially equilibrated over the sample (1–

2 kPa). In a separate experiment, C_2H_5OH/H_2O mixtures were also loaded into the syringe while feeding the same H_2O pressures (C_2H_5OH/H_2O = 0.005 (10, 20 kPa H_2O) and 0.03 (50, 75 kPa H_2O))).

S.1.7. Ethanol dehydration kinetics

Zeolites (0.020–0.199 g) were pelleted, crushed, and sieved to retain aggregates between 180–250 μm, and supported between two plugs of acid-washed quartz wool (W.R. Grace, washed with 1 M HNO_3 at ambient temperature for 16 h) within a tubular quartz reactor (7 mm i.d.). Zeolites were pretreated in flowing 5% O_2/He (UHP, Indiana Oxygen, 16.67 cm^3 (g zeolite)$^{-1}$ s^{-1}) at 773 K (0.0833 K s^{-1}) for 4 h, then cooled to reaction temperature, typically 373 K (0.0333 K s^{-1}), in flowing He (UHP, Indiana Oxygen, 16.67 cm^3 (g zeolite)$^{-1}$ s^{-1}). The HPW/Si-MCM-41 sample was heated to 373 K (0.0833 K s^{-1}) in flowing He (11.26 cm^3 g^{-1} s^{-1}) prior to reaction. Liquid C_2H_5OH (Sigma-Aldrich, anhydrous, >99.5%) and deionized water were loaded into glass gastight syringes (1 cm^3, 10 cm^3, 50 cm^3, Hamilton 1000 series) and fed via syringe pumps (KD Scientific Legato 100) into separate He streams (heated lines >383 K) flowing at approximately equal rates, and mixed at a tee upstream of the reactor. Reactant and product concentrations were measured by a gas chromatograph (Agilent 6890) equipped with a capillary column (HP-PLOT-Q, 30 m × 530 μm × 40 μm) and flame ionization detector. Diethyl ether was the only product detected under all conditions. Prior to reaction, the composition of the feed stream was verified from bypass injections while the zeolite was held in flowing He (16.67 cm^3 (g zeolite)$^{-1}$ s^{-1}) at reaction temperature for 1 h. The pressures of C_2H_5OH (2×10^{-3}–10 kPa) and H_2O (0–75 kPa) were varied non-systematically over the course of the experiment. A period of 4–12 h was allowed at a given condition to reach a steady state, as verified by measured rates that did not systematically increase or decrease with time-on-stream. Reported rates represent an average of values over at least 1.5 h at steady state. No deactivation was detected over the course of kinetic measurements (~7–21 days), verified by periodically returning to a reference condition (5 kPa C_2H_5OH, 50 kPa H_2O).

At the end of kinetic measurements on H-Al-Beta, H-Al-FAU, and HPW/Si-MCM-41 catalysts, H^+ were titrated *in situ* with 2,6-di-*tert*-butylpyridine (DTBP, Sigma-Aldrich, ≥97%) at 378 K. A solution of C_2H_5OH and deionized water with a C_2H_5OH/H_2O molar ratio of 5 was fed to the catalyst in flowing He to reach a measured steady-state rate at 5 kPa C_2H_5OH and 1 kPa H_2O. Simultaneously, a second feed stream was prepared in lines bypassing the reactor containing the same C_2H_5OH and H_2O pressures, and additionally $0.5–2\times10^{-3}$ kPa of DTBP titrant. Prior to reaching steady-state in the reactor, the composition of the DTBP-containing stream was verified with GC injections. The pressure drop in the DTBP-containing stream was equalized with that of the reactor-to-GC stream with a metering valve in the bypass line. After reaching steady-state, the DTBP-containing stream was introduced to the reactor by switching a multi-position valve, and the cumulative uptake of DTBP was quantified by its disappearance relative to its measured bypass concentration while simultaneously quantifying the diethyl ether formation rate. After suppression of measured rates, the irreversibility of titration was confirmed by observing no recovery of measured rates or desorption of DTBP after returning the DTBP-free stream to the reactor. A titration was also performed at 0.7 kPa C_2H_5OH and 30 kPa H_2O on H-Al-Beta-F(2.0) by the same procedure, using liquid feeds of different composition.

S.1.8. Gas-phase DFT

Beta unit cells were obtained from the International Zeolite Association (IZA)[11] and their lattice constants were relaxed before substituting Al into the framework to simulate the strain exerted by higher Si/Al ratios. Optimized lattice constants have cell volumes within 2% of the IZA values. The Image Dependent Pair Potential pre-optimizer was used to generate an initial guess that includes center of mass rotations,[12] which we have shown to be important within microporous voids.[13,14] The Lanczos diagonalization method was used once a partially converged NEB was obtained, which converges more quickly in microporous voids. All reactants and transition states have been corrected for their zero-point vibrational energy. These calculations were performed using the partial Hessian approach where the lattice was constrained. We have previously shown that even at high coverages of water in Sn-Beta the zero point vibrational frequencies do not shift significantly.[8]

To aid in the identification of lowest-energy configurations for adsorbates, AIMD simulations of some reactive intermediates was performed in the NVT ensemble using a Nosé–Hoover thermostat at 373 K for a duration of 1–2 ps. Images with lower total energies were extracted from the trajectories and force-minimized to obtain more stable conformations. These simulations indicated that adsorbates in H-Al-Beta have large diffusion distances related to their interactions with the proton. The Bader method[15] was used to calculate partial charges.

S.1.9. Ab initio molecular dynamics

In AIMD simulations, all hydrogen atoms were deuterated. The pseudopotentials, energy cutoff, unit cell parameters, and K-point grid were the same as in the gas-phase calculations. The potential energy and temperature of the systems were monitored and found to fluctuate normally around the mean temperature and energy (representative temperature and total energy plots are included in Figure S70). The entropy of solvated water molecules was more complicated than reported previously in Sn-Beta.[75] The acidic proton could transfer among water molecules, preventing the participation of individual degrees of freedom for each water molecule. This was performed with a python code that detects which water molecule is a hydronium, and then removes the hydrogen with the longest O-H bond length from the simulation. At most, only one proton exists in the simulation, so each water molecule is scanned to find the hydronium ion, and only proton can be removed. To calculate whether H^+ was solvated within clusters during simulations, H^+ within 1.10 Å of a framework oxygen was considered coordinated to the framework. This distance requirement accounts for the characteristic AlO-H distance obtained by DFT and includes O-H bond elongation during vibration.

S.1.10. Metadynamics

The collective variables were defined so that at the transition state both C-O bond distances would be nearly equivalent. Both types of C-O bonds are constrained to a maximum bond distance of 5 Å as the primary interest is to study the structure of the transition state, and not an excessively large number of reactant and product states. This maximum bond distance is sufficient to allow for restructuring of solvent around the C-O bonds, which provides space for additional water molecules to participate in the transition states. The choice of collective variables does not bias the mechanism by which C-O bonds are broken and reformed in the simulation, except that the forward and reverse reactions must include the oxygen atoms originally belonging to the ethanol dimer. These parameters were chosen based on test calculations in the gas phase where the approximate width and height of the barriers would ensure the Gaussians provided a slowly varying differential change in the free energy surface to ensure that an approximately canonical ensemble is preserved as the energy of the system is raised to the transition state. Throughout the simulation, 27 total barrier re-crossings were observed, indicating that the potential energy surface was filled to become flat and the algorithm converged.

Analysis of the free energy surface was performed using a python code that maps each Gaussian from VASP into a matrix to be plotted. A modified version of Dijkstra’s search algorithm was used to identify the minimum energy path between basins. The free energy surface was discretized into a graph data structure where points of a specified height are connected to neighboring points. By specifying a range of start and end nodes from basins in the free energy diagram, Dijkstra’s algorithm is a shortest-path tree algorithm that then finds the minimum total energy path to connect the reactant and product basin. Dijkstra’s algorithm can be generalized into higher-dimensional space by increasing the number of neighboring nodes.

It is worth noting that with bond lengths constrained at the transition state, the electronic structure of the system is significantly more difficult to converge at each timestep than for the closed-shell initial and final states further increasing the computational demand of these molecular dynamics simulations.

S.2. Supplementary Discussion

S.2.1. Validity of differential bed assumption in the absence of co-fed water and benchmarking

Figure S12 shows the fractional conversion of C_2H_5OH as a function of site-contact time on H-Al-Beta-F(2.0) and H-Al-Beta-OH(1.7) at 373 K without co-fed H_2O. Because they are not co-fed, both diethyl ether and H_2O gradients are present across the catalyst bed; however, linear dependences of conversion on site-contact time through the origin confirm the differential reactor bed assumption. In other words, varying the site-contact time effectively changes the average concentration of products within the bed, but does not affect the reaction rate because their concentrations are sufficiently small so as not to affect coverage terms in rate expressions. Rates were collected on H-Al-Beta-F(1.2) at values of site-contact time and conversion lower than those verified here as differential, and are therefore also differential. Under these conditions, $P_{H2O,outlet} < 4\times10^{-4}$ kPa. In all experiments with co-fed water, the amount co-fed was in excess of that produced by the reaction, and conversions were <5%, consistent with the conditions of differential operation.

Measured k_3 values ($1.9–2.9\times10^{-5}$ mol (mol H^+)$^{-1}$ s^{-1}, 373 K, Table S1) are also consistent with those measured on an H-Al-MFI zeolite (Si/Al = 43) by Chiang and Bhan[16] (1.7×10^{-5} mol (mol H^+)$^{-1}$ s^{-1}, 368 K), where H^+ are proposed to reside in MFI channel intersections[17–19] whose dimensions (0.64 nm diameter) are similar to those of Beta zeolite channels (0.67 nm diameter). The similar value of k_3 quantified on the same commercially-sourced H-Al-MFI sample used by Chiang and Bhan (3.6×10^{-5} mol (mol H^+)$^{-1}$ s^{-1}, 373 K, Figure S13, SI) provides additional data to benchmark our measurements. Chiang and Bhan also demonstrated that associative dehydration mechanisms prevail in MFI and MOR zeolites because DEE site-time yields (per H^+) were independent of co-fed ethene pressure (0–2 kPa, 388–409 K), which should have facilitated ethoxide-based pathways to form DEE.[16]

S.2.2. Comparison with 1-propanol dehydration at 0.53 and 2 kPa of water

Figure S21 shows the bimolecular ethanol dehydration rate data measured as a function of ethanol and water pressure at 423 K on H-Al-Beta-F(1.2), and directly compares this with bimolecular 1-propanol dehydration to form di-*n*-propyl ether at 423 K on H-Al-MFI reported by Zhi et al.[20] Turnover rates are higher in the case of 1-propanol on H-Al-MFI, likely because the larger 1-propanol dehydration transition state is more effectively stabilized by van der Waals contacts with the confining pore environment than that of ethanol dehydration. Notably, Zhi et al. observed no dependence of turnover rates on co-fed H_2O pressures between 0.53–2.0 kPa; however, the rate data in Figure S21 indicates that the reaction order in 1-propanol ranged between a maximum value of 0.5–0.7 (P_{C3H7OH} = 0.1–0.25 kPa) and a minimum value of 0–0.1 (P_{C3H7OH} = 3–4 kPa), meaning that under all conditions H^+ were partially covered by propanol-propanol dimer species. Under similar conditions, measured bimolecular ethanol dehydration turnover rates were invariant at 0.5 and 2.5 kPa H_2O, and 0.5 kPa C_2H_5OH, consistent with the observations of Zhi et al. Yet, reaching first-order regimes in C_2H_5OH at 2.5 kPa of H_2O required lowering the C_2H_5OH pressure to <0.01 kPa ($P_{C2H5OH}/P_{H2O} < 0.005$). Under conditions where H^+ in Beta zeolites were covered strictly by species involving only one ethanol, rates systematically decreased with increasing H_2O pressure, suggesting that the lack of systematic dependence observed by Zhi et al resulted from partial coverage by alcohol dimers ($P_{C3H7OH}/P_{H2O} > 0.03$) that attenuate the effects of water inhibition, and that such a dependence would be recovered if the P_{C3H7OH}/P_{H2O} ratio was lowered either by decreasing the 1-propanol pressure or increasing the H_2O pressure.

S.2.3. *Assessment of intraparticle transport corruptions*

According to the Madon-Boudart criterion,[21] measured reaction rates are free from transport corruptions when they are independent of active site density, and if the reaction is exothermic, this observation is required at two different temperatures. The latter prescription by Madon and Boudart stems from the expected dependence of the effectiveness factor on the Thiele modulus in the case where intraparticle temperature gradients are present; however, the low reactant conversions measured here (<0.2% between 10–75 kPa H_2O at 373 K on H-Al-Beta-F(2.0)) and mildly exothermic enthalpy of reaction for bimolecular ethanol dehydration to diethyl ether and water (–24 kJ mol^{-1}) make intraparticle temperature gradients unlikely. The values of k_{first} at 373 K on four different H-Al-Beta samples with H^+ densities spanning approximately 1–4×10^{-4} H^+ g^{-1} (as quantified during catalysis by 2,6-di-*tert*-butylpyridine titrations) are shown at water pressures between 10–75 kPa in Figure S19. Under these conditions, where k_{first} values deviate from their expected dependence on water pressure, k_{first} values are invariant with H^+ density, which is consistent with kinetically limited rate measurements as described by the Madon-Boudart criterion.

Intraparticle transport corruptions were further assessed using the Mears criterion.[22] Measured reaction rates are kinetically limited when they are significantly lower than the estimated diffusion rate per catalyst particle:

$$\frac{Rr_p^2}{C_S D_e} < \frac{1}{|n|} \tag{S1}$$

where R is the reaction rate (per particle volume) for an nth order reaction ($R=kC_s^n$), r_p is the particle radius, C_s is the reactant concentration at the external surface of the particle, and D_e is the effective diffusivity of the reactant within the particle. The reaction rate per particle volume is computed using the measured reaction rate per mass, and assuming the framework density of zeolite Beta (15.3 Si (1000 Å^3)$^{-1}$ = 1.53×10^6 g m^{-3}). The particle radius was conservatively estimated as 1.5 μm, because the largest crystallites observed in SEM images of H-Al-Beta-F samples by Camblor et al.[2] were 3 μm in diameter (belonging to a sample with Si/Al = 200, higher Al content samples had smaller crystallites). The surface concentration of C_2H_5OH was assumed to be equivalent to the bulk gas-phase concentration because large aggregates were not present in the catalyst bed (sieved to 180–250 μm aggregates) and thus interparticle gradients are not expected. The effective diffusivity of C_2H_5OH was taken to be 2×10^{-11} m^2 s^{-1}, which was the minimum value calculated in molecular dynamics simulations of 50/50 C_2H_5OH/H_2O mixtures in FAU zeolites at 300 K up to adsorbed densities commensurate with pore filling.[23] This is also a conservative estimate because diffusivities would be higher at 373 K. Taken together, the Mears criterion values calculated with these conservative estimates are <10^{-2} under all water pressure conditions where measured k_{first} values deviated from their expected dependence (>10 kPa H_2O, Figure S20). Thus, these deviations are not a result of transport limitations.

S.2.4. Influence of water on DFT-calculated associative and dissociative ethanol dehydration pathways

The Gibbs free energies (373 K) of adsorbed intermediates and transition states involved in bimolecular ethanol dehydration reaction coordinates were calculated using DFT in the absence of H_2O to validate the assumption that associative dehydration mechanisms prevail under experimental conditions, and with one co-adsorbed H_2O molecule to study its effects on transition state stability. The T9 site was selected as a representative location for Al based on the stability of adsorbed ethanol species (Table S9). The most stable adsorbate configurations were determined by sampling the configurational space at each of the four framework oxygen atoms bonded to the Al site, which at T9 may access both the straight channel and pore intersection environments. The 64 T-atom unit cell used here therefore reflects a simulated Si/Al of 63 (1 H^+ u.c.$^{-1}$), which is representative of the H-Al-Beta zeolites experimentally studied here.

Associative and dissociative DEE formation mechanisms were calculated in H-Al-Beta, following similar approaches to those used in previous studies of ethanol dehydration on Brønsted acidic polyoxometalate clusters.[24] Both associative and dissociative pathways begin with adsorption of gas-phase ethanol to form a hydrogen-bound ethanol monomer at H^+ (E*), with a calculated adsorption free energy of −49 kJ mol^{-1} (Figure S64) The HO-H^+ distance is 1.57 Å with the proton bound to the framework, and the ethanol molecule oriented in the straight channel. In the dissociative pathway, the ethanol monomer eliminates H_2O to form a surface ethoxy group and gas-phase water with an intrinsic activation free energy of 140 kJ mol^{-1} (TS2). At the transition state, the protonated ethanol is oriented toward the intersection, as the C_α-OH elongates to 2.18 Å and the C_α-OAl bond is 2.30 Å, which shortens to 1.53 Å after the ethoxy group is formed at the final state (E_x*, Figure S67). Co-adsorption of a second gas-phase ethanol molecule to form EE_x* (Figure S67) is followed by rearrangement to form DEE with an intrinsic activation free energy of 104 kJ mol^{-1} (TS3). The additional ethanol in EE_x* resides in the channel with a HO-OAl distance of 2.33 Å where the hydroxy group coordinates to an adjacent framework oxygen with no observed interaction with the framework-bound ethoxy group. At the transition state, the adsorbed ethanol attacks the framework-bound ethoxy group (C_α-OH = 2.50 Å), which leaves the framework behind (C_α-OAl = 2.42 Å) to form DEE, and simultaneously the proton of the nucleophilic ethanol is transferred to the framework to recover the Brønsted acid site. The coordination of the ethoxy group to the framework requires the transition state to reside close to the pore walls. Desorption of DEE completes the dissociative catalytic cycle.

In the associative pathway, a second gas-phase ethanol molecule co-adsorbs with the ethanol monomer to form a dimer species (EE*, Figure S64) whose protonated configuration (Bader charge = 0.87 e^-) is consistent with that calculated previously,[25] where the proton is shared between the hydroxyl groups. The presence of protonated dimers has been inferred experimentally by the persistence of Evans windows in IR spectra of ethanol adsorbed on H-Al-MFI and H-MOR up to coverages of 2 per H^+ site.[26] One ethanol molecule is closer to the Al site (OH-OAl = 1.56 Å) and is henceforth referred to as the primary ethanol. The proton-hydroxyl bond length connecting the primary ethanol is 1.05 Å, whereas the proton-hydroxyl bond length connecting the second ethanol is 1.48 Å. This asymmetric sharing was observed for protonated ethanol dimers on POMs,[24] and likely occurs because the charge from the framework polarizes the primary ethanol to a greater extent than the secondary ethanol. The total distance between oxygen atoms in the primary and secondary ethanol molecules across the proton bridge is 2.51 Å. The ethanol-ethanol protonated dimer rearranges to form the S_N2 transition state (TS1) that eliminates water and forms diethyl ether. The protonated primary ethanol reorients linearly within the channel such that a backside attack from the nucleophilic ethanol is sterically unhindered. DEE is formed concurrent with a proton transfer from the nucleophilic ethanol to the framework that regenerates the Brønsted acid site. The bond length between the oxygen of the primary ethanol and its alpha carbon (denoted O^1-$C_\alpha{}^1$) is 2.18 Å, and the bond length between the alpha carbon of the primary ethanol and the oxygen of the second, nucleophilic ethanol (denoted O^2-$C_\alpha{}^1$) is 2.11 Å. The distance between the nucleophile and leaving group for the associative pathway is smaller than that of the dissociative pathway (2.18 Å and 2.42 Å, respectively), as is the distance between the nucleophile and electrophile (2.11 Å and 2.50 Å, respectively). These differences reflect the stabilization of the associative transition state relative to the dissociative transition state because it is not constrained by the bond between framework and ethoxy group. The intrinsic activation free energy for the associative pathway is 125 kJ mol^{-1}, which is 26 kJ mol^{-1} lower than that of the dissociative pathway in the absence of water, when referenced to an ethanol monomer-covered surface. Diethyl ether formation predominantly through associative pathways has been shown previously on H-Al-MFI zeolites,[16] and is consistent with the experimental rate measurements and theoretical calculations shown here.

In summary, associative and dissociative pathways both involve S_N2 transition states that form DEE, but which differ in the identity and flexibility of the nucleophile and electrophile; associative pathways involve reorientation of an adsorbed ethanol monomer to allow sterically unhindered backside attack from the nucleophilic ethanol, while dissociative pathways involve more rigid framework-bound ethoxy groups that undergo attack by an adsorbed ethanol. The geometric constraints imposed by bonding between the zeolite framework and ethoxy group in dissociative pathways result in an intrinsic activation free energy that is 26 kJ mol^{-1} higher than for the associative pathway when referenced to an ethanol monomer-covered surface (Figure S64), consistent with the prevalence of associative dehydration pathways (Figure S11) under the experimental conditions studied (for additional discussion, see Section S.2.5).

In a water-assisted associative pathway, gas-phase water co-adsorbs with the ethanol monomer (E*) to form an ethanol-water dimer species (EW*, Figure S67) with a differential adsorption free energy of +5 kJ mol^{-1}. Ethanol and water form a protonated intermediate similar to EE*, with a Bader charge of 0.84 e$^-$ and a bridging proton that is unequally shared between ethanol and water (H^+-$O(H)C_2H_5$ = 1.02 Å, H^+-OH_2 = 1.54 Å). The ethanol is more closely coordinated to the framework with an OH-OAl distance of 1.47 Å. Adsorption of gas-phase ethanol to form an ethanol-ethanol-water trimer (EEW*) is endergonic (24 kJ mol^{-1}), and this species may form diethyl ether by an S_N2 transition state (TS4, Figure S64) whose structure is similar to that formed without co-adsorbed water (TS1). The additional water molecule stabilizes the H_2O leaving group via hydrogen bonding and acts as a proton shuttle between the framework and the leaving group, but does not alter the S_N2 geometry compared with the H_2O-free case (TS1) whose bond lengths are within 0.02 Å (O^1-C_α^1 = 2.19 Å, O^2-C_α^1 = 2.10 Å in TS4). The proton-shuttling function of the additional water molecule also allows the transition state to reside more distant from the framework Al (C_α^1-Al increases from 3.87 Å to 4.77 Å), which provides additional stabilization through dispersive interactions with the surrounding framework. The intrinsic activation free energy is 73 kJ mol^{-1}, which is an apparent activation free energy of 102 kJ mol^{-1} relative to the ethanol monomer, gas-phase ethanol, and gas-phase water. This apparent activation free energy is comparable to that of the associative pathway with the same reference state (TS1, 114 kJ mol^{-1}), indicating that as H^+ become covered by $(C_2H_5OH)(H^+)(H_2O)_n$ MARI species, corresponding transition states with co-adsorbed H_2O may become kinetically relevant. A mechanistic interpretation of the inhibitory effects of H_2O on ethanol dehydration catalysis therefore requires a more precise description of the coverage regimes that lead to $(C_2H_5OH)(H^+)(H_2O)_n$ intermediates of different molecularity that form diethyl ether without complete desorption of H_2O.

S.2.5. Derivation of the relative rates of dissociative and associative pathways

We derive an expression for the relative rates of dissociative and associative pathways in order to further demonstrate that the dissociative pathways are kinetically irrelevant under the conditions studied here. Refer to Figure S64 for the identity of each intermediate and transition state. The rate of the dissociative pathway is assumed equal to the rate of ethoxy formation:

$$r_{dissoc} = k_d(E^*) \tag{S2}$$

where k_d is the intrinsic rate constant that reflects the free energy of activation (TS2, Figure S64) to form ethoxy from the ethanol monomer. The assumption of Eq. S2 is reasonable because the second step of the associative pathway (TS3) has an intrinsic free energy barrier that is 36 kJ mol^{-1} lower than the first step. The rate of the associative pathway proceeds from ethanol-ethanol dimer species:

$$r_{assoc} = k_a(EE^*) \tag{S3}$$

where k_a is the intrinsic rate constant that reflects the free energy of activation to form the S_N2 elimination transition state (TS1, Figure S64) from the ethanol-ethanol dimer. Assuming quasi-equilibrated adsorption of gas-phase ethanol to form the ethanol-ethanol dimer:

$$r_{assoc} = k_a K_D (E^*) P_{C_2H_5OH} \tag{S4}$$

where K_D is the thermodynamic equilibrium constant to adsorb gas-phase ethanol at the ethanol monomer to form the ethanol-ethanol dimer. Dividing S2 by S4 gives:

$$\frac{r_{dissoc}}{r_{assoc}} = \frac{k_d}{k_a K_D P_{C_2H_5OH}} \tag{S5}$$

The rate and equilibrium constants may be written in terms of the free energies of intermediates and transition states in Figure S64:

$$k_d = \frac{k_B T}{h} exp\left(\frac{-\left(\Delta G°_{TS2} - \Delta G°_{E^*}\right)}{RT}\right) \tag{S6}$$

$$k_a = \frac{k_B T}{h} exp\left(\frac{-\left(\Delta G°_{TS1} - \Delta G°_{EE^*}\right)}{RT}\right) \tag{S7}$$

$$K_D = exp\left(\frac{-\left(\Delta G°_{EE^*} - \Delta G°_{E^*} - \Delta G°_{E(g)}\right)}{RT}\right) \tag{S8}$$

Combining S5 with S6–S8 gives:

$$\frac{r_{dissoc}}{r_{assoc}} = exp\left(\frac{\Delta G°_{TS1} + \Delta G°_{E(g)} - \Delta G°_{TS2}}{RT}\right) P_{C_2H_5OH}^{-1} \tag{S9}$$

where $\Delta G°_i$ are standard-state free energies of component i (kJ mol^{-1}), and the units of P_{C2H5OH} are bar. The values of $\Delta G°_i$ from Figure S64 predict that the rate of the dissociative pathway in the absence of water exceeds that of the associative pathway at P_{C2H5OH}<0.02 kPa (Figure S65); however, the precise pressure at which this transition occurs is subject to error in DFT-calculated free energies which can be on the order of 10 kJ mol^{-1}.[27,28] By analogy, the same relationship as in Eq. S9 exists for the dissociative and associative pathways with one co-adsorbed H_2O molecule shown in Figure S66, whose transition states differ by an amount (25 kJ mol^{-1}) almost identical to the water-free case (26 kJ mol^{-1}), meaning that a similar transition point (0.02 kPa C_2H_5OH) would be predicted with co-adsorbed H_2O.

Considering the reaction orders in ethanol measured experimentally, and the expected prevalent surface coverages brings clarity to the question of the dominant pathway. In either case with or without co-fed H_2O, experimentally, rate data collected under conditions where P_{C2H5OH}<0.02 kPa are approximately first-order in C_2H_5OH, which would reflect either dominant associative pathways with an ethanol monomer-saturated surface, or dominant dissociative pathways with a completely vacant surface. If the adsorption free energy to form an ethanol monomer (E*) is 49 kJ mol^{-1}, as predicted by DFT, then this allows estimating its equilibrium constant:

$$K_{E^*} = exp\left(\frac{-\left(\Delta G°_{E^*} - \Delta G°_{*} - \Delta G°_{E(g)}\right)}{RT}\right) \tag{S10}$$

which gives a value of 7×10^6 at 373 K. Assuming the MARI are (*) and (E*), the coverage of E* is given by:

$$\theta_{E^*} = \frac{K_{E^*}P_{C_2H_5OH}}{1+K_{E^*}P_{C_2H_5OH}} \tag{S11}$$

where K_{E^*} is given by Eq. S9, and P_{C2H5OH} has units of bar. Eq. S11 predicts that H^+ are not vacant under any experimentally-tested condition at 373 K (Figure S65b), but are rather covered by ethanol monomers (E*) or $(C_2H_5OH)(H^+)(H_2O)_n$ species (Figure 4, Main Text). In this case, only associative mechanisms would give first-order kinetics, and so it is concluded that dissociative mechanisms are not kinetically relevant under the conditions of experimental rate measurements (373 K, 2×10^{-3}–10 kPa C_2H_5OH, 0–75 kPa H_2O).

S.2.6. Derivation of the apparent free energies of activation in different coverage regimes

The rate and equilibrium constants in this derivation correspond to those shown in Figure S11, with the adsorbed intermediates abbreviated as: $(C_2H_5OH)_2H^+$ = EE*, $C_2H_5OH\cdots H^+$ = E*, and $C_2H_5OH\cdots H^+\cdots H_2O$ = EW*.

According to transition state theory, k_3 can be written as:

$$k_3 = \frac{k_BT}{h} exp\left(\frac{-\left(\Delta G°_{TS3}-\Delta G°_{EE^*}\right)}{RT}\right) \tag{S12}$$

The adsorption equilibrium constant K_2 is defined as:

$$K_2 = exp\left(\frac{-\left(\Delta G°_{EE*}-\Delta G°_{E^*}-\Delta G°_{E(g)}\right)}{RT}\right) \tag{S13}$$

Combining S12 and S13 gives:

$$k_3K_2 = \frac{k_BT}{h} exp\left(\frac{-\left(\Delta G°_{TS3}-\Delta G°_{E^*}-\Delta G°_{E(g)}\right)}{RT}\right) \tag{S14}$$

which indicates that the value of k_3K_2 reflects the free energy of the confined bimolecular dehydration transition state relative to those of the confined ethanol monomer and gas-phase ethanol. Values of k_3K_2 quantified with co-fed water are systematically 2–4× lower than those quantified in the absence of co-fed water (Table S1). This difference corresponds to apparent activation free energies at 404 K that are 2–4 kJ mol^{-1} higher with co-fed water, which qualitatively seems reasonable because physisorbed water can preferentially stabilize adsorbed alcohol intermediates over dehydration transition states, as suggested by Zhi et al. for 1-propanol dehydration activation enthalpies and entropies measured experimentally with and without co-fed H_2O (413–443 K, 0–2.5 kPa H_2O).[20] Additional variations in values of k_3K_2 among H-Al-Beta samples may also result from different proximity of Si-OH groups to H^+ active sites, which have been reported to stabilize adsorbed water and alcohol intermediates and dehydration transition states to different extents in Lewis acid-catalyzed ethanol dehydration.[13,29]

The adsorption equilibrium constant K_4 is defined as:

$$K_4 = exp\left(\frac{-\left(\Delta G^{\circ}{}_{EW*} - \Delta G^{\circ}{}_{E^*} - \Delta G^{\circ}{}_{W(g)}\right)}{RT}\right) \tag{S15}$$

Combining S14 and S15 gives:

$$k_3K_2K_4^{-1} = \frac{k_BT}{h} exp\left(\frac{-\left(\Delta G^{\circ}{}_{TS3} - \Delta G^{\circ}{}_{EW^*} + \Delta G^{\circ}{}_{W(g)} - \Delta G^{\circ}{}_{E(g)}\right)}{RT}\right) \tag{S16}$$

which indicates that $k_3K_2K_4^{-1}$ reflects the free energy of the confined bimolecular dehydration transition state and gas-phase water relative to the confined ethanol-water dimer and gas-phase ethanol.

S.2.7. H_2O adsorption at Si-OH nests and isosteric heats of adsorption

Silanol nest densities approximately equal to the number of H+ u.c.$^{-1}$ were quantified by the integrated area for ν(OH) peaks of silanol nests in IR spectra (Figure S38), without disruption to their bulk crystalline structure according to similar micropore volume measurements (Table 1, Main Text) and XRD patterns (Figure S1). The non-zero intercept of the correlation of silanol nest ν(OH) peak area with silanol nests per unit cell (Figure S38) indicates that formation of a minority amount of Si-OH defects is unavoidable during fluoride-mediated crystallization of Beta zeolites, which should be taken into account when developing correlations between adsorbed quantities and the silanol nests generated by dealumination. We note that two of the four Si-OH groups generated by Al removal likely condense so that the vacancy consists of a strained siloxane bridge and (Si-OH)$_2$,[30,31] which we refer to collectively as a Si-OH nest. The adsorption isotherm on Si-Beta-F is classified as Type III[32] and indicates weak adsorbate-adsorbent interactions where adsorption occurs by dispersive interactions of H_2O with non-polar siloxane bonds within micropores, and at Si-OH defects.

H_2O adsorption isotherms (293 K) normalized to the number of silanol nests in deAl-Beta-F samples (Figure S32b) show wider variation among samples than observed on H-Al-Beta-F samples, but adsorption behavior is consistent with preferential adsorption at silanol nests at low partial pressures ($P/P_0 < \sim 0.1$) followed by formation of extended hydrogen-bonded water networks.[7,8] This adsorption behavior contrasts the more tightly bound $(H_3O^+)(H_2O)_n$ clusters localized at H^+ sites that form initially in H-Al-Beta-F samples. The proportionality of water uptakes with silanol nest density indicates that the formation of extended hydrogen-bonded networks throughout the crystallite is limited by the density of Si-OH nest defects, in which micropore regions devoid of nest defects that are found in samples with lower defect densities (0.11–0.57 u.c.$^{-1}$) behave as essentially hydrophobic, while higher silanol nest densities (0.78–2.0 u.c.$^{-1}$) lead to hydrogen-bonded water networks that extend throughout crystallites, as indicated by similar water uptakes (per g) at high water pressures ($P/P_0 = 0.9$). These data are consistent with simulations[33–35] and experiments[36] that indicate that the density and spatial distribution of hydrophilic binding sites on hydrophobic surfaces influence the structure and dynamics of water.

The preferential adsorption of H_2O at H^+ and Si-OH nest defects was corroborated by obtaining isosteric heats of adsorption (q_{st}) as a function of coverage from adsorption isotherms collected at different temperatures (283–302 K, Figure S35–Figure S36):

$$q_{st} = -R\left(\frac{\partial lnP}{\partial\left(\frac{1}{T}\right)}\right)_{N_{H_2O}} \tag{S17}$$

where q_{st} is calculated from a plot of -Rln(P) vs. 1/T (K^{-1}) where the P values (kPa) are obtained from adsorption isotherms at a given constant value of H_2O coverage (mol g^{-1}). The calculation of q_{st} relies on the assumptions of reversible adsorption, an ideal gas phase, and negligible molar volume of the adsorbed phase relative to the gas phase.[37,38] The latter two assumptions are typically satisfied at low pressure and low coverage, but caution should be taken when interpreting high-coverage values.[38] On Si-Beta-F (Figure S37), the isosteric heat of adsorption is initially 50–55 kJ mol^{-1} (0.005–0.02 mmol g^{-1}), then rapidly decreases with increasing amounts of adsorbed water, becoming constant (~45 kJ mol^{-1}) above ~0.2 mmol g^{-1}. The initial heat of adsorption of H_2O measured calorimetrically at Si-OH defects present in low densities on an amorphous SiO_2 surface treated to 1073 K was a similar value (54 kJ mol^{-1}, ~0.04 mmol g^{-1}),[39] indicating that the initial q_{st} on Si-Beta-F is consistent with preferential adsorption of H_2O at a minority of Si-OH defect sites within micropores (0.03–0.2 mmol g^{-1}, quantified by CD_3CN IR on Ti-Beta-F zeolites[7]). Adsorption at higher coverages (>0.2 mmol g^{-1}) occurs at extracrystalline locations at higher relative pressures ($P/P_0>0.6$, 293 K)[40] with a q_{st} of ~45 kJ mol^{-1}, consistent with q_{st} values (44 kJ mol^{-1}) on a hydrophobic Si-MFI-F zeolite at similar coverages (0.1–0.2 mmol g^{-1}).[41] Preferential adsorption of H_2O at intracrystalline Si-OH defects is consistent with the perturbation of their ν(OH) IR peak (3735 cm^{-1}) by H_2O adsorption at low P/P_0 values (0.1–0.2) (Figure S40b inset), whereas extracrystalline Si-OH groups (3745 cm^{-1}) are perturbed later (P/P_0>0.2).

In contrast to Si-Beta, the q_{st} for water on de-Al-Beta-F(2.0) (Figure S37) is 82 ± 14 kJ mol^{-1} at low coverage (0.5 mmol g^{-1} = ~1 H_2O per Si-OH nest), in agreement with calorimetrically measured heats of adsorption of H_2O at Si-OH groups on amorphous SiO_2 activated at 423 K (80 kJ mol^{-1})[42] and 473 K (73 kJ mol^{-1}),[39] which indicates that H_2O adsorption occurs preferentially at Si-OH nests in deAl-Beta-F zeolites. The value of q_{st} decreases to 45 kJ mol^{-1} above a coverage of ~3 mmol g^{-1} (~6 H_2O per Si-OH nest), after which adsorption likely occurs by adsorbate-adsorbate interactions energetically similar to those of liquid H_2O (ΔH_{cond} = 41 kJ mol^{-1}), and similar to the value measured calorimetrically on H-Al-MFI zeolites after $(H_3O)^+(H_2O)_6$ clusters are formed (45 kJ mol^{-1}).[43] Calorimetric[43] and isosteric[44] heats of adsorption measured on H-Al-MFI zeolites measure similarly high heats of adsorption at H^+ (~80 kJ mol^{-1}) consistent with preferential formation of $(H_3O^+)(H_2O)$ at coverages between 1–2 H_2O/H^+. Taken together, volumetric adsorption isotherms and heats of adsorption of H_2O indicate that H_2O adsorbs preferentially at low coverages at hydrophilic binding sites (H^+, Si-OH) within hydrophobic zeolite pores, then forms clustered $(H_3O^+)(H_2O)_6$ clusters and extended hydrogen-bonded networks. Measured isotherms provide a quantitative relationship between H_2O coverage and partial pressure that can be further related to the spectroscopic signatures of adsorbed H_2O structures present at different H_2O coverages.

S.2.8. Estimating entropy in AIMD simulations of ethanol and water in H-Al-Beta zeolites

Proton shuttling is facile, which complicates entropy calculations as each proton transfer is a collision causing the angular velocity to be discontinuous in the reference frame of individual water molecules upon accepting or releasing a proton. Therefore, the acidic mobile proton was eliminated in post-processing from each simulation, by defining the proton (which can only be singular in our 1 acid site per unit cell model) as any hydrogen that has the largest O-H bond distance in the system subject to each water molecule oxygen has two bonded hydrogens. This produces a set of molecular trajectories only including water and without necessitating the labeling of protons during the system, allowing for proton shuttling to occur during the simulation without any bias for which hydrogen must behave as a proton. In removing this proton, we are implicitly assuming the entropy of the solvated proton is the same across the water densities we have considered, and not that the proton entropy is formally zero. As the reference state for all ethanol-water mixtures is the solvated pure-water system, all reported energies are relative to a similarly protonated system. As for whether the proton entropy is similar at the range of water and ethanol compositions considered here, we can first acknowledge the proton entropy change will likely be small relative to the change in translational entropy for adsorbate molecules. We can draw some similarities with the electrochemistry field, where the entropies of protons are often neglected.[45]

To estimate the entropy of adsorbate molecules, it must be considered that due to proton solvation, events will occur during simulation where a proton will form a hydronium ion with a finite lifetime, followed by the release of a proton to form water. The proton that forms the hydronium and the proton that is released to form water does not need to be the same atom. Water shuttling mechanisms mean that atoms cannot be labeled as they are in methods such as those used by Goddard which we have used for Sn-Beta and deAl-Beta.[8] This can be remediated in translational entropy treatments by treating the center of mass of each water and ethanol molecule using the method of Alexopoulos et al.[25] Integration of rotational and vibrational degrees of freedom; however, is still made difficult by the proton shuttling events which can instantaneously change the moment of inertia of a water molecule or change the vibrational modes of water molecules. For vibrational degrees of freedom, we have shown in our previous work in Sn-Beta and deAl-Beta that while vibrational frequencies shift with water loading, the contribution to the total entropy is small relative to translation. In addition, the range of water loadings considered here is smaller than that considered in our previous work, and thus the vibrational entropy contributions are considered to be the same across water loadings. We will also assume the change in rotational entropy of adsorbates is the same across water loadings due to the discontinuity of molecular moments of inertia when water shuttling events occur. The consistency of rotational states requires more thought, as it is possible that even with small changes in density the rotational states may change more substantially. The discontinuity in rotation due to proton shuttling presents a complication in evaluating rotational degrees of freedom in the traditional AIMD methods such as the VDOS or non-rigid moments of inertia. One potential technique would be re-scaling of the moments of inertia before the collision, and translating the moment of inertia after each collision back to their initial configuration to smooth the moments of inertia and allow partition function methods for calculating rotational entropies, and we are interested in testing these techniques in the future to more rigorously assign changes in rotational entropy upon solvation. For the present work, as we are considering a narrow range of adsorbate loadings for relatively small molecules, and comparing them to a similarly solvated state, we affirm the present methods are sufficient to quantify changes in water loading upon coadsorption of ethanol molecules, and also contribute to the techniques used to model solvated reacting systems.

S.2.9. Relating $K^{\ddagger}$ to the rate and equilibrium constants for elementary steps

As defined in the main text, $K^{\ddagger}$ reflects the free energy of the transition state and gas-phase water relative to that of $(C_2H_5OH)(H_3O^+)(H_2O)_n$ and gas-phase ethanol:

$$\frac{k_BT}{h}K^{\ddagger} = \frac{k_BT}{h}exp\left(\frac{-\left(\Delta G^{\circ}{}_{\ddagger}+\Delta G^{\circ}{}_{H_2O(g)}-\Delta G^{\circ}{}_{C_2H_5OH(g)}-\Delta G^{\circ}{}_{EW_n}\right)}{RT}\right) \tag{S18}$$

Within the exponential, we can add and subtract the free energies of both EW_{n-1} and EEW_{n-1} intermediates which are formed en route to the transition state in Scheme 1, and group terms together into quantities that can be simplified to the rate and equilibrium constants of elementary steps:

$$\frac{k_BT}{h}K^{\ddagger} =$$

$$\frac{k_BT}{h}exp\left(\frac{-\left(\Delta G^{\circ}{}_{\ddagger}-\Delta G^{\circ}{}_{EEW_{n-1}}\right)}{RT}\right)exp\left(\frac{-\left(\Delta G^{\circ}{}_{EEW_{n-1}}-\Delta G^{\circ}{}_{C_2H_5OH(g)}-\Delta G^{\circ}{}_{EW_{n-1}}\right)}{RT}\right)exp\left(\frac{-\left(\Delta G^{\circ}{}_{H_2O(g)}+\Delta G^{\circ}{}_{EW_{n-1}}-\Delta G^{\circ}{}_{EW_n}\right)}{RT}\right)$$

(S19)

$$\frac{k_BT}{h}K^{\ddagger} = k_3K_2K_4^{-1} \tag{S20}$$

Eq. S20 can then be substituted directly into Eq. 12 in the main text to give:

$$\frac{r_{DEE}}{[H^+]} = \frac{k_3K_2}{K_4}\frac{\gamma_{EW_n}}{\gamma_{\ddagger}}\frac{P_{C_2H_5OH}}{P_{H_2O}} \tag{S21}$$

S.3. Supplementary Figures

S.3.1. XRD patterns

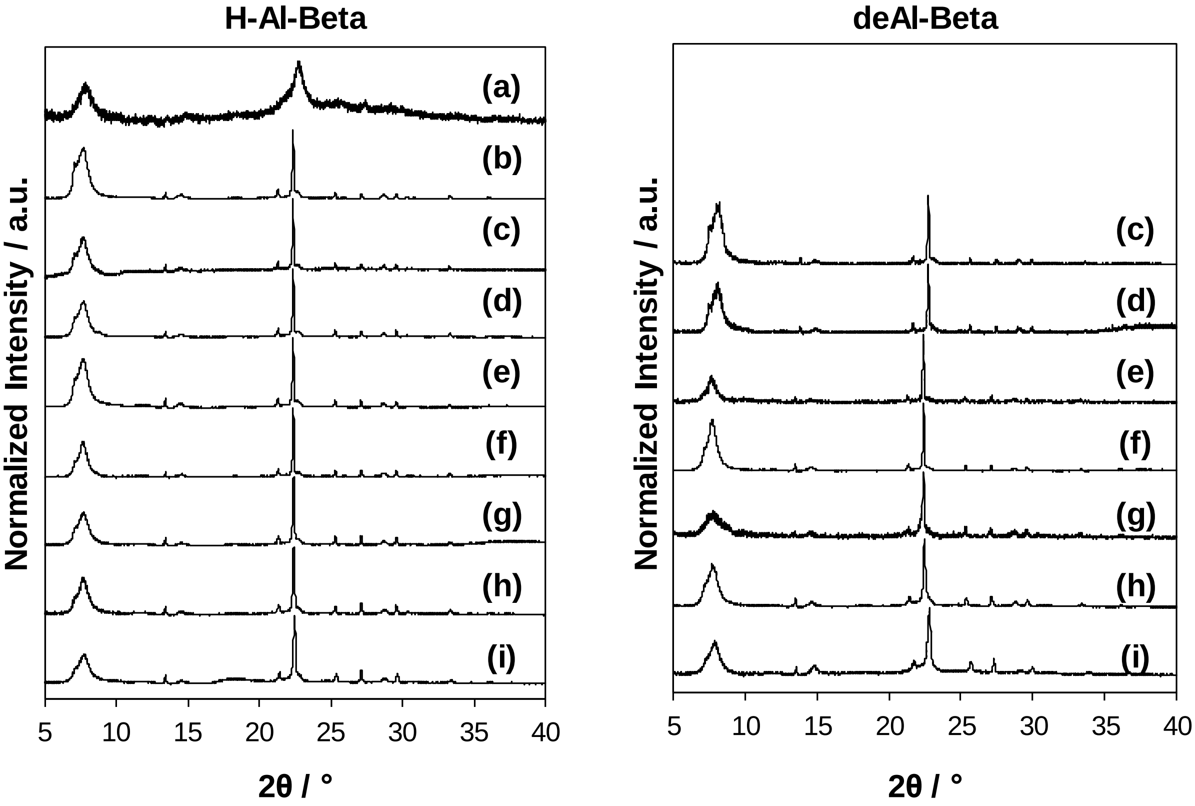

Figure S1. Left: XRD patterns of (a) H-Al-Beta-OH(1.7), (b) Si-Beta-F, and H-Al-Beta-F with H^+ u.c.$^{-1}$ = (c) 0.11, (d) 0.16, (e) 0.57, (f) 0.78, (g) 1.2, (h) 1.4, (i) 2.0. Right: dealuminated analogs (deAl-Beta-F) of the samples at left. All XRD patterns are normalized to their highest peak intensity.

S.3.2. NH_3-TPD data

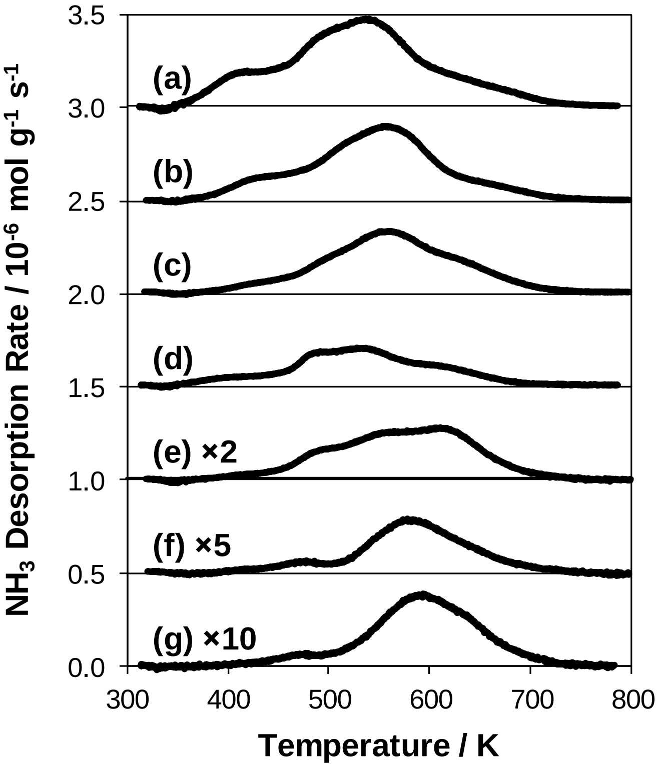

Figure S2. NH_3-TPD profiles for H-Al-Beta-F zeolites with Si/Al = (a) 23, (b) 34, (c) 45, (d) 65, (e) 93, (f) 220, (g) 500. Offset by 0.5 units for clarity.

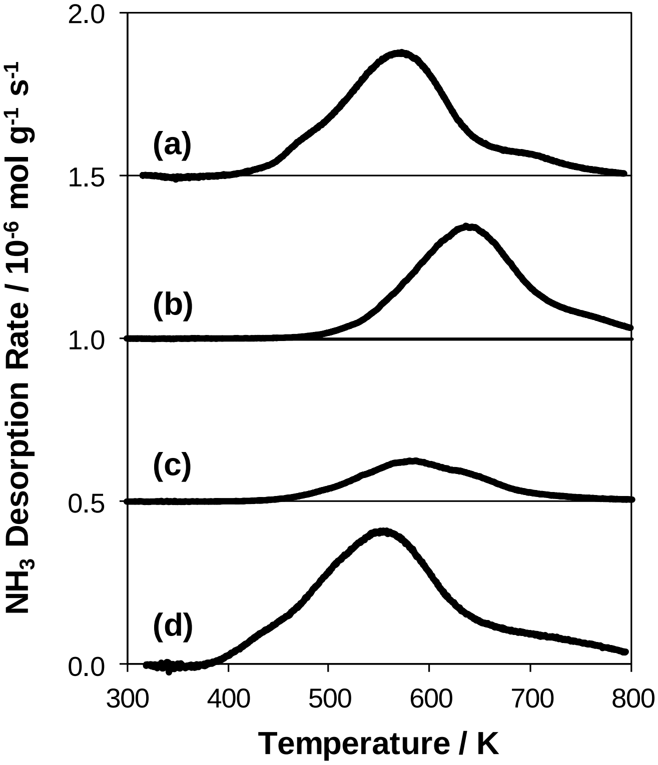

Figure S3. NH_3-TPD profiles for (a) H-Al-MFI, (b) H-Al-TON, (c) H-Al-FAU, (d) H-Al-Beta-OH(1.7). Offset by 0.5 units for clarity.

S.3.3. In situ 2,6-di-tert-butylpyridine titration data

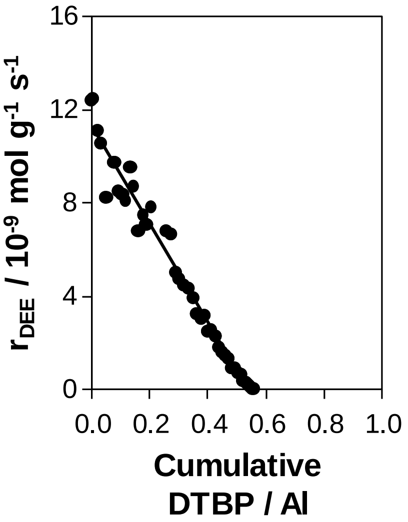

Figure S4. Diethyl ether formation rate (per g catalyst, 378 K, 5 kPa C_2H_5OH, 1 kPa H_2O) as a function of 2,6-di-*tert*-butylpyridine uptake (0.6 Pa DTBP) on H-Al-Beta-F(2.0) during catalysis. Solid line represents linear regression.

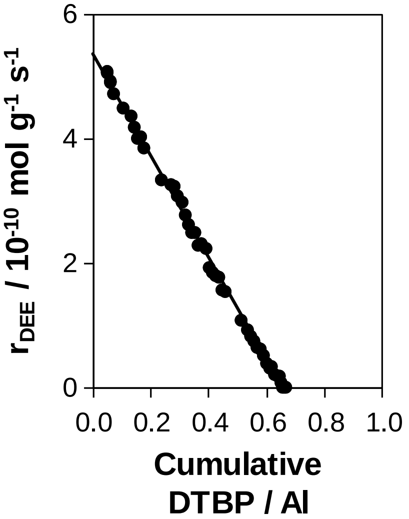

Figure S5. Diethyl ether formation rate (per g catalyst, 378 K, 0.7 kPa C_2H_5OH, 30 kPa H_2O) as a function of 2,6-di-*tert*-butylpyridine uptake (1.4 Pa DTBP) on H-Al-Beta-F(2.0) during catalysis. Solid line represents linear regression.

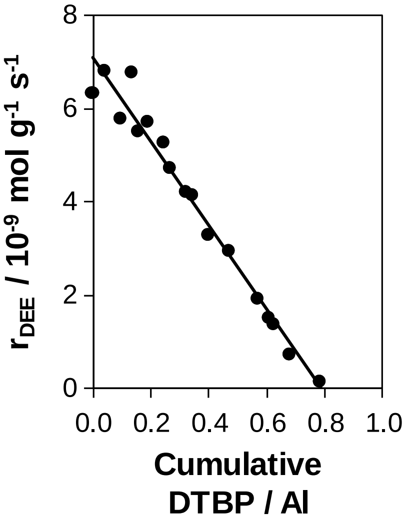

Figure S6. Diethyl ether formation rate (per g catalyst, 378 K, 4.5 kPa C_2H_5OH, 1 kPa H_2O) as a function of 2,6-di-*tert*-butylpyridine uptake (1.8 Pa DTBP) on H-Al-Beta-F(1.2) during catalysis. Solid line represents linear regression.

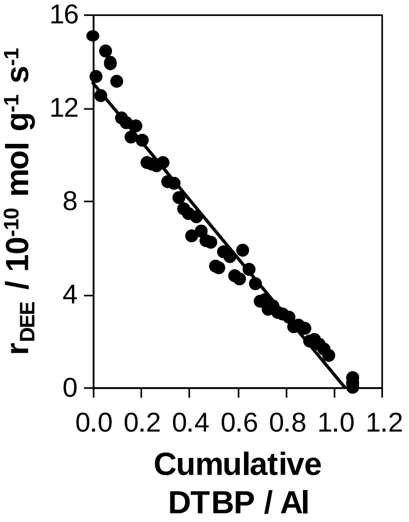

Figure S7. Diethyl ether formation rate (per g catalyst, 378 K, 4.5 kPa C_2H_5OH, 1 kPa H_2O) as a function of 2,6-di-*tert*-butylpyridine uptake (0.5 Pa DTBP) on H-Al-Beta-F(0.16) during catalysis. Solid line represents linear regression.

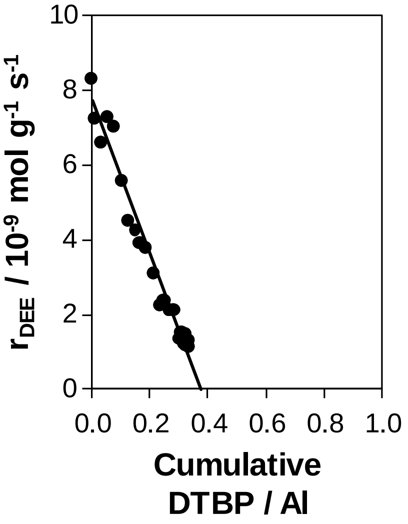

Figure S8. Diethyl ether formation rate (per g catalyst, 378 K, 4.4 kPa C_2H_5OH, 1 kPa H_2O) as a function of 2,6-di-*tert*-butylpyridine uptake (1.9 Pa DTBP) on H-Al-Beta-OH(1.7) during catalysis. Solid line represents linear regression.

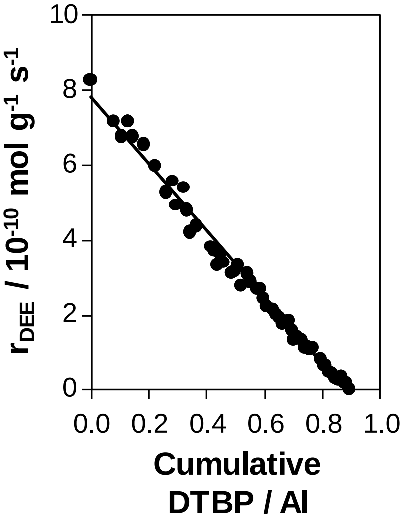

Figure S9. Diethyl ether formation rate (per g catalyst, 373 K, 4.7 kPa C_2H_5OH, 1 kPa H_2O) as a function of 2,6-di-*tert*-butylpyridine uptake (0.9 Pa DTBP) on H-Al-FAU during catalysis. Solid line represents linear regression.

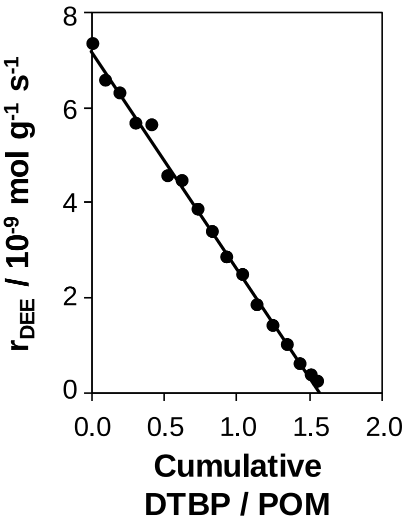

Figure S10. Diethyl ether formation rate (per g catalyst, 378 K, 4.5 kPa C_2H_5OH, 1 kPa H_2O) as a function of 2,6-di-*tert*-butylpyridine uptake (0.4 Pa DTBP) on HPW/Si-MCM-41 during catalysis. Solid line represents linear regression.

S.3.4. Ethanol dehydration kinetic data

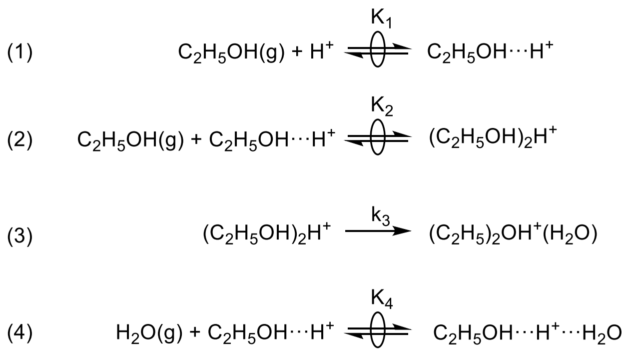

Figure S11. Series of elementary steps describing associative bimolecular ethanol dehydration at H^+ sites in zeolites (steps 1–3), and the adsorption of water to form inhibitory ethanol-water dimers (step 4). Kinetically irrelevant DEE and water desorption steps are omitted for brevity.

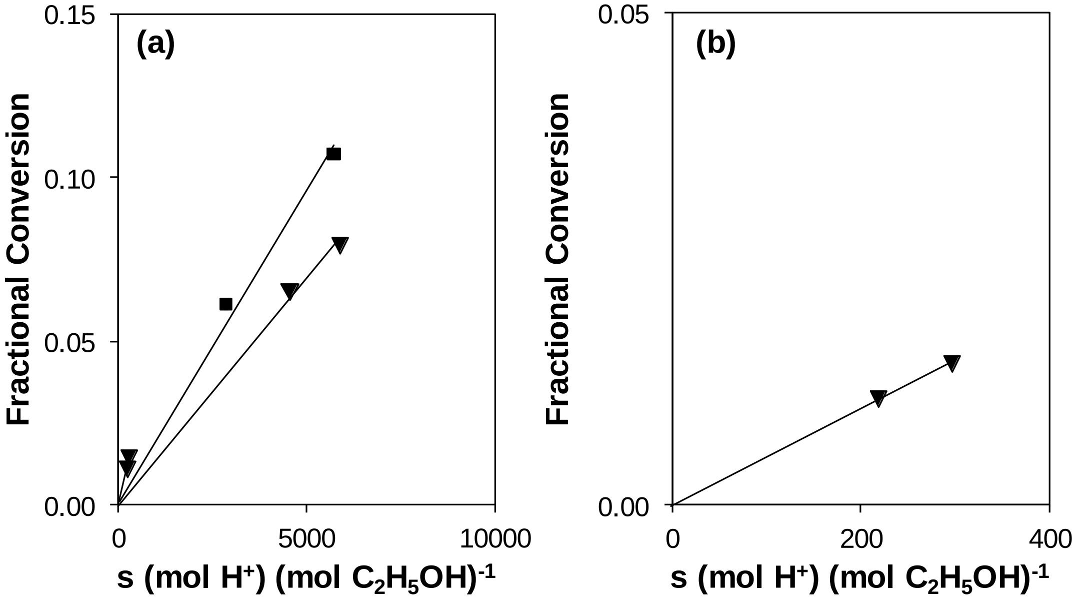

Figure S12. (a) Fractional conversion of C_2H_5OH as a function of site-contact time at 0.008 kPa C_2H_5OH on H-Al-Beta-F(2.0) (■), and at 0.04 kPa and 0.002 kPa C_2H_5OH on H-Al-Beta-OH(1.7) (▼), collected without co-fed H_2O at 373 K. (b) provides a better view of the data points near the origin in (a) at 0.04 kPa C_2H_5OH on H-Al-Beta-OH(1.7) (▼).

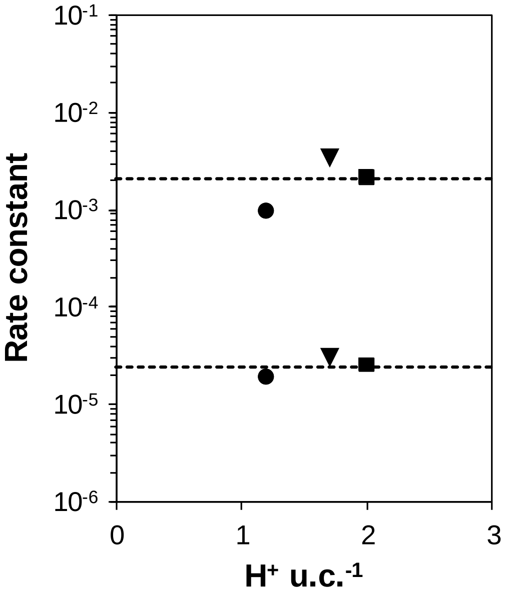

Figure S13. First-order (k_3K_2 / mol (mol H^+)$^{-1}$ kPa^{-1} s^{-1}) and zero-order (k_3 / mol (mol H^+)$^{-1}$ s^{-1}) dehydration rate constants (per H^+, 373 K) quantified on H-Al-Beta-F(1.2) (●), H-Al-Beta-F(2.0) (■), and H-Al-Beta-OH(1.7) (▼) as a function of H^+ density. Dashed line represents the average value. Because intracrystalline transport limitations would lead to lower k_3 values at higher H^+ densities, these data are consistent with kinetically limited rates as described by the Madon-Boudart criterion.[21]

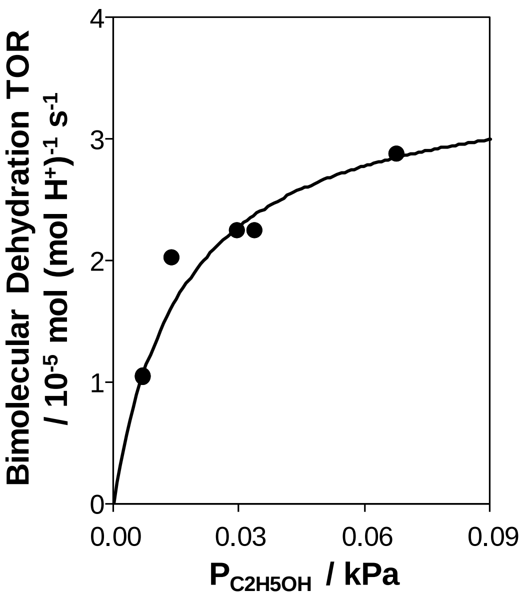

Figure S14. Bimolecular ethanol dehydration turnover rate (per H^+, 373 K) as a function of C_2H_5OH pressure, without co-fed H_2O, on H-Al-MFI. Solid line represents regression to Eq. (1) (Main Text).

These measurements (Figure S14) give values of $k_3 = 3.6\times10^{-5}$ mol (mol H^+)$^{-1}$ s^{-1} and $K_2 = 59$ kPa^{-1}. This value of k_3 agrees well with that measured by Chiang and Bhan[16] on the same Zeolyst H-Al-MFI sample (CBV8014). Chiang and Bhan report (in the zero-order regime, at 368 K) a value of $k = 1.7\times10^{5}$ mol (mol H^+)$^{-1}$ s^{-1}. Their reported k values as a function of temperature (368–409 K, $E_{app} = 103$ kJ mol^{-1}) can be used to interpolate this value at 373 K as $k = 2.7\times10^{-5}$ mol (mol H^+)$^{-1}$ s^{-1}. This value is 76% that quantified here (Figure S14), which is in reasonable agreement and thus provides a benchmark that validates the measurements reported using this reactor system.

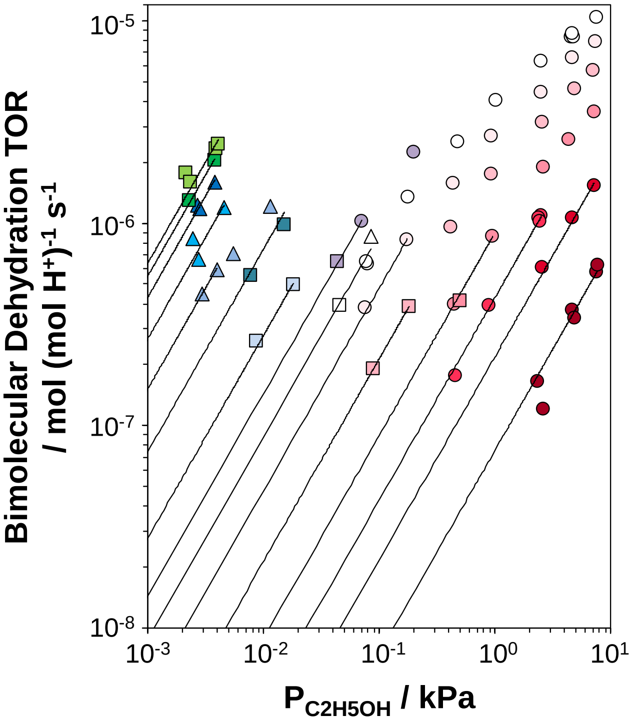

Figure S15. Bimolecular ethanol dehydration turnover rate (373 K, per H^+) on H-Al-Beta-F(2.0) as a function of ethanol pressure at water pressures of 0.02, 0.05, 0.2, 0.6, 2, 5, 7, 10, 14, 20, 30, 40, 50, 75 kPa. Squares, triangles, and circles were measured in separate experiments. Solid lines reflect linear regression to data points in first-order regimes.

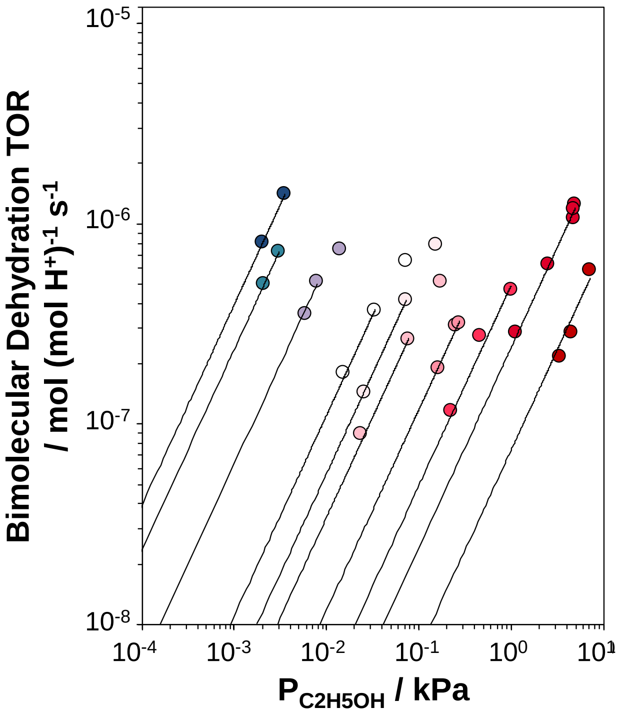

Figure S16. Bimolecular ethanol dehydration turnover rate (373 K, per H^+) on H-Al-Beta-F(1.2) as a function of ethanol pressure at water pressures of 0.02, 0.2, 2, 10, 14, 20, 30, 40, 50, 75 kPa. Solid lines reflect linear regression to data points in first-order regimes.

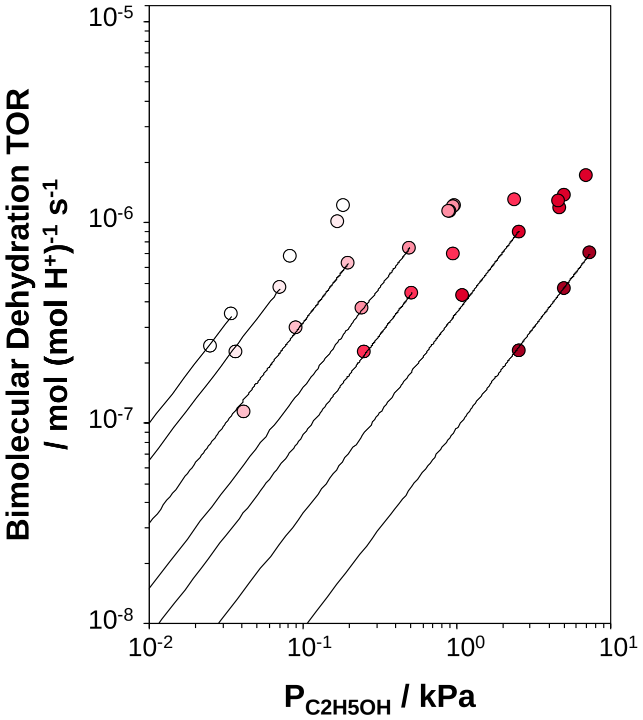

Figure S17. Bimolecular ethanol dehydration turnover rate (373 K, per H^+) on H-Al-Beta-F(0.16) as a function of ethanol pressure at water pressures of 10, 14, 20, 30, 40, 50, 75 kPa. Solid lines reflect linear regression to data points in first-order regimes.

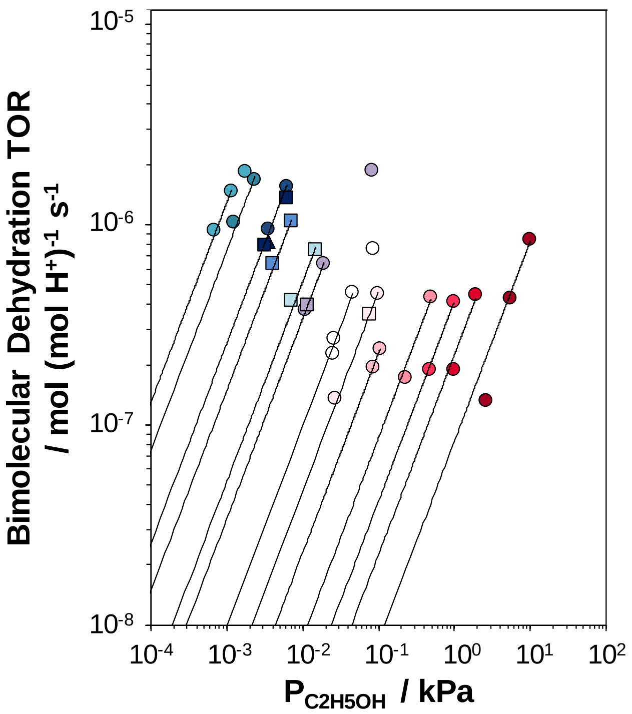

Figure S18. Bimolecular ethanol dehydration turnover rate (373 K, per H$^+$) on H-Al-Beta-OH(1.7) as a function of ethanol pressure at water pressures of 0.05, 0.2, 0.6, 1, 2, 5, 10, 14, 20, 30, 40, 50, 75 kPa. Squares and circles were measured in separate experiments. Solid lines reflect linear regression to data points in first-order regimes.

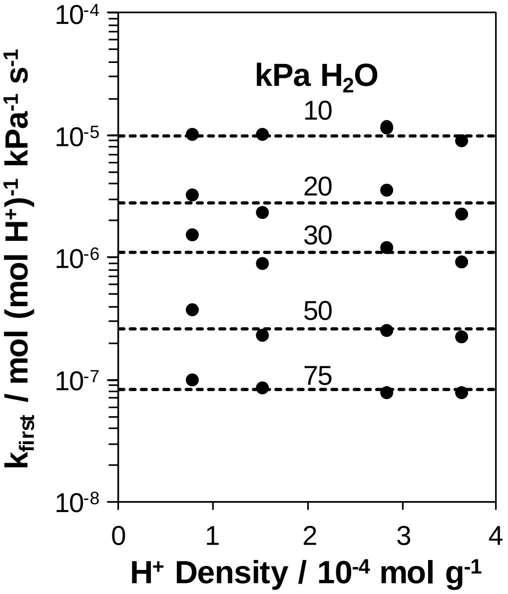

Figure S19. Apparent first-order rate constant for bimolecular ethanol dehydration (per H^+, 373 K) on H-Al-Beta samples as a function of H_2O pressure (10–75 kPa) and H^+ density (quantified by *in situ* 2,6-di-*tert*-butylpyridine titration). Dashed lines represent averages at each H_2O pressure.

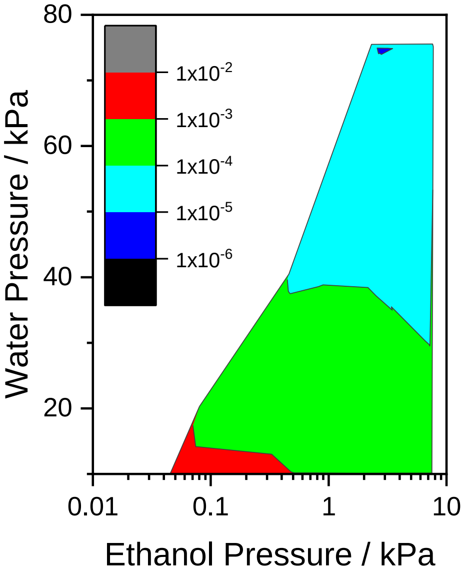

Figure S20. Mears criterion values calculated as a function of ethanol and water pressure on H-Al-Beta-F(2.0) at 373 K. Shaded regions correspond to Mears criterion values that fall in the range of values specified by the scale bar.

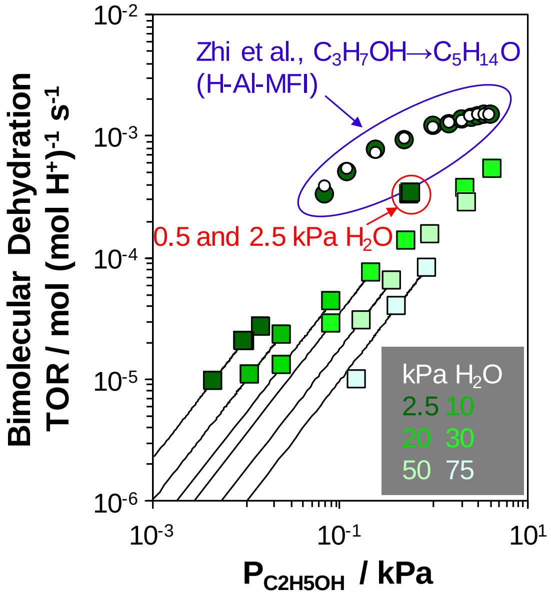

Figure S21. Bimolecular ethanol dehydration turnover rate (423 K, per H^+) on H-Al-Beta-F(1.2) (boxes) as a function of ethanol pressure at water pressures between 2.5–75 kPa (see color legend in bottom right). Bimolecular 1-propanol dehydration turnover rates (423, per H^+) on H-Al-MFI reported by Zhi et al.[20] are adapted from Figure 3S in their manuscript's Supporting Information, where the filled circles were collected at 2.5 kPa H_2O, and the open circles were collected at 0.53 kPa H_2O.

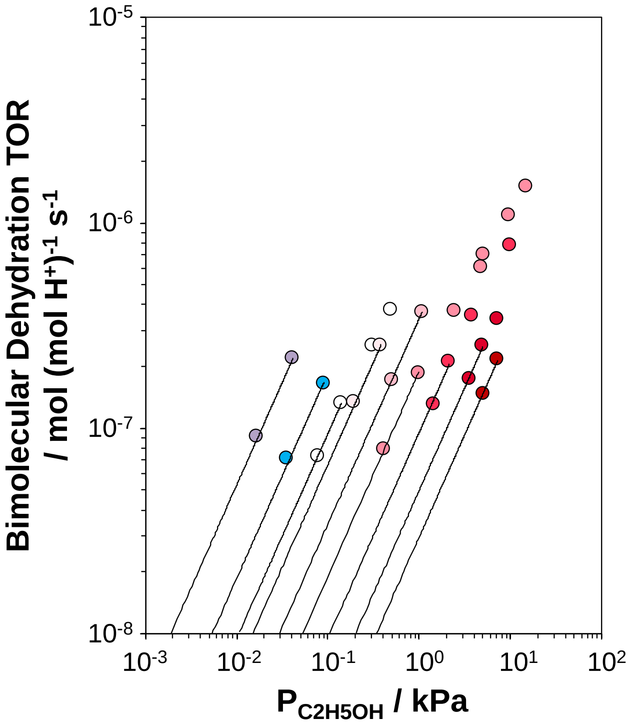

Figure S22. Bimolecular ethanol dehydration turnover rate (373 K, per H$^+$) on H-Al-FAU as a function of ethanol pressure at water pressures of 2, 5, 10, 14, 20, 30, 40, 60 kPa. Solid lines reflect linear regression to data points in first-order regimes.

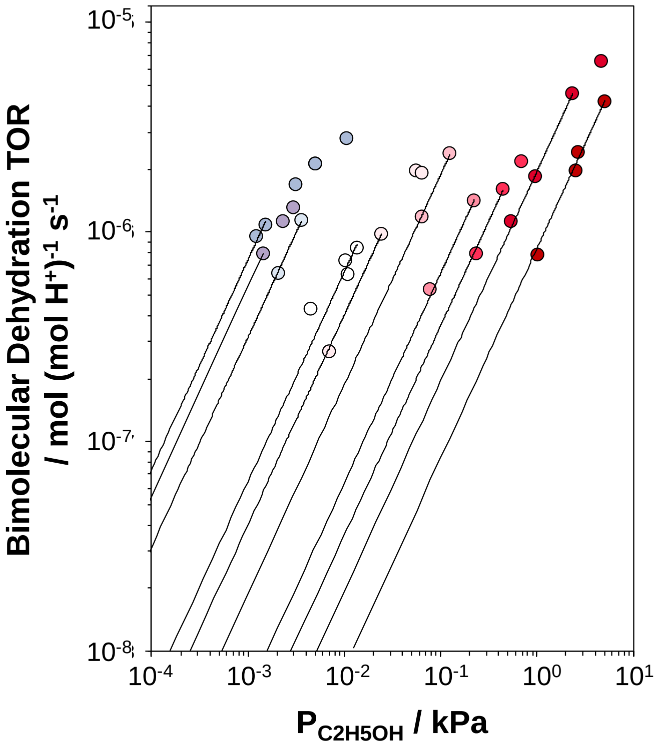

Figure S23. Bimolecular ethanol dehydration turnover rate (373 K, per H^+) on H-Al-TON as a function of ethanol pressure at water pressures of 1, 2, 5, 10, 14, 20, 30, 40, 50, 75 kPa. Solid lines reflect linear regression to data points in first-order regimes.

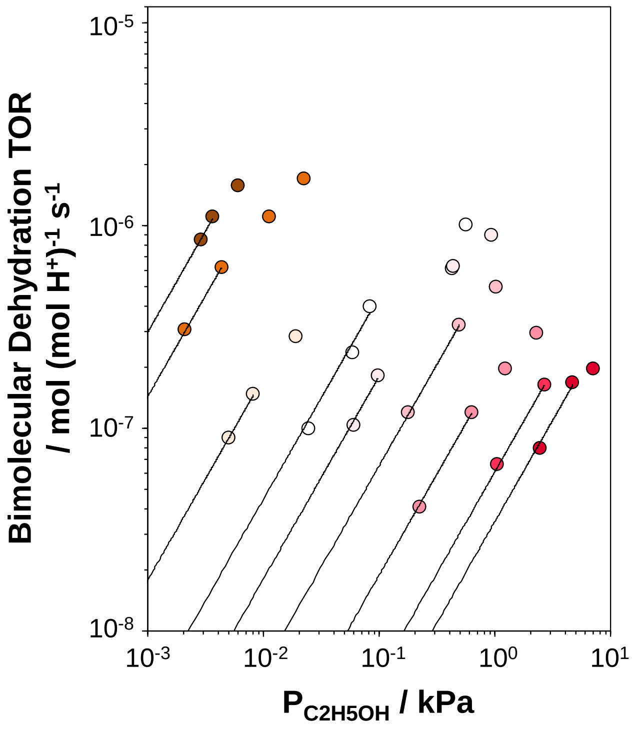

Figure S24. Bimolecular ethanol dehydration turnover rate (373 K, per H$^+$) on H-Al-CHA as a function of ethanol pressure at water pressures of 0.2, 0.6, 5, 10, 14, 20, 30, 40, 50 kPa. Solid lines reflect linear regression to data points in first-order regimes.

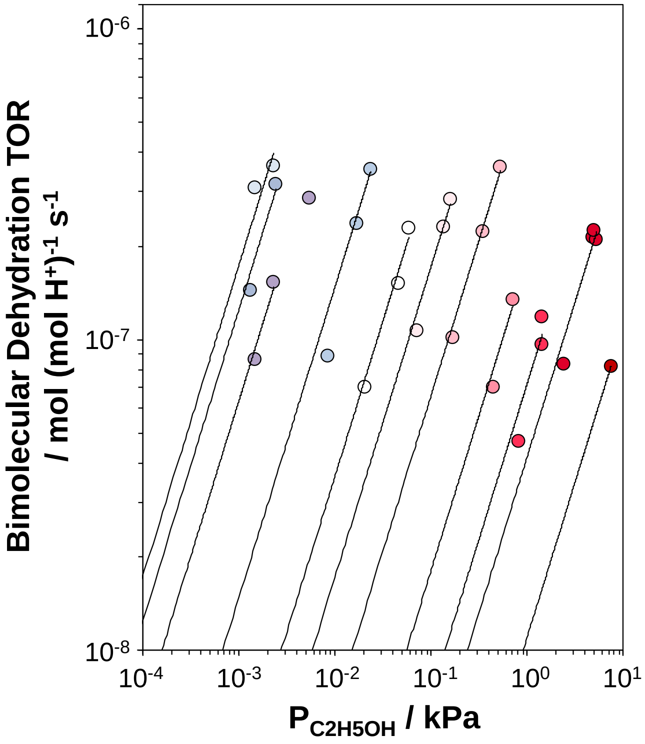

Figure S25. Bimolecular ethanol dehydration turnover rate (373 K, per H^+) on H-Al-AEI as a function of ethanol pressure at water pressures of 0.6, 1, 2, 5, 10, 14, 20, 30, 40, 50, 75 kPa. Solid lines reflect linear regression to data points in first-order regimes.

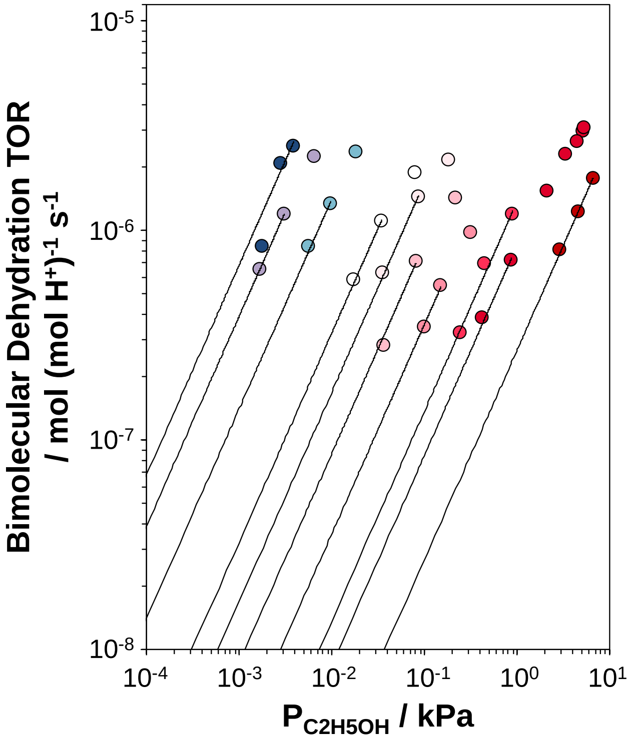

Figure S26. Bimolecular ethanol dehydration turnover rate (373 K, per H^+) on H-Al-MFI as a function of ethanol pressure at water pressures of 0.02, 0.2, 2, 10, 14, 20, 30, 40, 50, 75 kPa. Solid lines reflect linear regression to data points in first-order regimes.

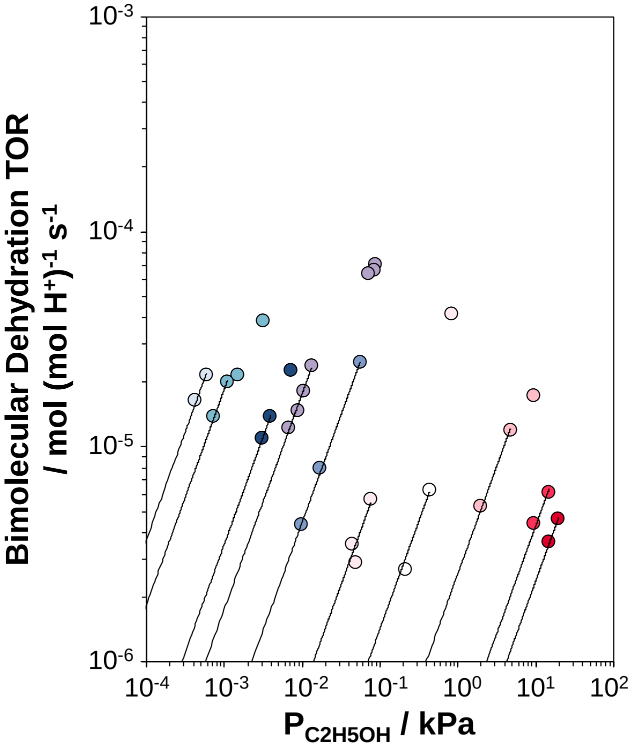

Figure S27. Bimolecular ethanol dehydration turnover rate (373 K, per H^+) on HPW/Si-MCM-41 as a function of ethanol pressure at water pressures of 0.1, 0.2, 0.6, 1, 2, 5, 10, 20, 40, 50 kPa. Solid lines reflect linear regression to data points in the first-order regime.

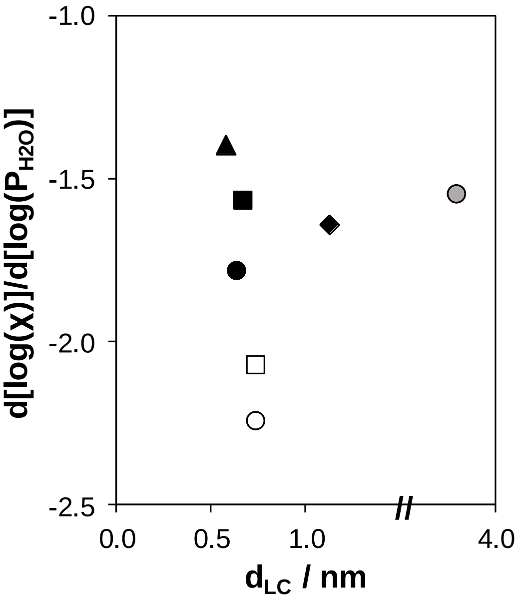

Figure S28. Dependence of activity coefficient ratios ($\chi = \gamma_{EWn}/\gamma_{\ddagger}$) on P_{H2O} in the high water pressure limit, on H-Al-Beta-F(2.0) (■), H-Al-TON (▲), H-Al-MFI (●), H-Al-FAU (◆), H-Al-AEI (□), H-Al-CHA (○), and HPW/Si-MCM-41 (●), as a function of the diameter of the largest included sphere within the pore topology (d_{LC}).

S.3.5. Volumetric adsorption isotherms

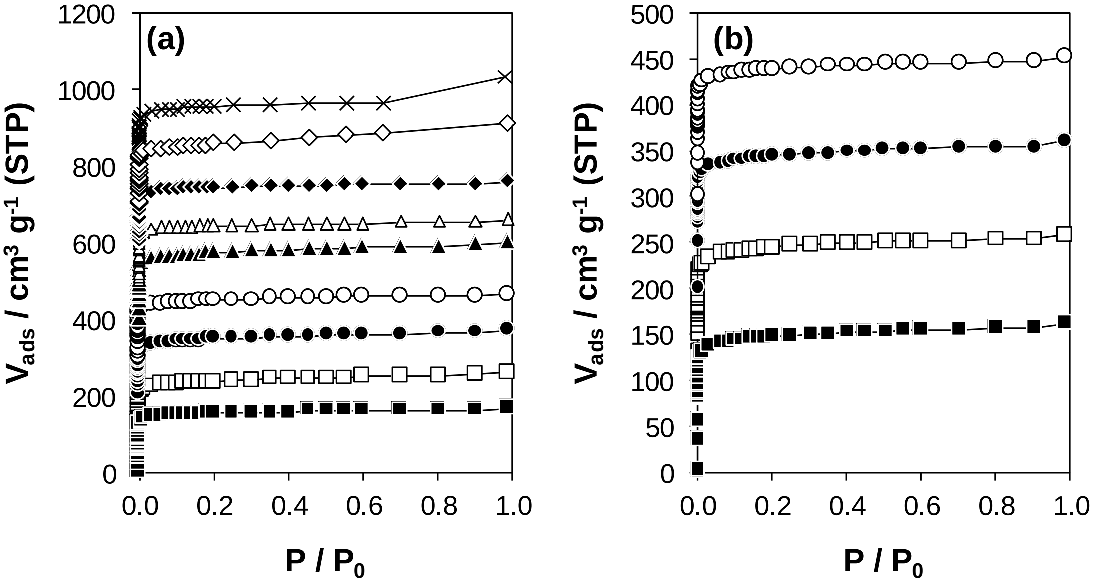

Figure S29. Volumetric N_2 adsorption isotherms (77 K) measured on H-Al-Beta-F samples (a) and their dealuminated analogs (b), with H^+ (or Si-OH nest) per unit cell = 0 (◇), 0.11 (◆), 0.16 (△), 0.57 (▲), 0.78 (○), 1.2 (●), 1.4 (□), and 2.0 (■), and on H-Al-Beta-OH(1.7) (×). Isotherms are offset by 100 units for clarity.

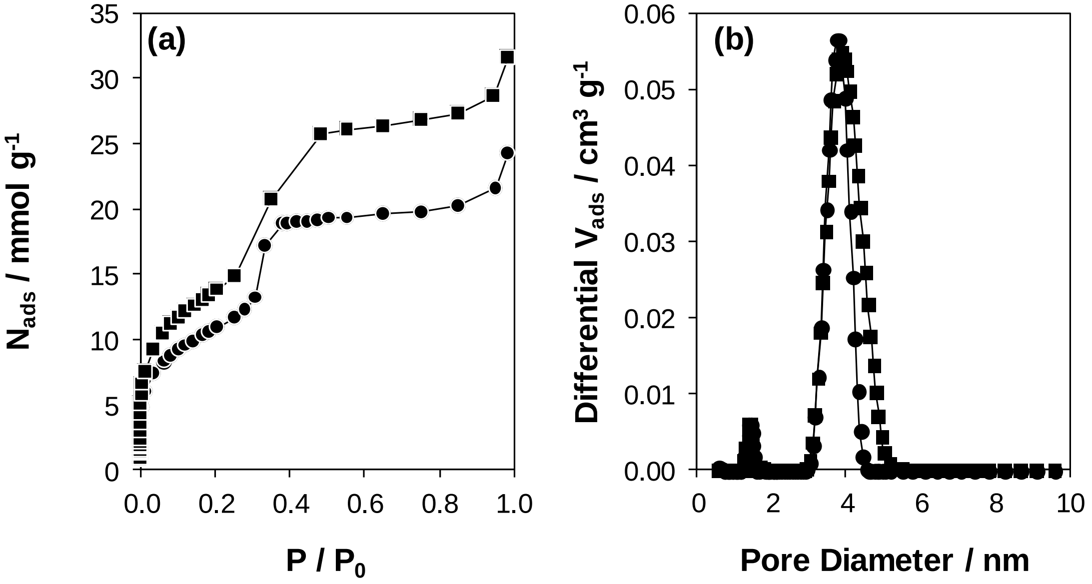

Figure S30. (a) Volumetric N_2 adsorption isotherms (77 K) measured on Si-MCM-41 (■) and HPW/Si-MCM-41 (●), and (b) NLDFT-based pore-size distributions derived from the data.

The mesopores of Si-MCM-41 are between 3.0–5.5 nm, with the maximum of the distribution at 3.9 nm. The mesopores of HPW/Si-MCM-41 are between 3.0–4.5 nm, with the maximum of the distribution at 3.8 nm. This indicates that the POM clusters are located within the mesopores and preferentially occupy the mesopores of larger diameter.

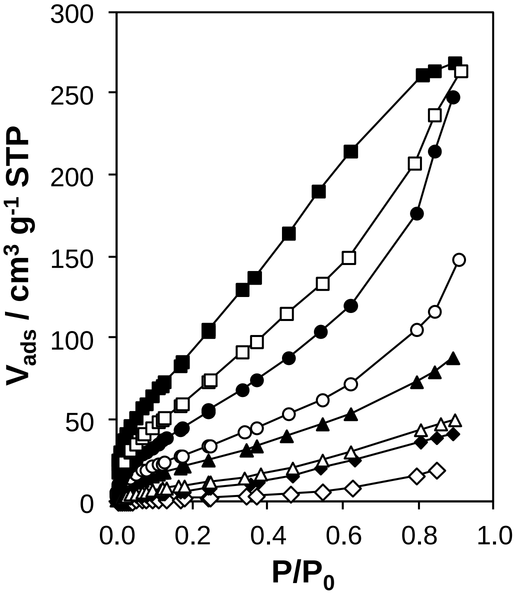

Figure S31. Volumetric H_2O adsorption isotherms (293 K) on H-Al-Beta-F samples, with H^+ u.c.$^{-1}$ = 0.11 (◆), 0.16 (△), 0.57 (▲), 0.78 (○), 1.2 (●), 1.4 (□), 2.0 (■), and Si-Beta-F (◇).

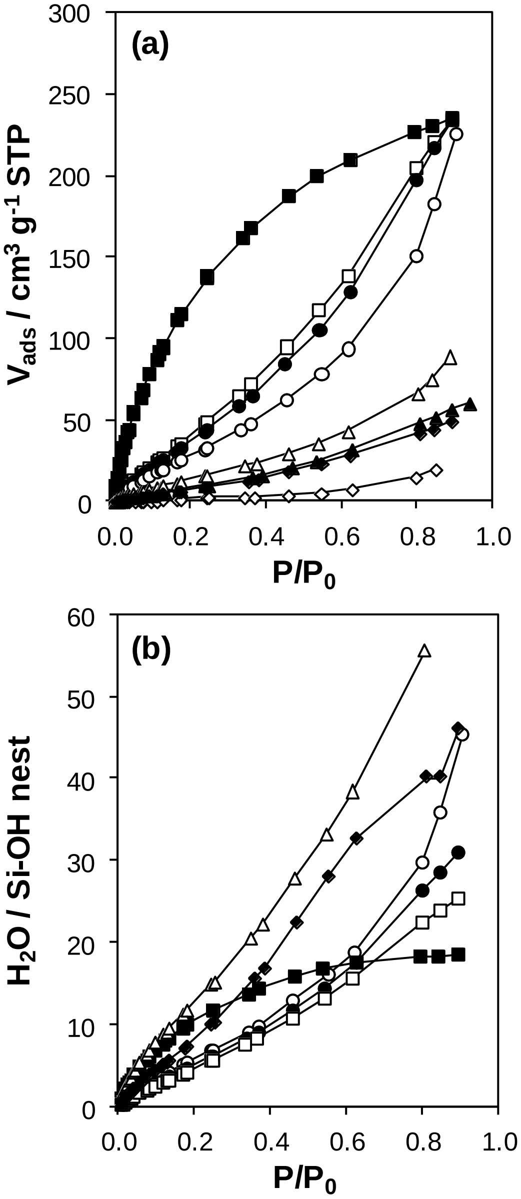

Figure S32. (a) Volumetric H_2O adsorption isotherms (293 K) on deAl-Beta-F samples, with Si-OH nest u.c.$^{-1}$ = 0.11 (◆), 0.16 (△), 0.57 (▲), 0.78 (○), 1.2 (●), 1.4 (□), 2.0 (■), and Si-Beta-F (◇); and (b) after subtraction of Si-Beta-F isotherm and normalizing by Si-OH nests.

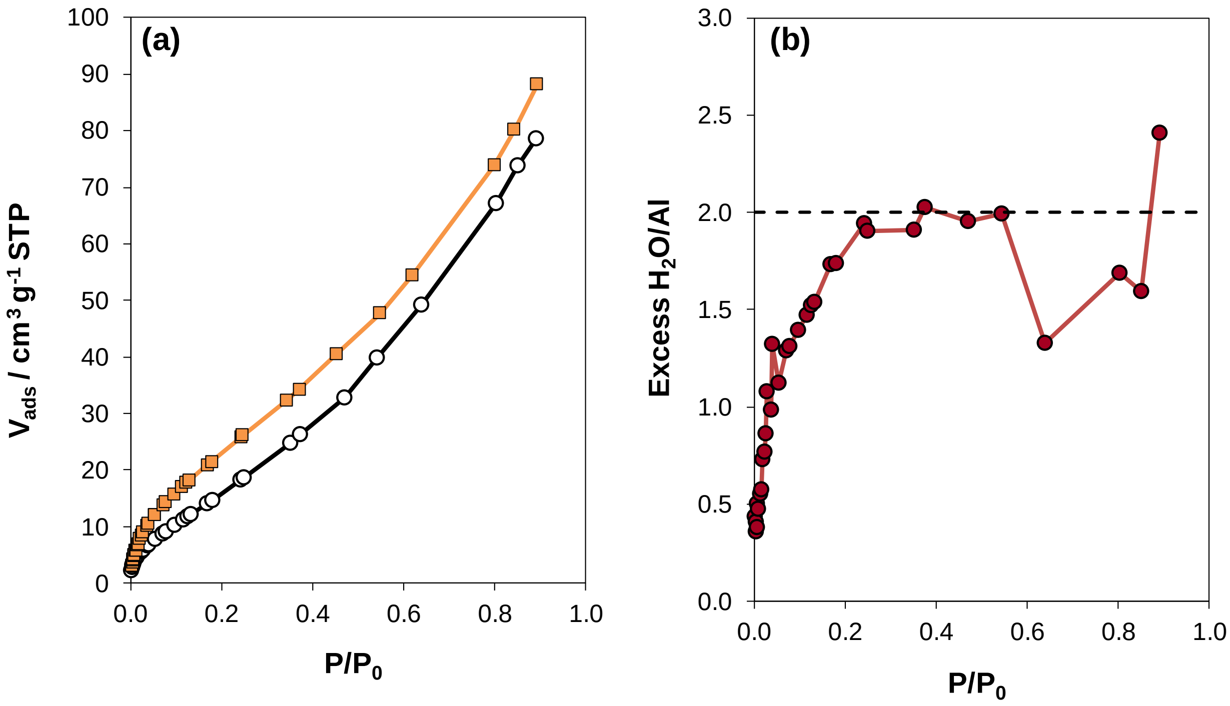

Figure S33. (a) Volumetric H_2O adsorption isotherms (293 K) on H-Al-Beta-F(0.57) (orange squares) and Na-Al-Beta-F(0.57) (black circles). (b) Difference between H-Al-Beta-F(0.57) and Na-Al-Beta-F(0.57) isotherms in (a), normalized by the Al density. Dashed line represents approximate plateau value between P/P_0 = 0.2–0.6, which implies that $(H^+)(H_2O)_n$ clusters are saturated at P/P_0 = 0.2, and that they contain 2 more H_2O molecules than $(Na^+)(H_2O)_n$ clusters.

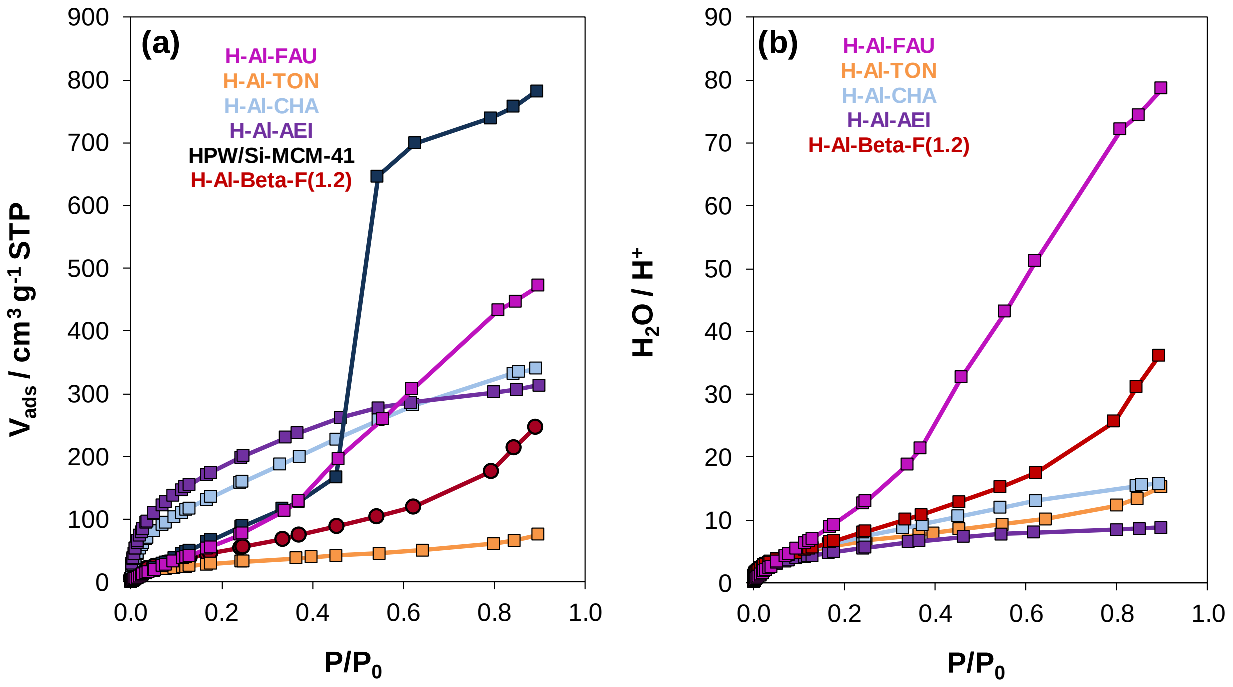

Figure S34. (a) H_2O adsorption isotherms (293 K) on H-Al-FAU (pink), H-Al-TON (orange), H-Al-CHA (light blue), H-Al-AEI (purple), HPW/Si-MCM-41 (dark blue), and H-Al-Beta-F(1.2) (red), for comparison. (b) Calculated H_2O adsorbed per H^+ on H-zeolite samples. H_2O adsorbed within Si-Beta-F or any other siliceous analogs is not subtracted in this case, as it is in the main text on H-Al-Beta-F samples.

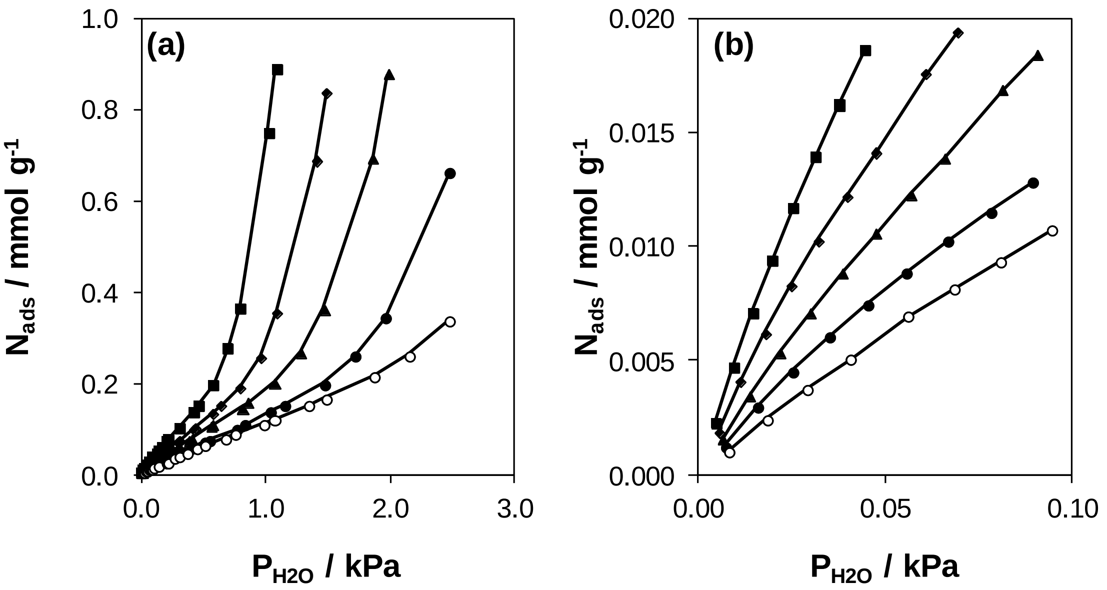

Figure S35. (a) Volumetric adsorption isotherms of H_2O on Si-Beta-F at 283 K (■), 288 K (◆), 293 K (▲), 298 K (●), and 302 K (○), with low-coverage data shown in (b) for clarity.

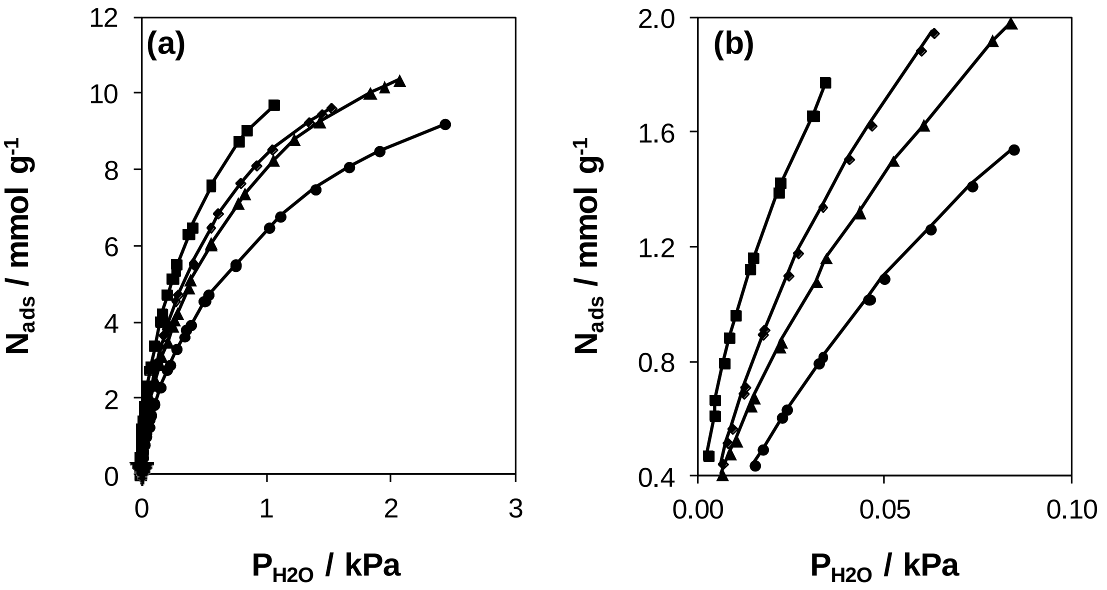

Figure S36. (a) Volumetric adsorption isotherms of H_2O on deAl-Beta-F(2.0) at 283 K (■), 288 K (◆), 293 K (▲), and 298 K (●), with low-coverage data shown in (b) for clarity.

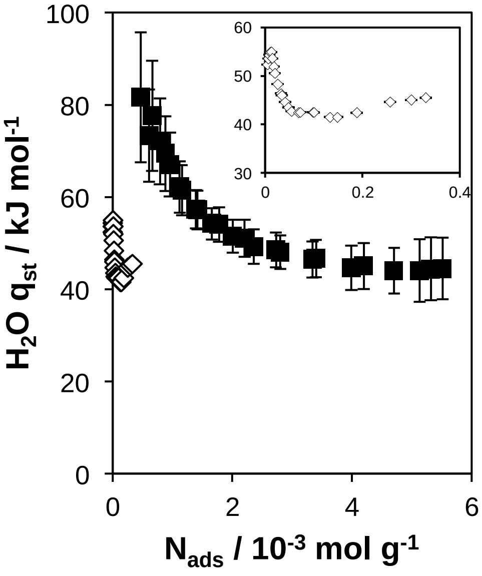

Figure S37. Isosteric heat of adsorption of H_2O as a function of coverage on Si-Beta-F (◇) and deAl-Beta-F(2.0) (■) determined in the range 283–302 K. Inset: detailed view of data on Si-Beta-F.

S.3.6. Infrared spectra collected at 293 K

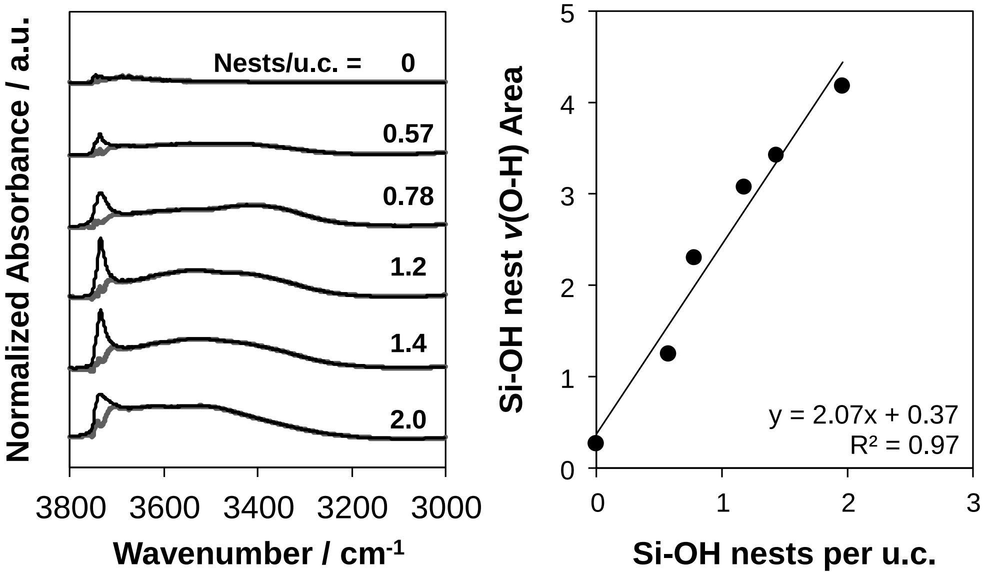

Figure S38. (a) Normalized (to T–O–T overtone peak area (1750–2100 cm^{-1})) IR spectra of Si-Beta-F and deAl-Beta-F zeolites at 293 K after treatment in flowing He to 823 K for 1 h. Grey traces represent deconvoluted signal for Si-OH nest peak areas. (b) Correlation of Si-OH nest ν(O-H) peak area with the number of Si-OH nests u.c.$^{-1}$ generated by removal of framework Al.

The integrated area for ν(OH) peaks of Si-OH nests has been also correlated with the number of Q^3 sites in ^{29}Si NMR by Flaherty and coworkers.[46]

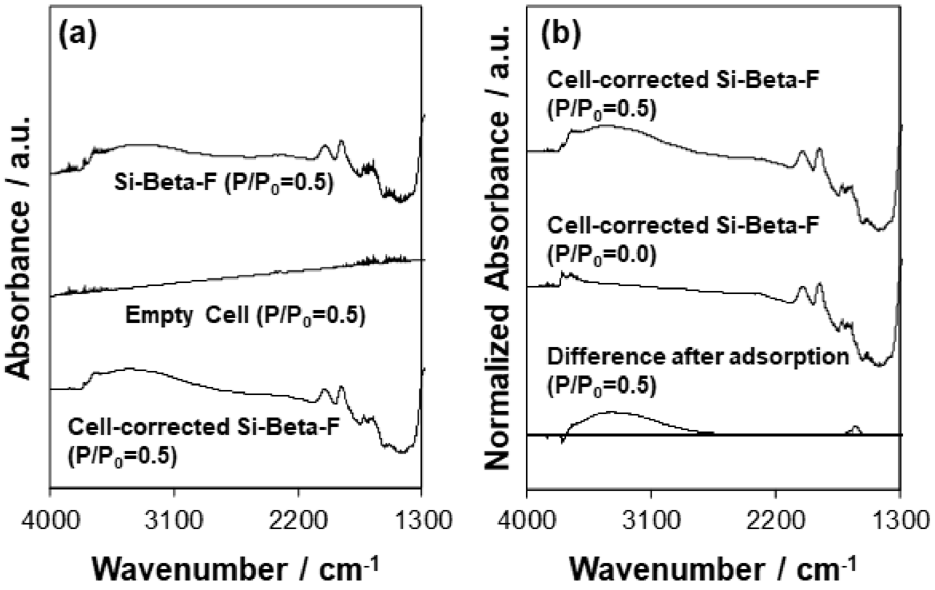

Figure S39. Illustration of processing of spectra under flowing H_2O, using Si-Beta-F at $P/P_0 = 0.5$ (293 K) as an example. (a) The signal from vapor-phase H_2O in the empty cell is subtracted from the signal for Si-Beta-F under flowing vapor-phase H_2O to yield a cell-corrected spectrum, then (b) the spectrum of the zeolite in flowing He before H_2O adsorption is subtracted from this to give the difference after adsorption.

The spectra for the empty cell at the corresponding H_2O P/P_0 values were subtracted from the wafer spectra to yield cell-corrected spectra (Figure S39a). Then, the cell-corrected spectra were normalized by the Si-O-Si overtone vibration (1750–2100 cm^{-1}) peak area of the wafer before H_2O adsorption. The normalized, cell-corrected spectrum of the wafer before H_2O adsorption was subtracted from those measured at each H_2O P/P_0 value to give subtracted spectra (Figure S39b) that represent the signal for adsorbed H_2O, and any changes to the vibrations associated with the zeolite, e.g., perturbation of Si-OH groups. Spectra were also subtracted between incremental increases in H_2O pressure, denoted “differential subtracted,” in order to visualize the change in signal associated with the adsorption of additional H_2O molecules. Subtracted and differential subtracted spectra were further baseline-corrected with pivot points at 4000, 2400, and 1350 cm^{-1}, where no absorbance was detected.

Isolated Si-OH groups (3735 cm^{-1}, 3745 cm^{-1}) are perturbed by H_2O adsorbing throughout the entire P/P_0 range on samples with H^+/Si-OH nest densities between 0–1.4, as indicated by negative peaks in differential subtracted spectra (insets of Figures S40b–S54b), whereas these groups are fully perturbed above P/P_0 values of 0.5 in H-Al-Beta-F(2.0) and deAl-Beta-F(2.0). The perturbation of isolated Si-OH groups throughout the P/P_0 range is consistent with weaker adsorption at these groups concurrent with stronger adsorption at H^+ or Si-OH nests, as inferred from volumetric adsorption isotherms and isosteric heats of adsorption (Figure 3, Main Text and Section S.2.7, SI). Full perturbation of Si-OH groups at lower relative pressures than expected for strictly isolated Si-OH groups may result from their closer proximity, on average, to Si-OH nests or H^+ when such hydrophilic binding sites are present in higher density.

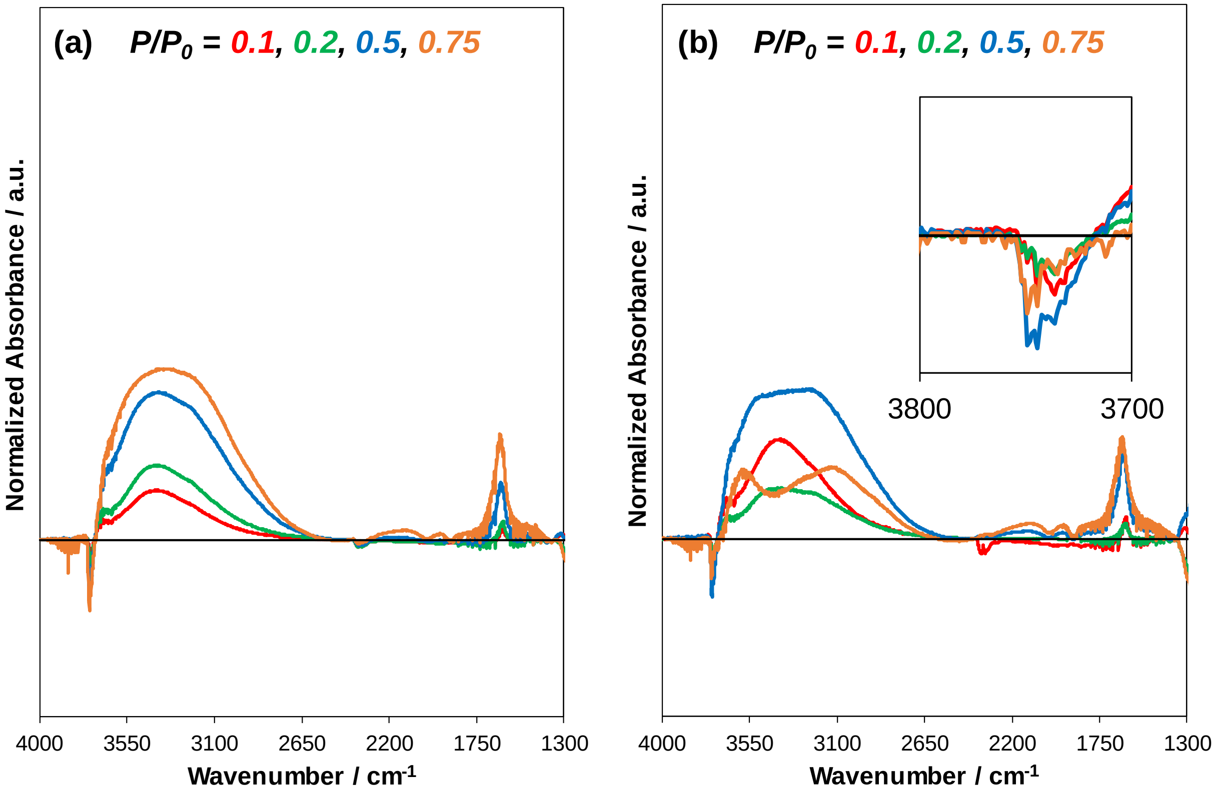

Figure S40. (a) Baseline-corrected difference IR spectra of H_2O adsorbed at 293 K on Si-Beta-F at P/P_0 values of 0.1 (red), 0.2 (green), 0.5 (blue), and 0.75 (orange). Difference spectra reflect the subtraction of the spectrum of the dehydrated sample under flowing He prior to H_2O adsorption, and the spectrum of H_2O adsorbed within an empty IR cell. (b) Differential-subtracted spectra reflect the difference between the spectrum at the given P/P_0 value and the next-lowest P/P_0 value. All spectra are normalized to the T–O–T overtone peak area (1750–2100 cm^{-1}) prior to adsorption. The spectra on Si-Beta-F were originally reported in Ref. [8].

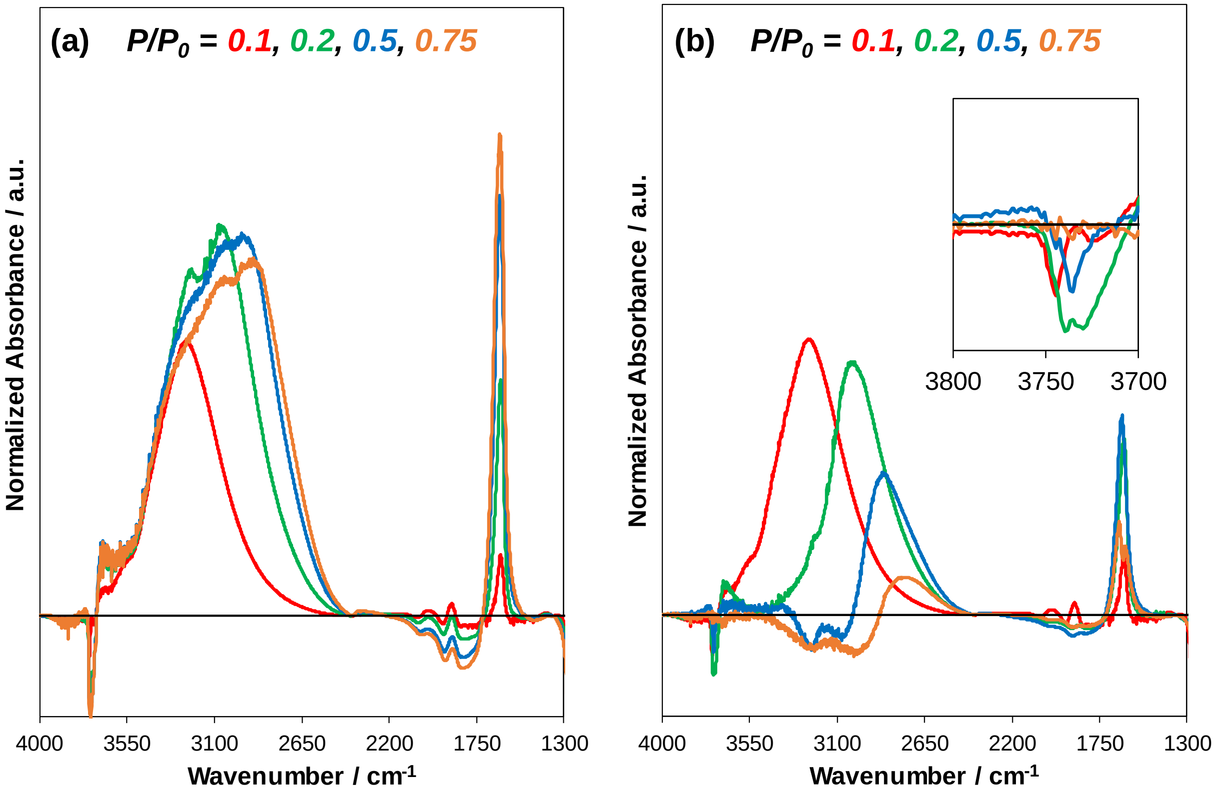

Figure S41. (a) Baseline-corrected difference IR spectra of H_2O adsorbed at 293 K on deAl-Beta-F(2.0) at P/P_0 values of 0.1 (red), 0.2 (green), 0.5 (blue), and 0.75 (orange). Difference spectra reflect the subtraction of the spectrum of the dehydrated sample under flowing He prior to H_2O adsorption, and the spectrum of H_2O adsorbed within an empty IR cell. (b) Differential-subtracted spectra reflect the difference between the spectrum at the given P/P_0 value and the next-lowest P/P_0 value. All spectra are normalized to the T–O–T overtone peak area (1750–2100 cm^{-1}) prior to adsorption.

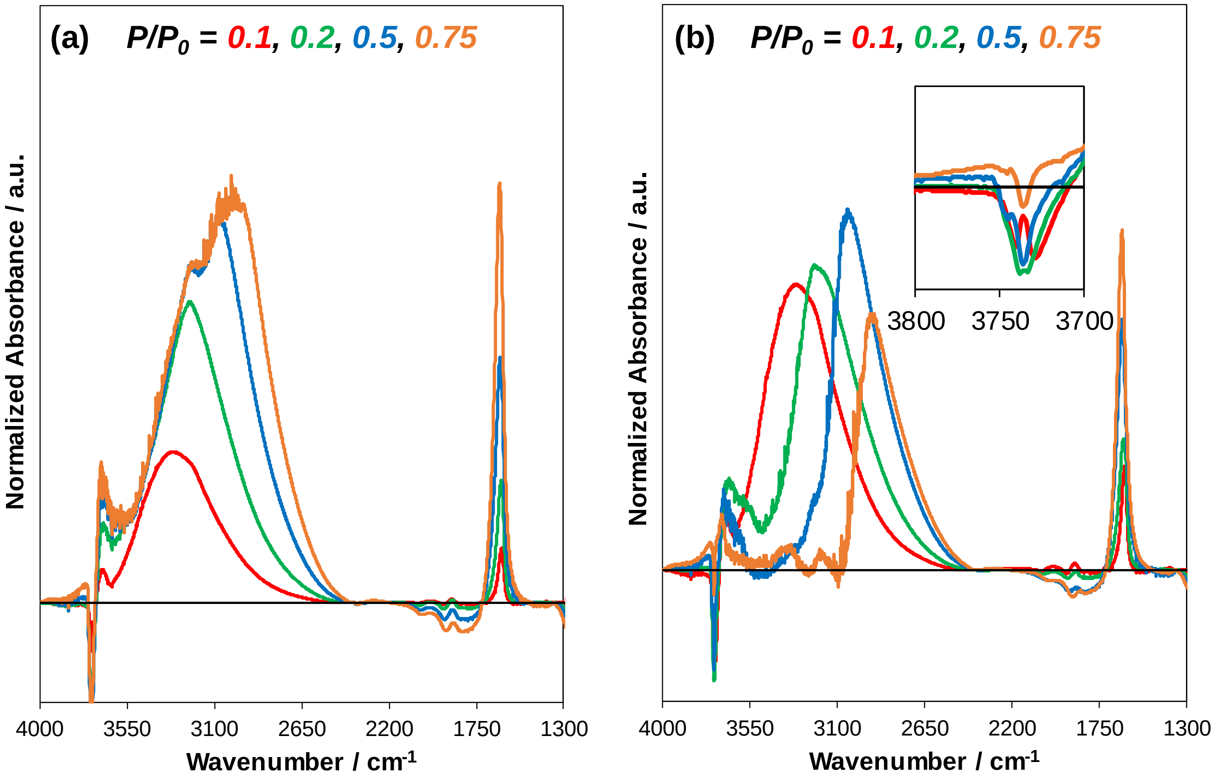

Figure S42. (a) Baseline-corrected difference IR spectra of H_2O adsorbed at 293 K on deAl-Beta-F(1.4) at P/P_0 values of 0.1 (red), 0.2 (green), 0.5 (blue), and 0.75 (orange). Difference spectra reflect the subtraction of the spectrum of the dehydrated sample under flowing He prior to H_2O adsorption, and the spectrum of H_2O adsorbed within an empty IR cell. (b) Differential-subtracted spectra reflect the difference between the spectrum at the given P/P_0 value and the next-lowest P/P_0 value. All spectra are normalized to the T–O–T overtone peak area (1750–2100 cm^{-1}) prior to adsorption.

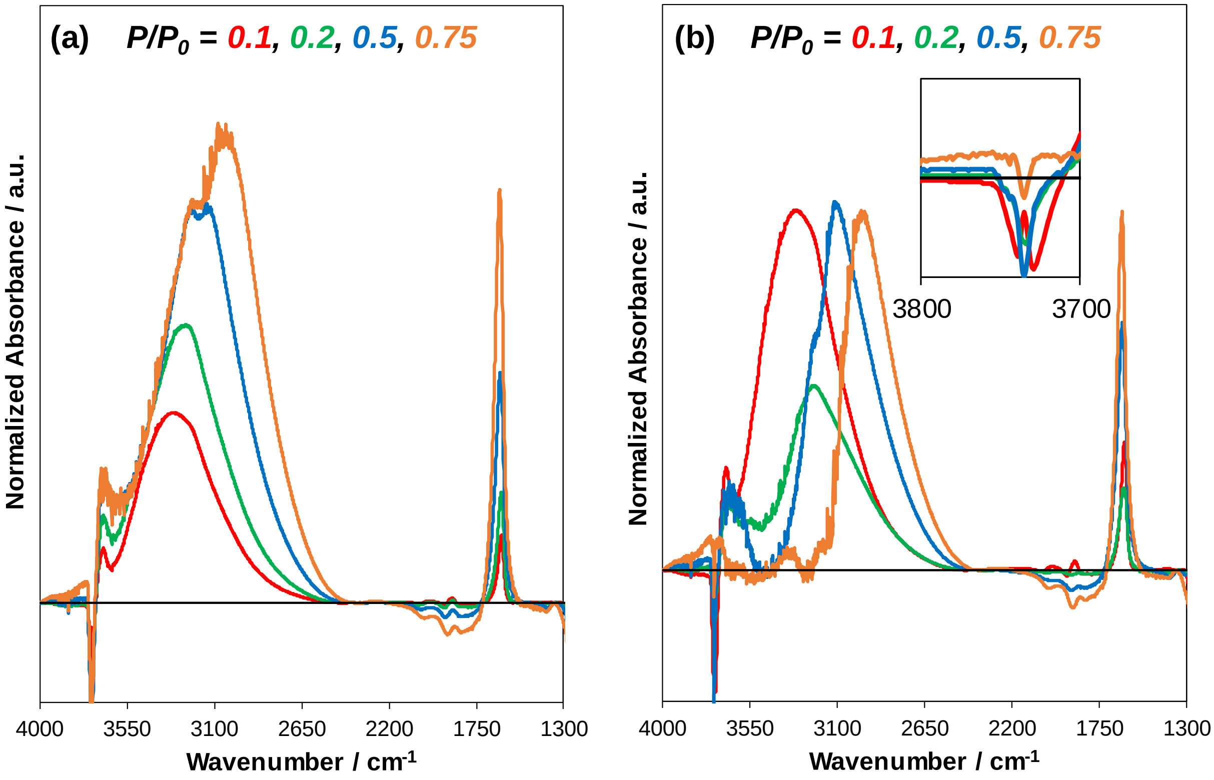

Figure S43. (a) Baseline-corrected difference IR spectra of H_2O adsorbed at 293 K on deAl-Beta-F(1.2) at P/P_0 values of 0.1 (red), 0.2 (green), 0.5 (blue), and 0.75 (orange). Difference spectra reflect the subtraction of the spectrum of the dehydrated sample under flowing He prior to H_2O adsorption, and the spectrum of H_2O adsorbed within an empty IR cell. (b) Differential-subtracted spectra reflect the difference between the spectrum at the given P/P_0 value and the next-lowest P/P_0 value. All spectra are normalized to the T–O–T overtone peak area (1750–2100 cm^{-1}) prior to adsorption.

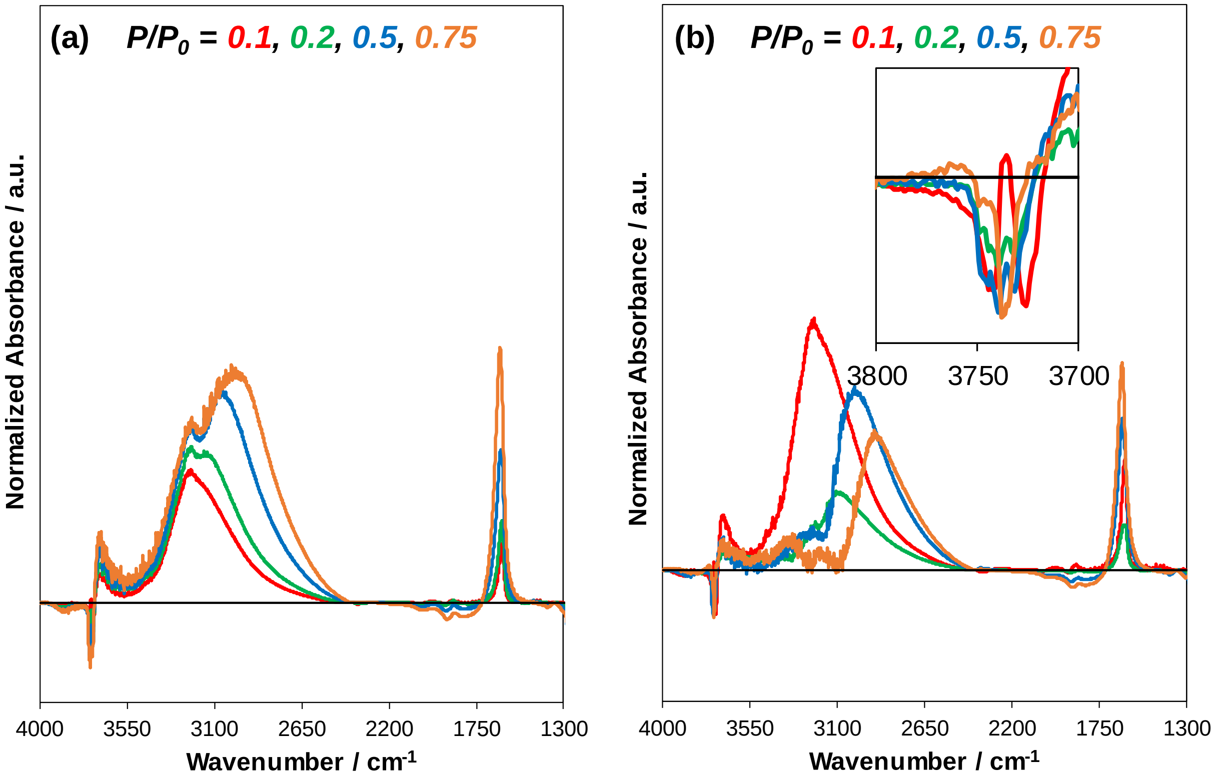

Figure S44. (a) Baseline-corrected difference IR spectra of H_2O adsorbed at 293 K on deAl-Beta-F(0.78) at P/P_0 values of 0.1 (red), 0.2 (green), 0.5 (blue), and 0.75 (orange). Difference spectra reflect the subtraction of the spectrum of the dehydrated sample under flowing He prior to H_2O adsorption, and the spectrum of H_2O adsorbed within an empty IR cell. (b) Differential-subtracted spectra reflect the difference between the spectrum at the given P/P_0 value and the next-lowest P/P_0 value. All spectra are normalized to the T–O–T overtone peak area (1750–2100 cm^{-1}) prior to adsorption. The spectra on deAl-Beta-F(0.78) were originally reported in Ref. [8].

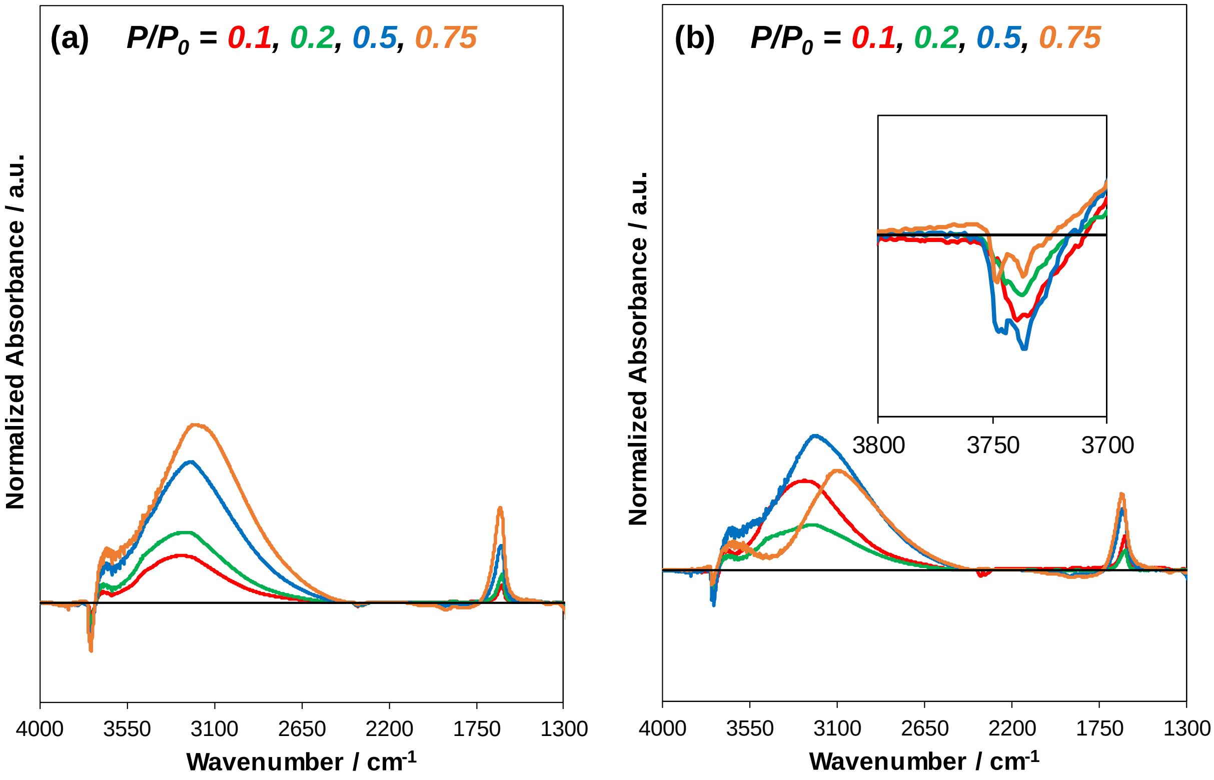

Figure S45. (a) Baseline-corrected difference IR spectra of H_2O adsorbed at 293 K on deAl-Beta-F(0.57) at P/P_0 values of 0.1 (red), 0.2 (green), 0.5 (blue), and 0.75 (orange). Difference spectra reflect the subtraction of the spectrum of the dehydrated sample under flowing He prior to H_2O adsorption, and the spectrum of H_2O adsorbed within an empty IR cell. (b) Differential-subtracted spectra reflect the difference between the spectrum at the given P/P_0 value and the next-lowest P/P_0 value. All spectra are normalized to the T–O–T overtone peak area (1750–2100 cm^{-1}) prior to adsorption.

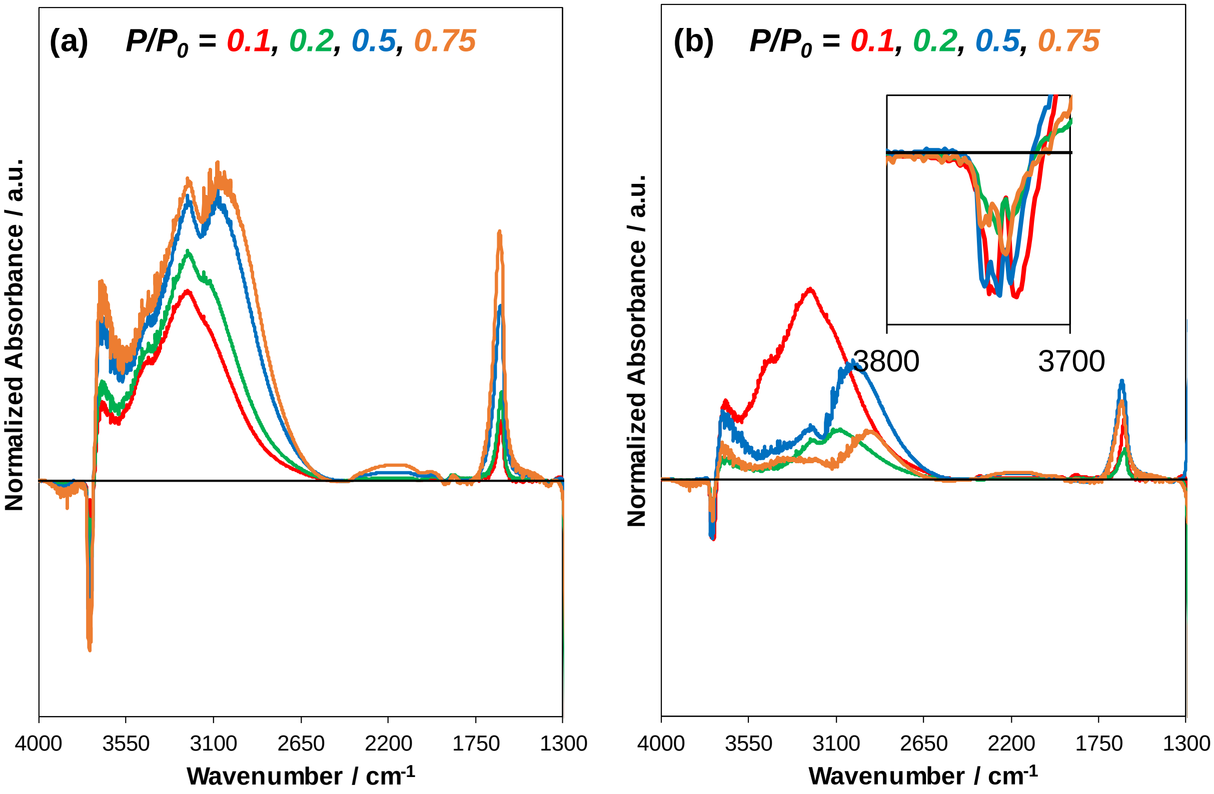

Figure S46. (a) Baseline-corrected difference IR spectra of H_2O adsorbed at 293 K on deAl-Beta-F(0.16) at P/P_0 values of 0.1 (red), 0.2 (green), 0.5 (blue), and 0.75 (orange). Difference spectra reflect the subtraction of the spectrum of the dehydrated sample under flowing He prior to H_2O adsorption, and the spectrum of H_2O adsorbed within an empty IR cell. (b) Differential-subtracted spectra reflect the difference between the spectrum at the given P/P_0 value and the next-lowest P/P_0 value. All spectra are normalized to the T–O–T overtone peak area (1750–2100 cm^{-1}) prior to adsorption.

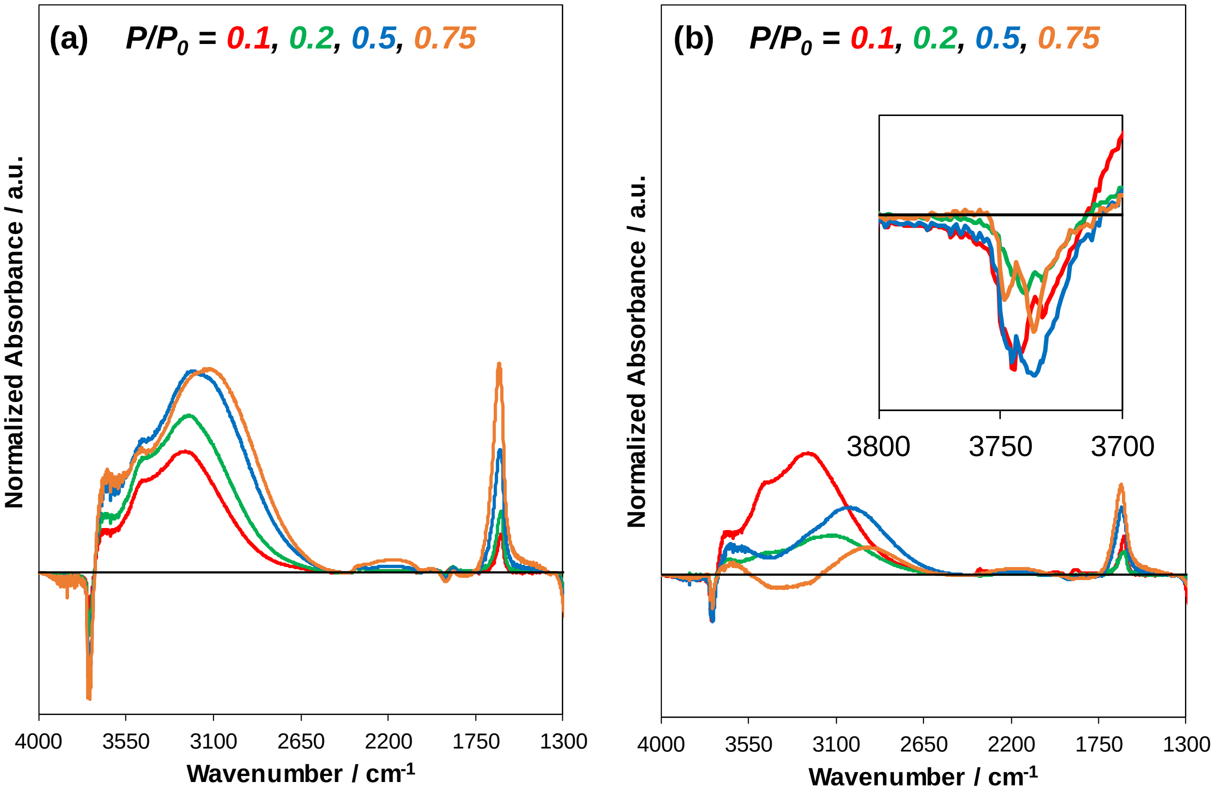

Figure S47. (a) Baseline-corrected difference IR spectra of H_2O adsorbed at 293 K on deAl-Beta-F(0.11) at P/P_0 values of 0.1 (red), 0.2 (green), 0.5 (blue), and 0.75 (orange). Difference spectra reflect the subtraction of the spectrum of the dehydrated sample under flowing He prior to H_2O adsorption, and the spectrum of H_2O adsorbed within an empty IR cell. (b) Differential-subtracted spectra reflect the difference between the spectrum at the given P/P_0 value and the next-lowest P/P_0 value. All spectra are normalized to the T–O–T overtone peak area (1750–2100 cm^{-1}) prior to adsorption.

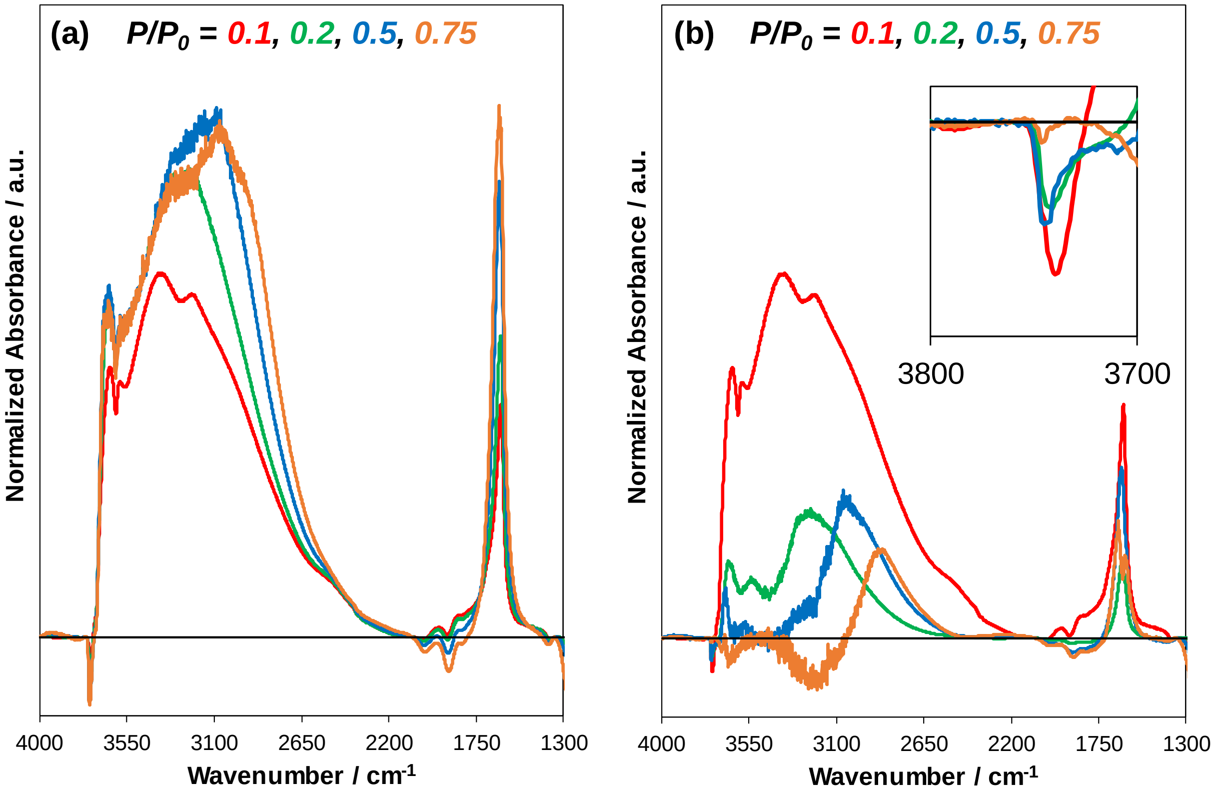

Figure S48. (a) Baseline-corrected difference IR spectra of H_2O adsorbed at 293 K on H-Al-Beta-F(2.0) at P/P_0 values of 0.1 (red), 0.2 (green), 0.5 (blue), and 0.75 (orange). Difference spectra reflect the subtraction of the spectrum of the dehydrated sample under flowing He prior to H_2O adsorption, and the spectrum of H_2O adsorbed within an empty IR cell. (b) Differential-subtracted spectra reflect the difference between the spectrum at the given P/P_0 value and the next-lowest P/P_0 value. All spectra are normalized to the T–O–T overtone peak area (1750–2100 cm^{-1}) prior to adsorption.

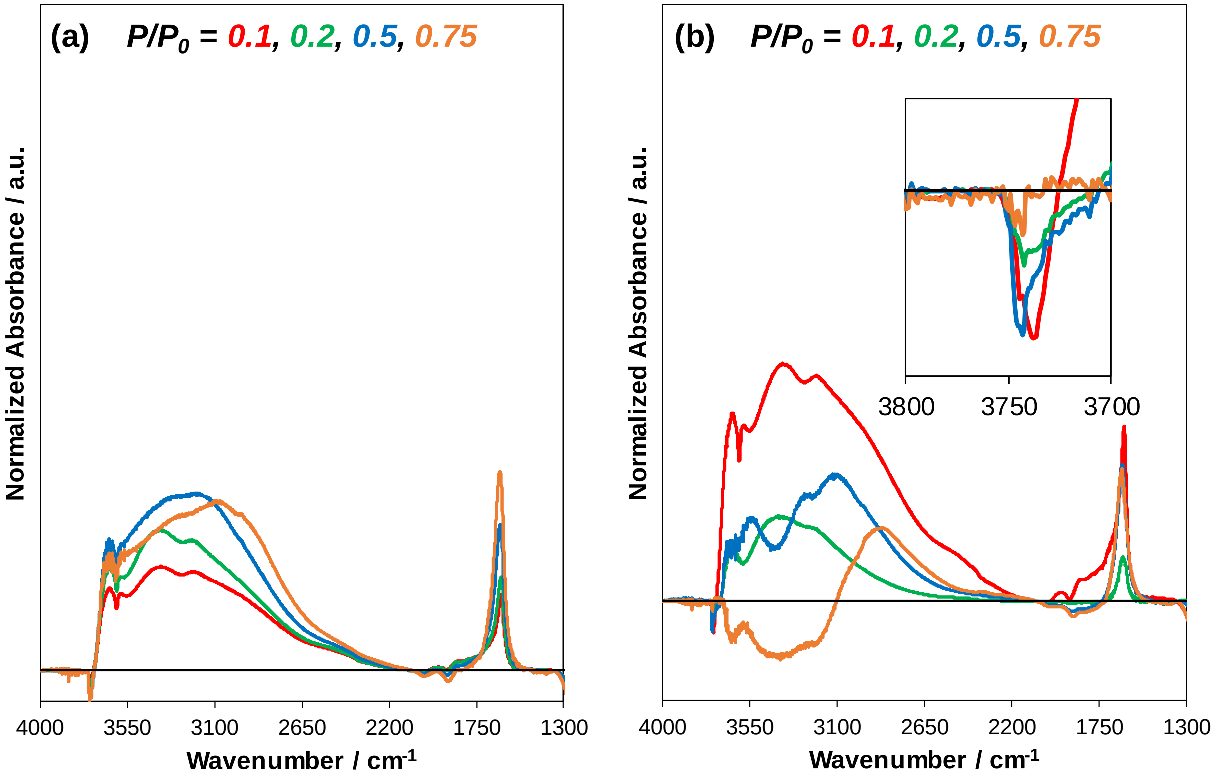

Figure S49. (a) Baseline-corrected difference IR spectra of H_2O adsorbed at 293 K on H-Al-Beta-F(1.4) at P/P_0 values of 0.1 (red), 0.2 (green), 0.5 (blue), and 0.75 (orange). Difference spectra reflect the subtraction of the spectrum of the dehydrated sample under flowing He prior to H_2O adsorption, and the spectrum of H_2O adsorbed within an empty IR cell. (b) Differential-subtracted spectra reflect the difference between the spectrum at the given P/P_0 value and the next-lowest P/P_0 value. All spectra are normalized to the T–O–T overtone peak area (1750–2100 cm^{-1}) prior to adsorption.

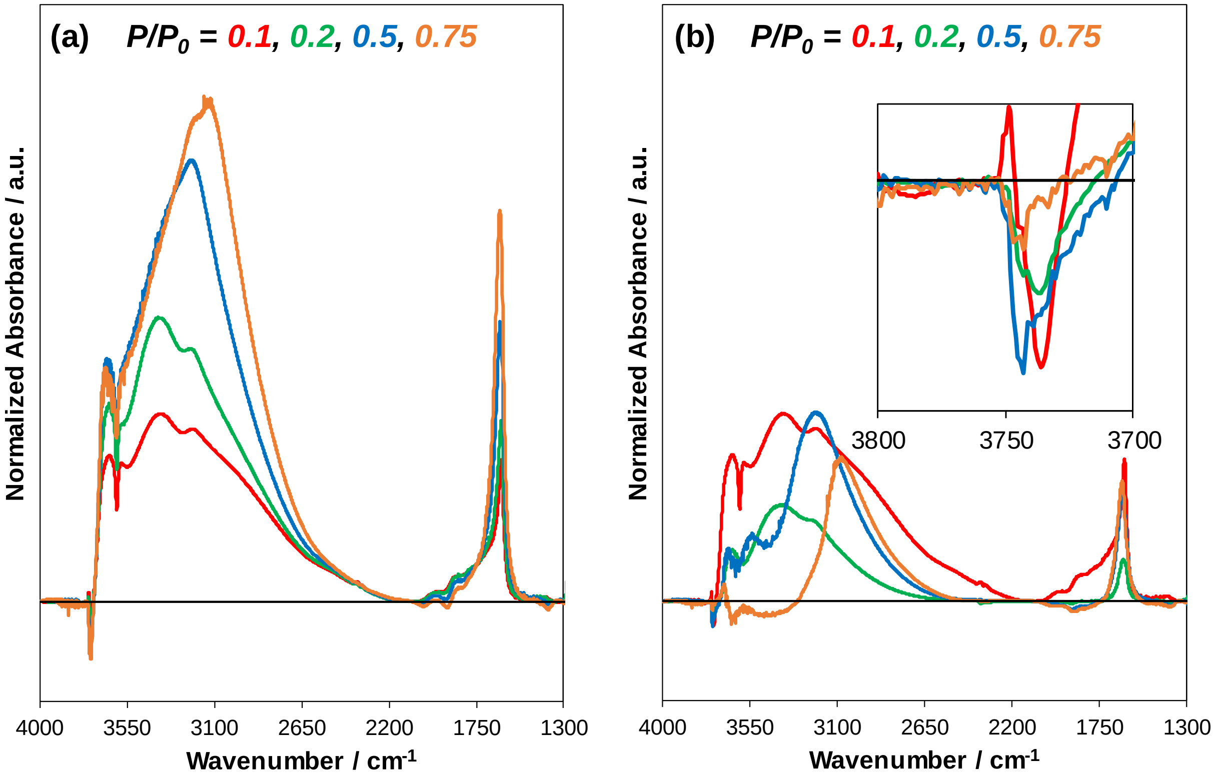

Figure S50. (a) Baseline-corrected difference IR spectra of H_2O adsorbed at 293 K on H-Al-Beta-F(1.2) at P/P_0 values of 0.1 (red), 0.2 (green), 0.5 (blue), and 0.75 (orange). Difference spectra reflect the subtraction of the spectrum of the dehydrated sample under flowing He prior to H_2O adsorption, and the spectrum of H_2O adsorbed within an empty IR cell. (b) Differential-subtracted spectra reflect the difference between the spectrum at the given P/P_0 value and the next-lowest P/P_0 value. All spectra are normalized to the T–O–T overtone peak area (1750–2100 cm^{-1}) prior to adsorption.

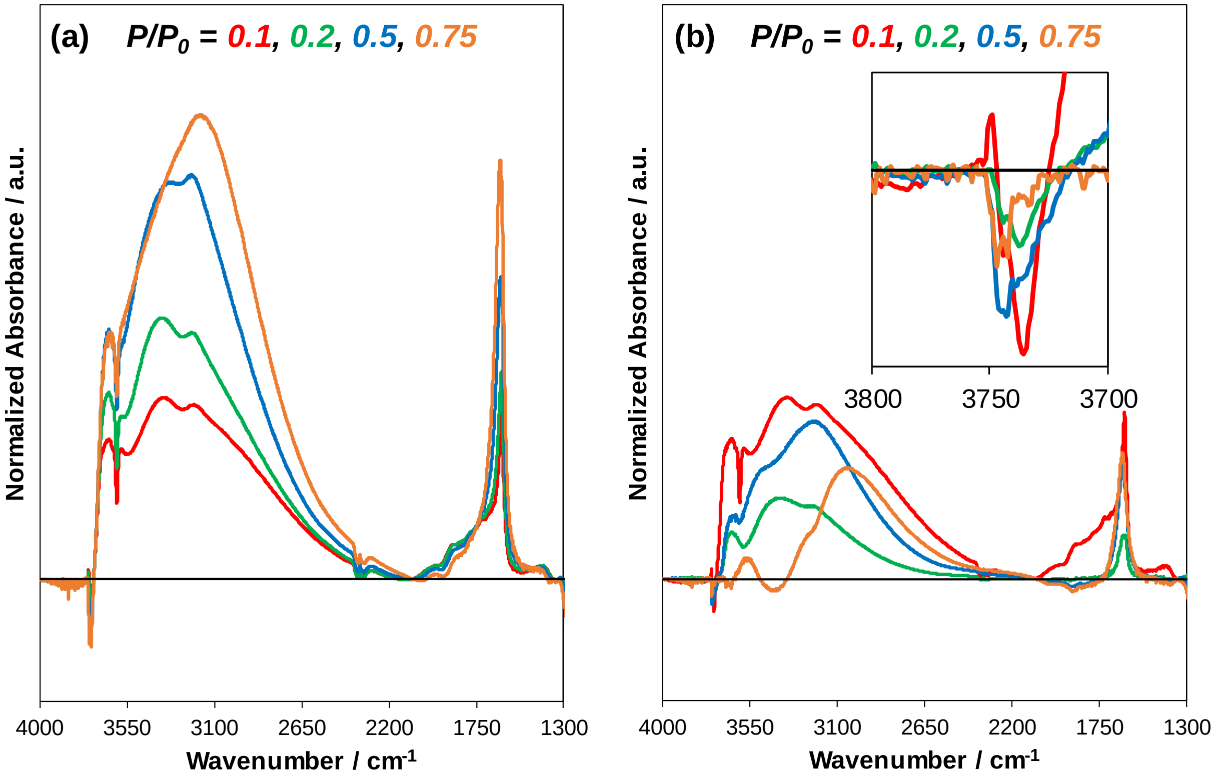

Figure S51. (a) Baseline-corrected difference IR spectra of H_2O adsorbed at 293 K on H-Al-Beta-F(0.78) at P/P_0 values of 0.1 (red), 0.2 (green), 0.5 (blue), and 0.75 (orange). Difference spectra reflect the subtraction of the spectrum of the dehydrated sample under flowing He prior to H_2O adsorption, and the spectrum of H_2O adsorbed within an empty IR cell. (b) Differential-subtracted spectra reflect the difference between the spectrum at the given P/P_0 value and the next-lowest P/P_0 value. All spectra are normalized to the T–O–T overtone peak area (1750–2100 cm^{-1}) prior to adsorption.

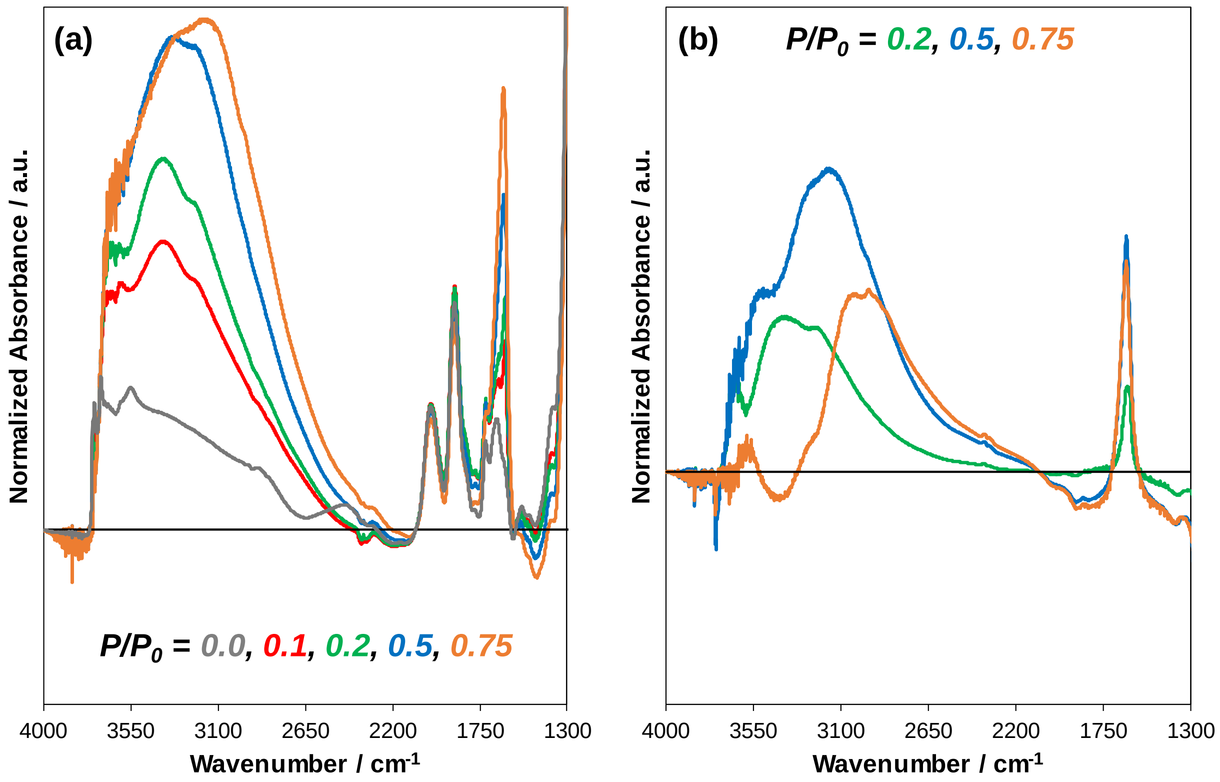

Figure S52. (a) Baseline-corrected IR spectra of H_2O adsorbed at 293 K on H-Al-Beta-F(0.57) at P/P_0 values of 0.1 (red), 0.2 (green), 0.5 (blue), and 0.75 (orange). A small leak in the system led to H_2O entering the system during cooling to 293 K, and adsorbing at some of the H^+ in 1:1 hydrogen-bonded complexes, evident in the A, B, C triplet seen in the grey spectrum, so difference spectra were not analyzed. (b) Differential-subtracted spectra reflect the difference between the spectrum at the given P/P_0 value and the next-lowest P/P_0 value. All spectra are normalized to the T–O–T overtone peak area (1750–2100 cm^{-1}) prior to adsorption.

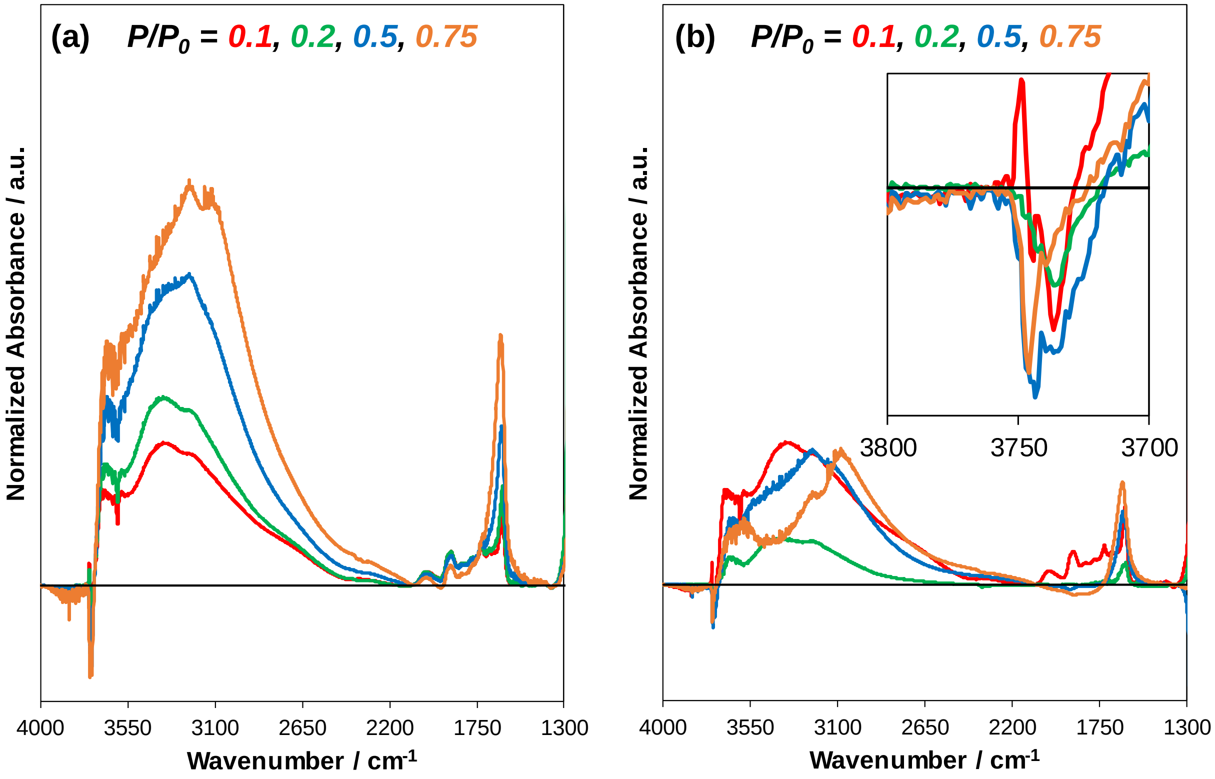

Figure S53. (a) Baseline-corrected difference IR spectra of H_2O adsorbed at 293 K on H-Al-Beta-F(0.16) at P/P_0 values of 0.1 (red), 0.2 (green), 0.5 (blue), and 0.75 (orange). Difference spectra reflect the subtraction of the spectrum of the dehydrated sample under flowing He prior to H_2O adsorption, and the spectrum of H_2O adsorbed within an empty IR cell. (b) Differential-subtracted spectra reflect the difference between the spectrum at the given P/P_0 value and the next-lowest P/P_0 value. All spectra are normalized to the T–O–T overtone peak area (1750–2100 cm^{-1}) prior to adsorption.

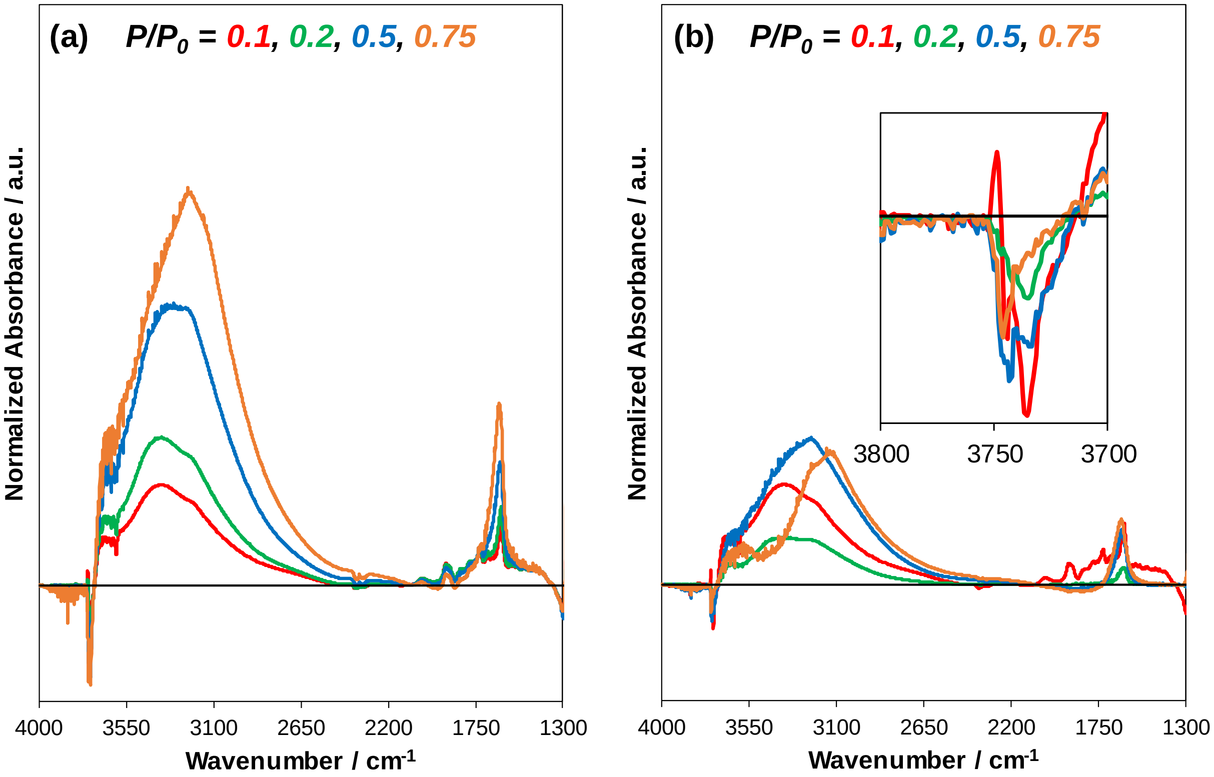

Figure S54. (a) Baseline-corrected difference IR spectra of H_2O adsorbed at 293 K on H-Al-Beta-F(0.11) at P/P_0 values of 0.1 (red), 0.2 (green), 0.5 (blue), and 0.75 (orange). Difference spectra reflect the subtraction of the spectrum of the dehydrated sample under flowing He prior to H_2O adsorption, and the spectrum of H_2O adsorbed within an empty IR cell. (b) Differential-subtracted spectra reflect the difference between the spectrum at the given P/P_0 value and the next-lowest P/P_0 value. All spectra are normalized to the T–O–T overtone peak area (1750–2100 cm^{-1}) prior to adsorption.

S.3.7. Infrared spectra of D_2O/HOD/H_2O mixtures

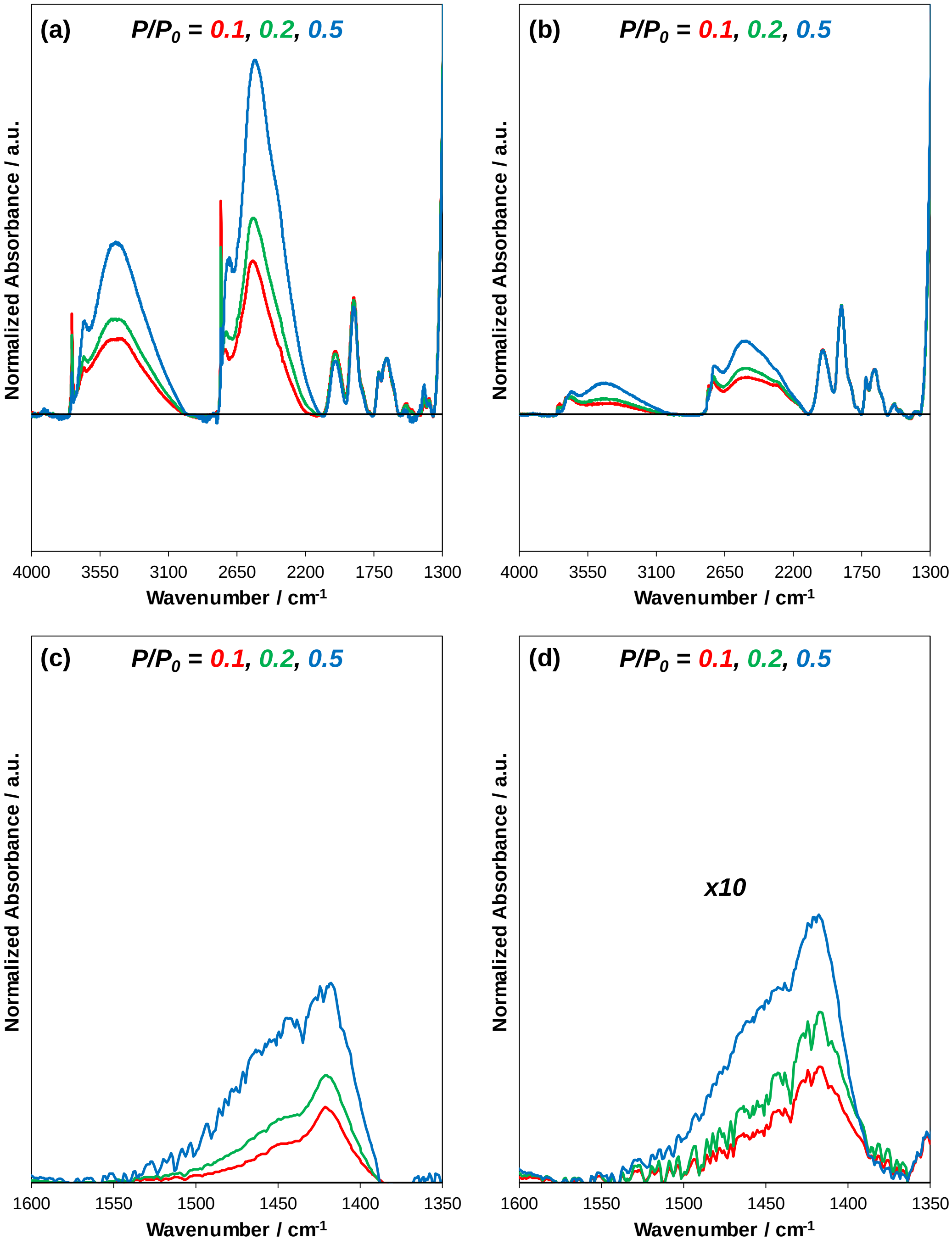

Figure S55. Baseline-corrected, gas-phase-corrected IR spectra of 16:8:1 D_2O:HOD:H_2O mixtures adsorbed at 303 K on (a) deAl-Beta-F(2.0) and (b) Si-Beta-F, at P/P_0 values of 0.1 (red), 0.2 (green), and 0.5 (blue). All spectra are normalized to the T–O–T overtone peak area (1750–2100 cm^{-1}) prior to adsorption. (c) and (d) show subtracted IR spectra of the δ(HOD) peaks under the same conditions described for (a), (b) on (c) deAl-Beta-F(2.0) and (d) Si-Beta-F.

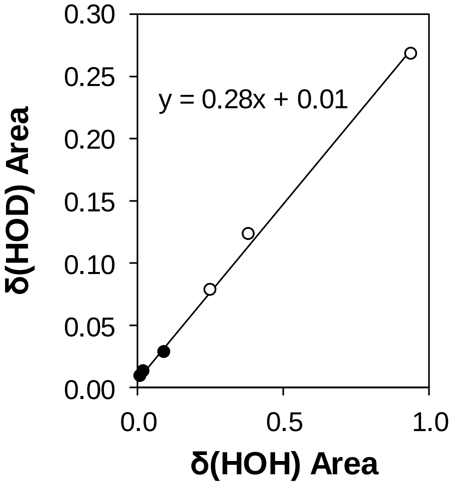

Figure S56. δ(HOD) peak areas quantified from Figure S55c,d correlated with the δ(HOH) peak areas quantified from Figure S40 and Figure S41 on Si-Beta-F (●) and deAl-Beta-F(2.0) (○) at the same P/P_0 conditions (0.1, 0.2, 0.5).

The correlation of peak areas in Figure S56 with a regressed slope of 0.28 that closely matches the mole fraction of HOD in the 16:8:1 D_2O:HOD:H_2O stream (0.32) indicates that coverages and extents of hydrogen bonding between $H(D)_2O$ molecules are the same between pure H_2O and the mixture experiments. Note that the δ(HOH) peak area was too small to quantify because of the low mole fraction of H_2O in the mixture (0.04), and the δ(DOD) peak at 1210 cm^{-1} could not be detected because it is obscured by the Si-O-Si modes of the zeolite framework (<1300 cm^{-1}). At the same coverage values where in the pure-H_2O experiment the ν(OH) peak center shifted to low wavenumbers with increasing coverages, when 96% of the mixture is D_2O or HOD there is no shift in the ν(OH) peak center, because 2δ(HOD) (2900 cm^{-1}) and 2δ(DOD) (2400 cm^{-1}) do not generate Fermi resonance with ν(OH) when in extended hydrogen-bonded networks, because they lie at lower wavenumbers.[47]

S.3.8. Infrared spectra collected at 373 K

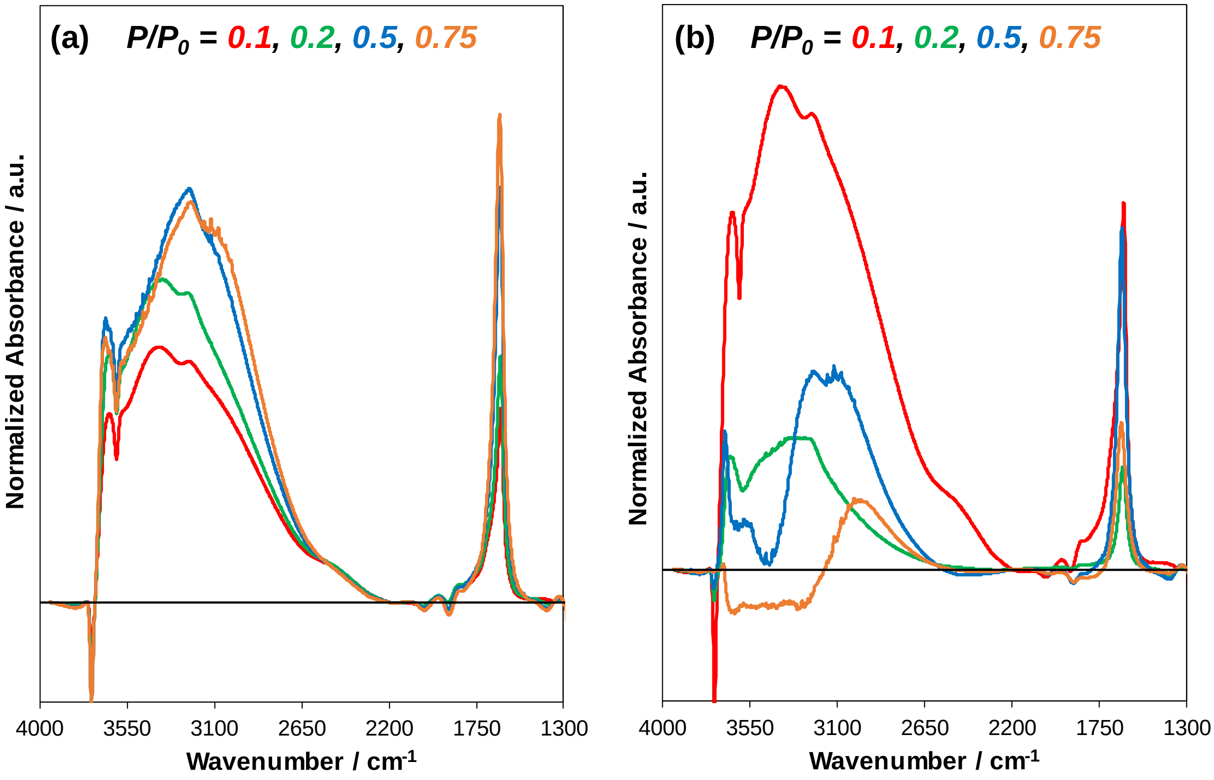

Figure S57. (a) Baseline-corrected difference IR spectra of H_2O adsorbed at 373 K on H-Al-Beta-F(2.0) at H_2O pressures of 10 (red), 20 (green), 30 (blue), and 75 kPa (orange) (P/P_0 = 0.1–0.75). Difference spectra reflect the subtraction of the spectrum of the dehydrated sample under flowing He prior to H_2O adsorption, and the spectrum of H_2O adsorbed within an empty IR cell. (b) Differential-subtracted spectra reflect the difference between the spectrum at the given P/P_0 value and the next-lowest P/P_0 value. All spectra are normalized to the T–O–T overtone peak area (1750–2100 cm^{-1}) prior to adsorption.

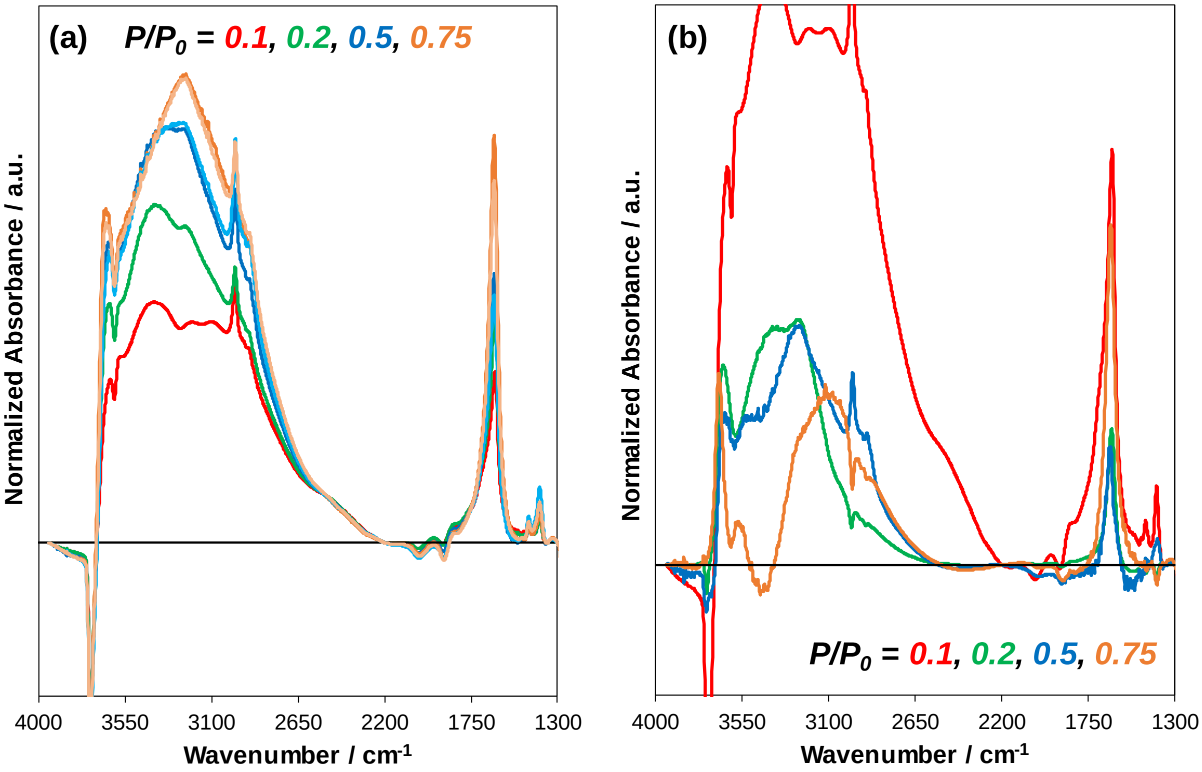

Figure S58. (a) Baseline-corrected difference IR spectra of H_2O/C_2H_5OH mixtures adsorbed at 373 K on H-Al-Beta-F(2.0) at H_2O pressures of 10 (red), 20 (green), 30 (blue), and 75 kPa (orange) (P/P_0 = 0.1–0.75). The colors shown in the legend correspond to C_2H_5OH/H_2O ratios of 0.005 (red, green) and 0.03 (blue, orange), and the lighter blue and orange spectra correspond to a C_2H_5OH/H_2O ratio of 0.06. Difference spectra reflect the subtraction of the spectrum of the dehydrated sample under flowing He prior to H_2O adsorption, and the spectrum of H_2O adsorbed within an empty IR cell. (b) Differential-subtracted spectra reflect the difference between the spectrum at the given P/P_0 value and the next-lowest P/P_0 value. All spectra are normalized to the T–O–T overtone peak area (1750–2100 cm^{-1}) prior to adsorption.

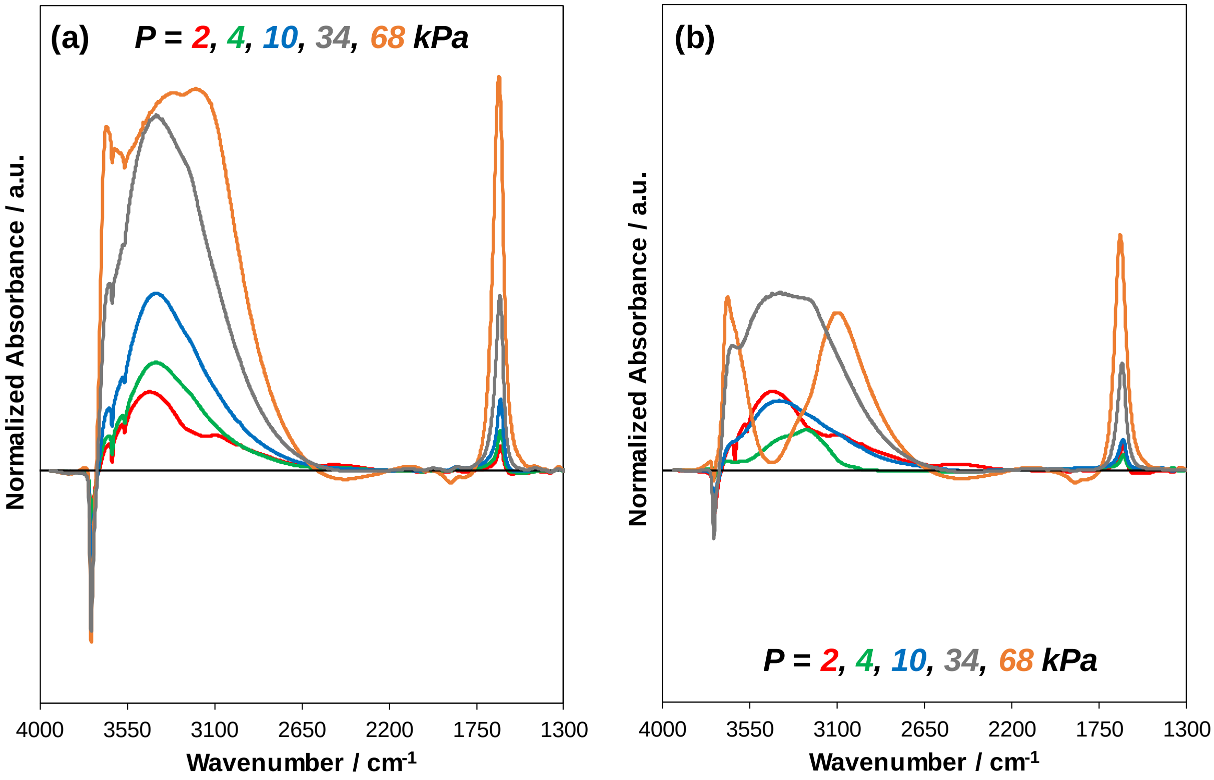

Figure S59. (a) Baseline-corrected difference IR spectra of H_2O adsorbed at 373 K on H-Al-FAU at H_2O pressures of 2 (red), 4 (green), 10 (blue), 34 (grey), and 68 kPa (orange) ($P/P_0 = 0.02–0.75$). Difference spectra reflect the subtraction of the spectrum of the dehydrated sample under flowing He prior to H_2O adsorption, and the spectrum of H_2O adsorbed within an empty IR cell. (b) Differential-subtracted spectra reflect the difference between the spectrum at the given P/P_0 value and the next-lowest P/P_0 value. All spectra are normalized to the T–O–T overtone peak area (1750–2100 cm^{-1}) prior to adsorption.

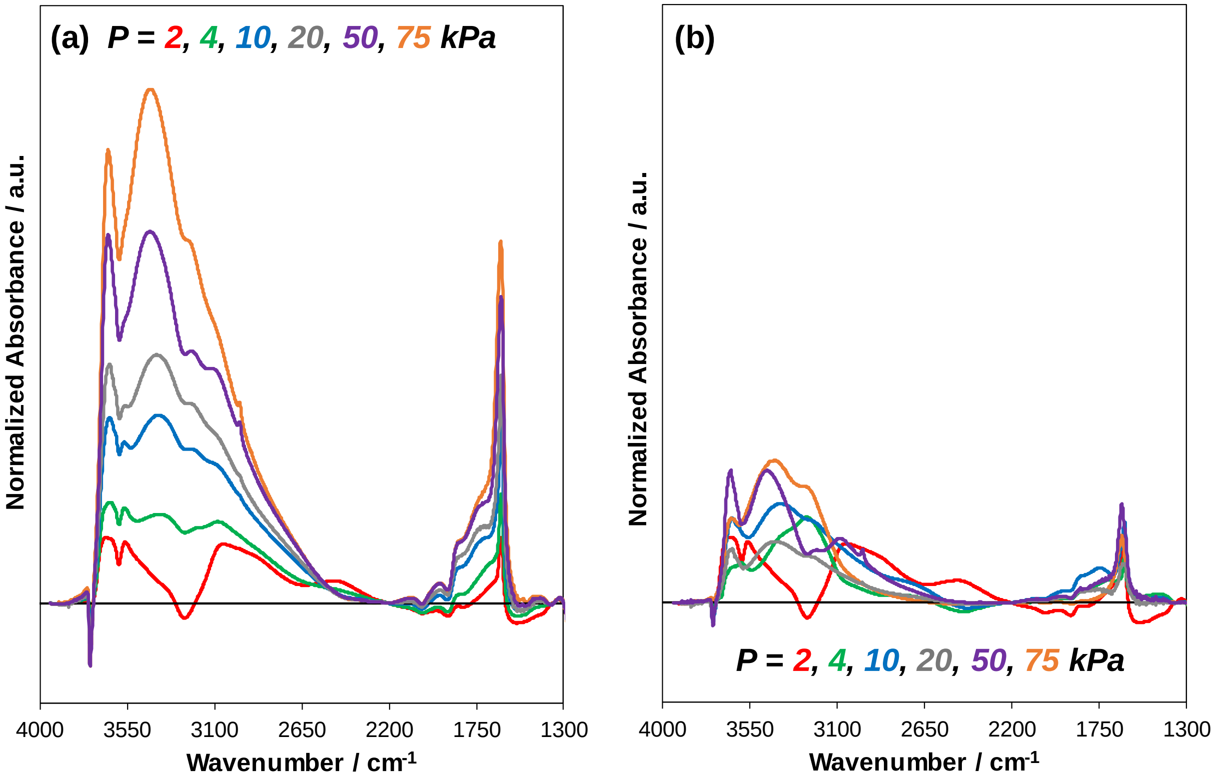

Figure S60. (a) Baseline-corrected difference IR spectra of H_2O adsorbed at 373 K on H-Al-TON at H_2O pressures of 2 (red), 4 (green), 10 (blue), 20 (grey), 50 (purple) and 75 kPa (orange) (P/P_0 = 0.02–0.75). Difference spectra reflect the subtraction of the spectrum of the dehydrated sample under flowing He prior to H_2O adsorption, and the spectrum of H_2O adsorbed within an empty IR cell. (b) Differential-subtracted spectra reflect the difference between the spectrum at the given P/P_0 value and the next-lowest P/P_0 value. All spectra are normalized to the T–O–T overtone peak area (1750–2100 cm^{-1}) prior to adsorption.

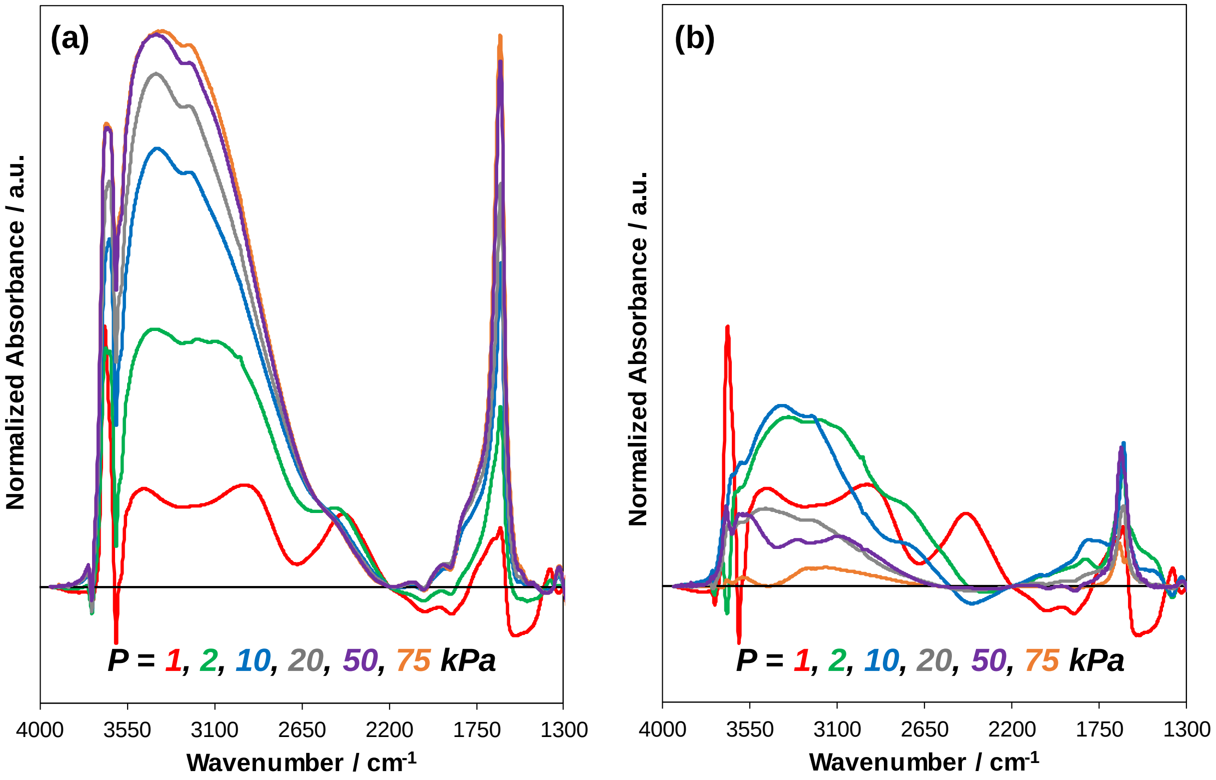

Figure S61. (a) Baseline-corrected difference IR spectra of H_2O adsorbed at 373 K on H-Al-AEI at H_2O pressures of 1 (red), 2 (green), 10 (blue), 20 (grey), 50 (purple) and 75 kPa (orange) (P/P_0 = 0.02–0.75). Difference spectra reflect the subtraction of the spectrum of the dehydrated sample under flowing He prior to H_2O adsorption, and the spectrum of H_2O adsorbed within an empty IR cell. (b) Differential-subtracted spectra reflect the difference between the spectrum at the given P/P_0 value and the next-lowest P/P_0 value. All spectra are normalized to the T–O–T overtone peak area (1750–2100 cm^{-1}) prior to adsorption.

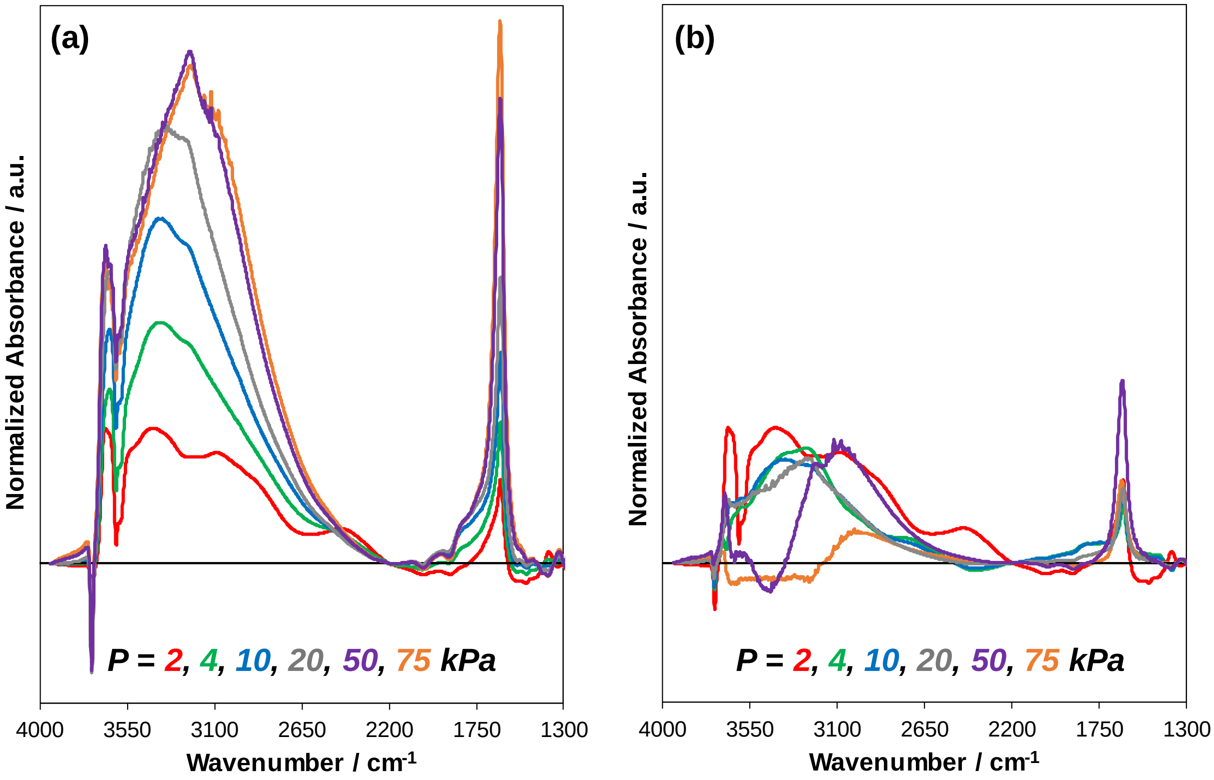

Figure S62. (a) Baseline-corrected difference IR spectra of H_2O adsorbed at 373 K on H-Al-CHA at H_2O pressures of 2 (red), 4 (green), 10 (blue), 20 (grey), 50 (purple) and 75 kPa (orange) (P/P_0 = 0.02–0.75). Difference spectra reflect the subtraction of the spectrum of the dehydrated sample under flowing He prior to H_2O adsorption, and the spectrum of H_2O adsorbed within an empty IR cell. (b) Differential-subtracted spectra reflect the difference between the spectrum at the given P/P_0 value and the next-lowest P/P_0 value. All spectra are normalized to the T–O–T overtone peak area (1750–2100 cm^{-1}) prior to adsorption.

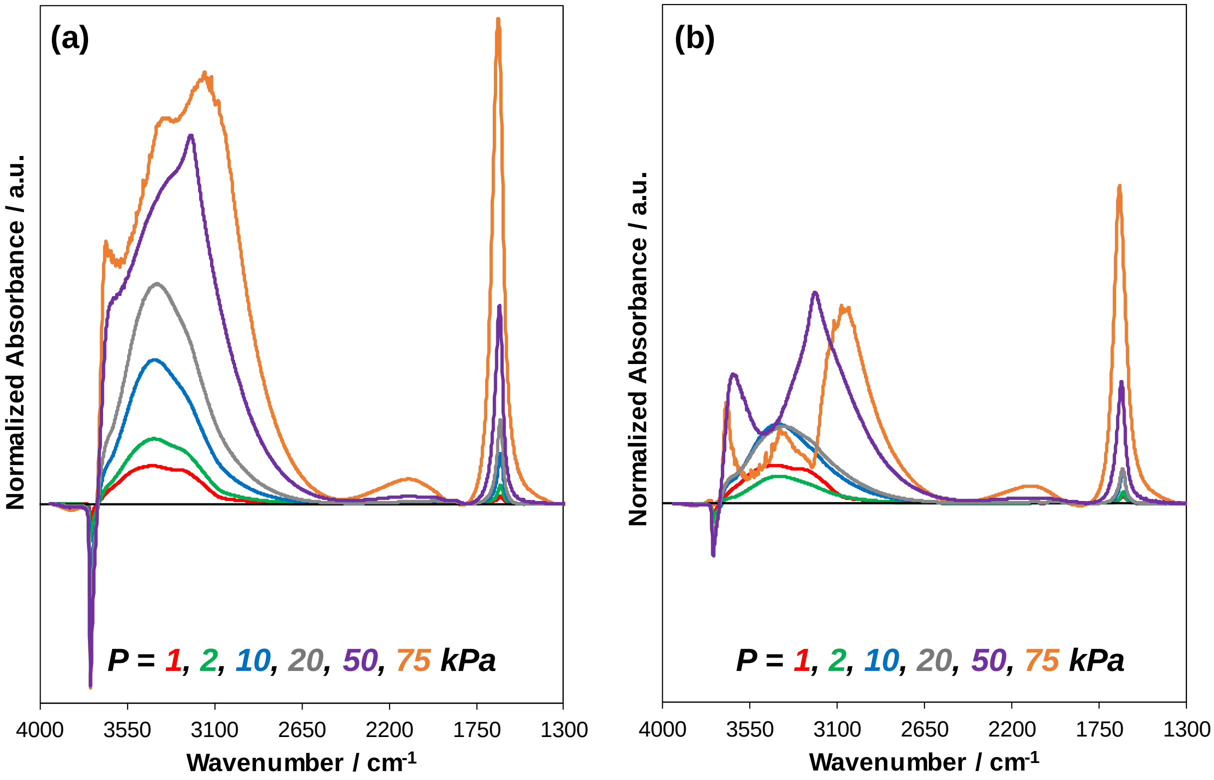

Figure S63. (a) Baseline-corrected difference IR spectra of H_2O adsorbed at 373 K on HPW/Si-MCM-41 at H_2O pressures of 1 (red), 2 (green), 10 (blue), 20 (grey), 50 (purple) and 75 kPa (orange) (P/P_0 = 0.02–0.75). Difference spectra reflect the subtraction of the spectrum of the dehydrated sample under flowing He prior to H_2O adsorption, and the spectrum of H_2O adsorbed within an empty IR cell. (b) Differential-subtracted spectra reflect the difference between the spectrum at the given P/P_0 value and the next-lowest P/P_0 value. All spectra are normalized to the T–O–T overtone peak area (1750–2100 cm^{-1}) prior to adsorption.

S.3.9. Theoretical calculations

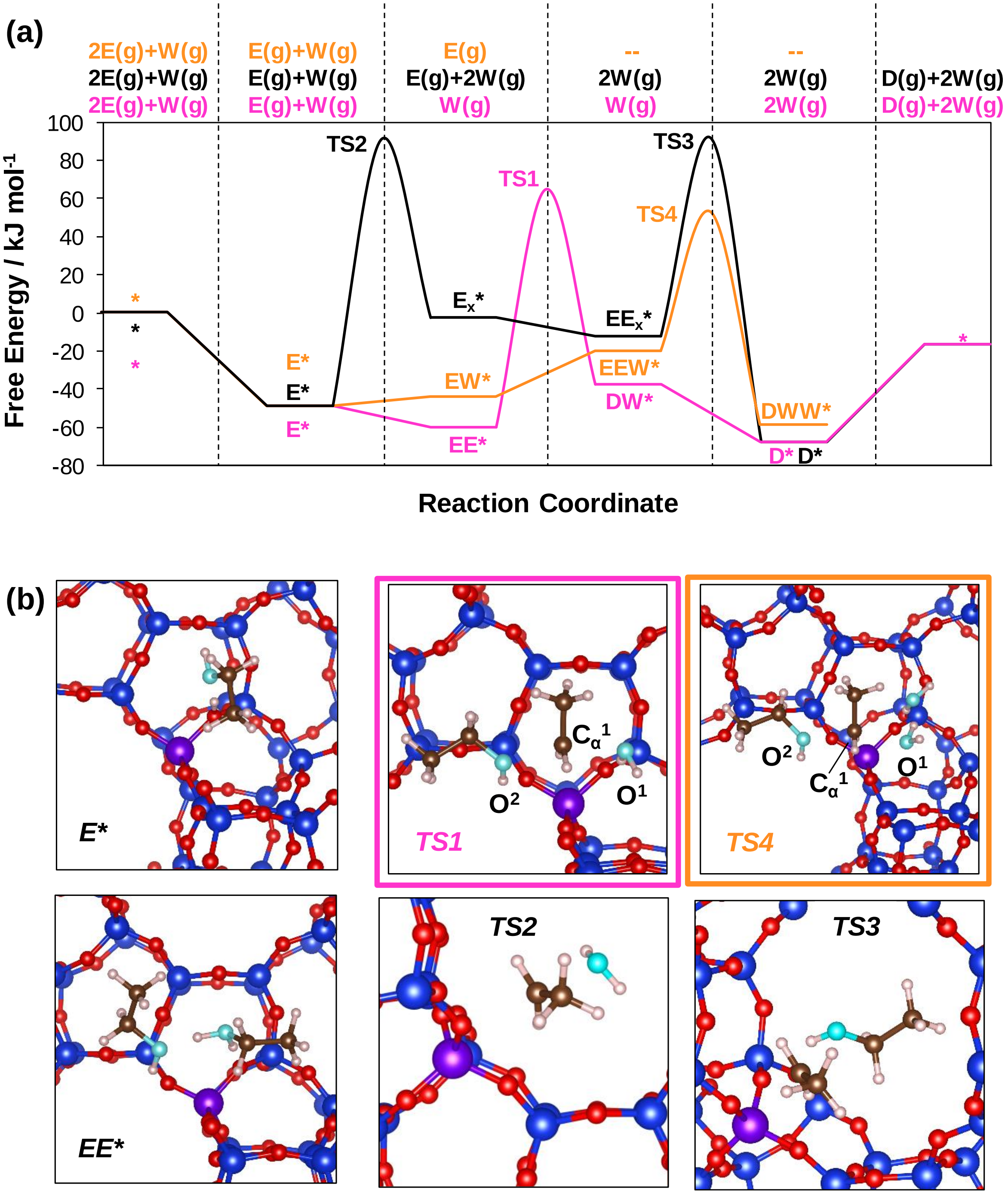

Figure S64. (a) Gibbs free energies (373 K) of adsorbed intermediates and transition states within H-Al-Beta calculated by DFT, referenced to two gas-phase ethanol molecules and one water molecule, for diethyl ether formation through the dissociative pathway (black), the associative pathway (pink), and the associative pathway with one co-adsorbed H_2O molecule (orange). (b) Geometries of adsorbed intermediates and transition states.

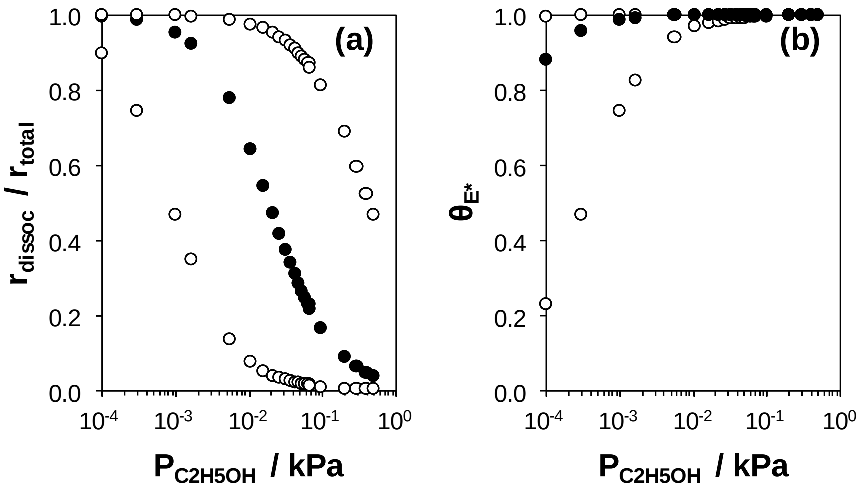

Figure S65. (a) Relative rates of dissociative and associative pathways to form diethyl ether (373 K) in the absence of co-fed water as a function of ethanol pressure on H-Al-Beta zeolites predicted from their DFT-calculated free energy barriers (Eq. (S9)), plotted as the fraction of the total rate ($r_{total} = r_{dissoc} + r_{assoc}$). (b) Predicted coverage of ethanol monomers at H^+ in H-Al-Beta at 373 K as a function of ethanol pressure, based on the DFT-calculated adsorption free energy (Eq. (S10)–(S11)). In both plots, the range of possible values introduced by a ±10 kJ mol^{-1} error in free energies is shown as the unfilled circles.

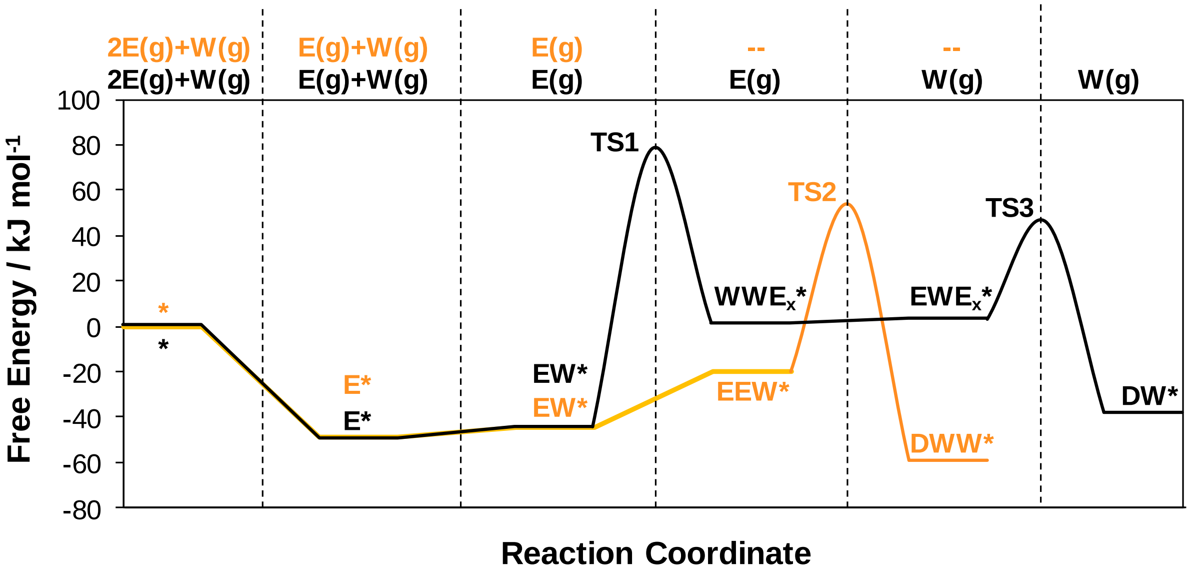

Figure S66. Gibbs free energies (373 K) of adsorbed intermediates and transition states within H-Al-Beta calculated by DFT, referenced to two gas-phase ethanol molecules and one water molecule, for diethyl ether formation through the dissociative pathway with one co-adsorbed H_2O molecule (black) and the associative pathway with one co-adsorbed H_2O molecule (orange).

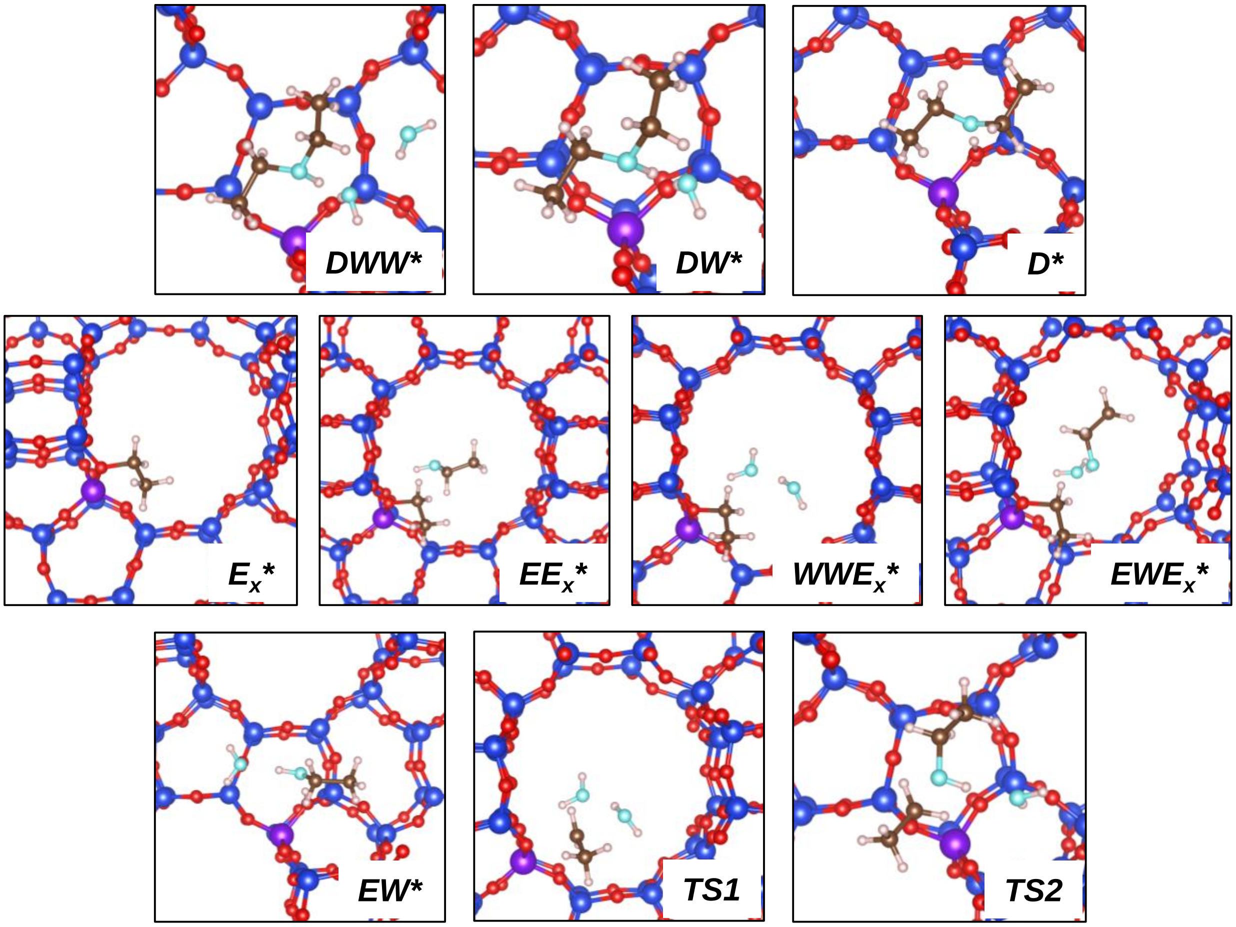

Figure S67. Additional reactive intermediates and transition states not included in Figure S64 and Figure S66. Similar to Figure S64, the Al atom is colored purple, oxygen atoms belonging to ethanol, water, or DEE are colored teal, framework oxygens are red, and framework silicon are blue. Hydrogen atoms and protons are colored white.

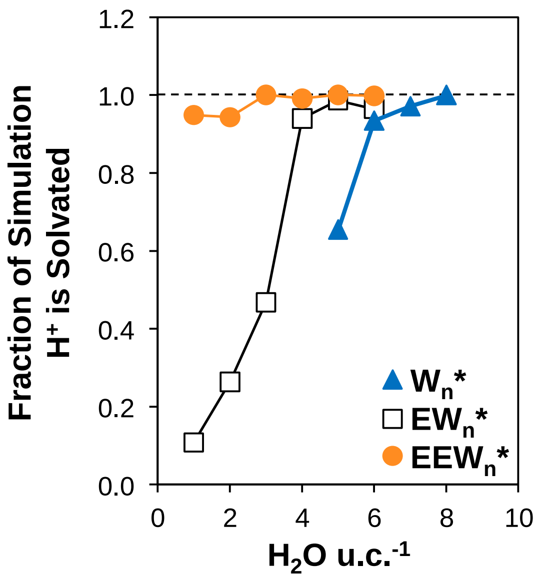

Figure S68. Probability that the acid site proton is solvated in either a pure water cluster (W_n*), ethanol monomer cluster (EW_n*), or ethanol dimer cluster (EEW_n*)

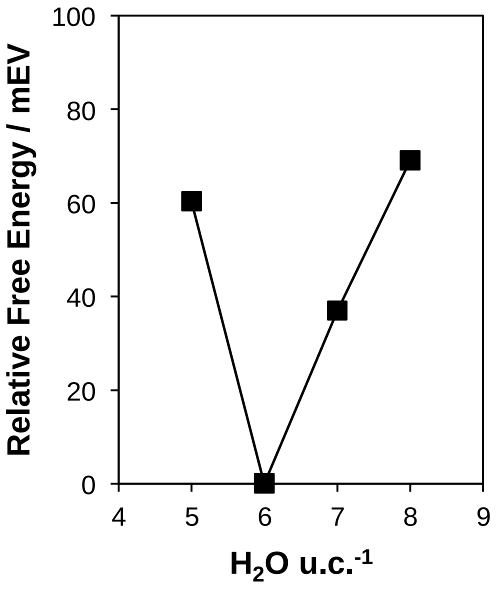

Figure S69. Free energy of water clusters (relative to W_6*) for different water loadings.

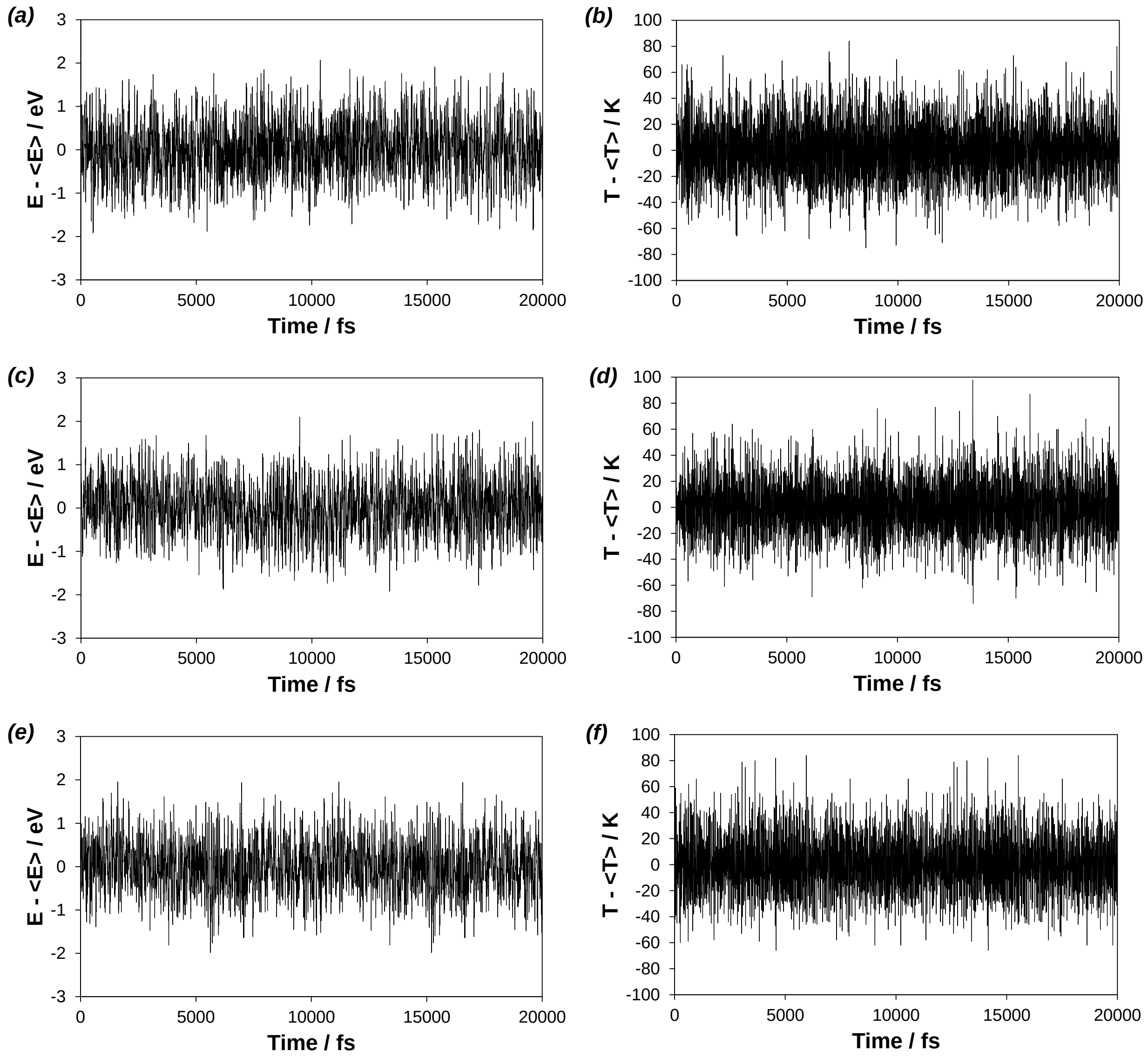

Figure S70. Characteristic fluctuations in total energy and temperature for ethanol dimer clusters (EEW_3*) (a-b), ethanol monomer clusters (EW_5*) (c-d), and pure water clusters (W_6*) (e-f).

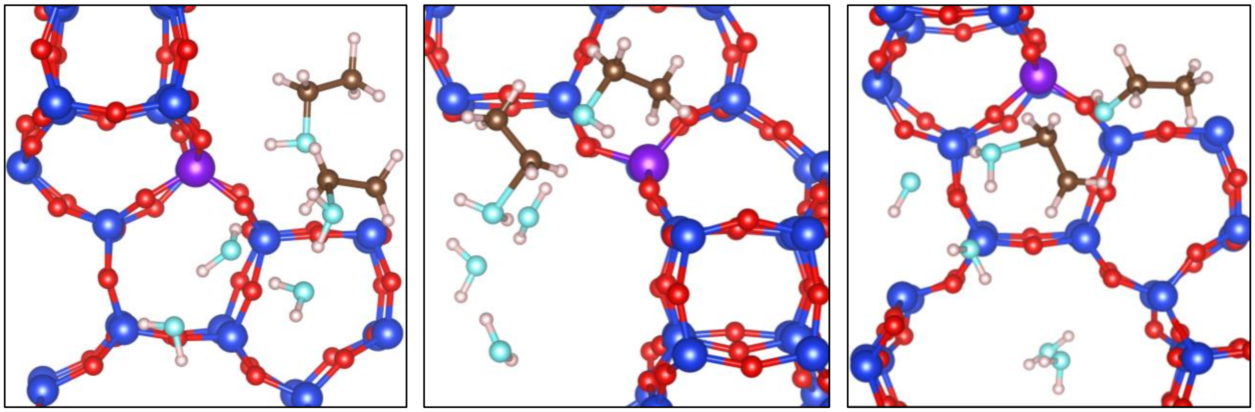

Figure S71. Additional views of the DEE formation transition state with 5 clustered H_2O molecules calculated with constrained AIMD at the saddle point identified with metadynamics indicated by reaction coordinate position (2) in Figure 6(b) of the Main Text. Each image is from a different timestep of the AIMD simulation depicting alkoxy groups that remain at the periphery of water clusters at the transition state.

S.4. Supplementary Tables

Table S1. Ethanol dehydration rate and equilibrium constants on H-Al-Beta zeolites quantified in the absence of co-fed water at 373 K.

Sample	**k_3 / 10^{-5} mol (mol H^+)$^{-1}$ s^{-1}**	**K_2 / kPa^{-1}**
H-Al-Beta-F(2.0)	2.5	84
H-Al-Beta-F(1.2)	1.9	51
H-Al-Beta-OH(1.7)	2.9	110

Table S2. Ethanol dehydration rate and equilibrium constants on H-Al-Beta zeolites quantified at 373 K in the water pressure regime described by Eq. (6) in the main text (~0.02–10 kPa).

Sample	**k_3K_2 / 10^{-4a}**	**$k_3K_2K_4^{-1}$ / 10^{-4b}**	**k_3K_2 / $10^{-4a,c}$ (no co-fed H_2O)**
H-Al-Beta-F(2.0)	5.2	1.5	21
H-Al-Beta-F(1.2)	3.8	1.5	9.5
H-Al-Beta-OH(1.7)	19	1.7	33

[a]units [=] mol (mol H^+)$^{-1}$ s^{-1} kPa^{-1} [b]units [=] mol (mol H^+)$^{-1}$ s^{-1} [c]quantified without co-fed H_2O (Table S1)

Table S3. Ethanol dehydration rate and equilibrium constants on H-Al-Beta-F(1.2) quantified in the water pressure regime described by Eq. (6) in the main text.

Temperature / K	**k_3K_2 / 10^{-4a}**	**$k_3K_2K_4^{-1}$ / 10^{-4b}**	**K_4 / kPa^{-1}**
373	3.8	1.5	2.5
423	43	120	0.35

[a]units [=] mol (mol H^+)$^{-1}$ s^{-1} kPa^{-1} [b]units [=] mol (mol H^+)$^{-1}$ s^{-1}

Table S4. Data used to estimate H_2O/H^+ on H-Al-Beta-F zeolites from volumetric adsorption isotherms at $P/P_0=0.2$.

Sample	**mmol g^{-1} H_2O**	**H_2O u.c.$^{-1}$**	**Si-Beta-F correction**[b]	**H_2O/H^{+b}**
Si-Beta-F	0.087	0.34	--	--
H-Al-Beta-F(0.11)	0.31	1.2	28%	7.9
H-Al-Beta-F(0.16)	0.46	1.8	19%	9.0
H-Al-Beta-F(0.57)	1.0	3.9	9%	6.2
H-Al-Beta-F(0.78)	1.4	5.2	6%	6.2
H-Al-Beta-F(1.2)	2.2	8.4	4%	6.8
H-Al-Beta-F(1.4)	2.9	11	3%	7.5
H-Al-Beta-F(2.0)	4.1	16	2%	7.0
Average	--	--	--	7 ± 1[c]

[a]Percentage of total adsorbed amount subtracted when correcting for Si-Beta-F adsorbed amount
[b]Corrected for Si-Beta mmol g^{-1} [c]Error represents 95% confidence interval of data set

Table S5. Data used to estimate H_2O/H^+ on H-Al-Beta-F zeolites from volumetric adsorption isotherms at $P/P_0=0.1$.

Sample	**mmol g^{-1} H_2O**	**H_2O u.c.$^{-1}$**	**Si-Beta-F correction**[b]	**H_2O/H^{+b}**
Si-Beta-F	0.051	0.19	--	--
H-Al-Beta-F(0.11)	0.22	0.83	23%	4.6
H-Al-Beta-F(0.16)	0.34	1.3	15%	6.1
H-Al-Beta-F(0.57)	0.76	2.9	7%	4.5
H-Al-Beta-F(0.78)	1.0	3.9	5%	4.6
H-Al-Beta-F(1.2)	1.6	6.2	3%	5.0
H-Al-Beta-F(1.4)	2.2	8.4	2%	5.5
H-Al-Beta-F(2.0)	3.1	12	2%	5.3
Average	--	--	--	5.1 ± 0.4[c]

[a]Percentage of total adsorbed amount subtracted when correcting for Si-Beta-F adsorbed amount
[b]Corrected for Si-Beta mmol g^{-1} [c]Error represents 95% confidence interval of data set

Table S6. Data used to estimate H_2O/(Si-OH nest) on deAl-Beta-F zeolites from volumetric adsorption isotherms at P/P_0=0.1.

Sample	**mmol g^{-1} H_2O**	**H_2O u.c.$^{-1}$**	**Si-Beta-F correction[b]**	**H_2O/nest[b]**
Si-Beta-F	0.044	0.17	--	--
deAl-Beta-F(0.11)	0.17	0.67	25%	4.6
deAl-Beta-F(0.16)	0.37	1.4	12%	8.0
deAl-Beta-F(0.78)	0.75	2.9	6%	3.5
deAl-Beta-F(1.2)	0.94	3.6	5%	2.9
deAl-Beta-F(1.4)	1.0	3.9	4%	2.6
deAl-Beta-F(2.0)	3.6	14	1%	6.3
Average	--	--	--	5 ± 2[c]

[a]Percentage of total adsorbed amount subtracted when correcting for Si-Beta-F adsorbed amount [b]Corrected for Si-Beta mmol g^{-1} [c]Error represents 95% confidence interval of data set

Table S7. Data used to estimate H_2O/(Si-OH nest) on deAl-Beta-F zeolites from volumetric adsorption isotherms at P/P_0=0.2.

Sample	**mmol g^{-1} H_2O**	**H_2O u.c.$^{-1}$**	**Si-Beta-F correction[b]**	**H_2O/nest[b]**
Si-Beta-F	0.087	0.34	--	--
deAl-Beta-F(0.11)	0.32	1.2	27%	9.8
deAl-Beta-F(0.16)	0.61	2.4	14%	14
deAl-Beta-F(0.78)	1.3	4.8	7%	6.0
deAl-Beta-F(1.2)	1.6	6.3	5%	5.2
deAl-Beta-F(1.4)	1.8	7.0	5%	4.7
deAl-Beta-F(2.0)	5.5	21	2%	9.5
Average	--	--	--	8 ± 3[c]

[a]Percentage of total adsorbed amount subtracted when correcting for Si-Beta-F adsorbed amount [b]Corrected for Si-Beta mmol g^{-1} [c]Error represents 95% confidence interval of data set

Table S8. H_2O coverages quantified by *in situ* IR at 373 K on H-Al-Beta-F(2.0), with and without co-fed C_2H_5OH.

P_{H2O} / kPa	N_{H2O}[a] / 10^{-3} mol g^{-1}	P_{C2H5OH} / kPa	N_{H2O}[b] / 10^{-3} mol g^{-1}	Ratio of H_2O coverages[c]
10	3.8	0.05	3.7	0.99
20	4.7	0.1	5.4	1.15
50	7.9	1.5	6.6	0.84
50	7.9	3	6.5	0.83
75	9.5	2.3	9.8	1.04
75	9.5	4.6	9.1	0.96

[a] Quantified from δ(HOH) peak area in IR spectra at the H_2O pressure specified in column 1. Error ± 0.3 × 10^{-3} mol g^{-1}

[b] Quantified from δ(HOH) peak area in IR spectra at the H_2O and C_2H_5OH pressures specified in columns 1 and 3. Error ± 0.3 × 10^{-3} mol g^{-1}

[c] Ratio of H_2O coverages with and without co-fed C_2H_5OH

Table S9. Binding energy of ethanol at different sites in H-Al-Beta[48]

T site index	proton location	Ethanol binding energy / eV
T0	C0	-0.98
	C1	-0.91
	C2	-0.86
	C3	-0.97
T1	C0	-0.97
	C1	-0.99
	C2	-0.88
	C3	-0.78
T2	C0	-0.91
	C1	-0.99
	C2	-0.91
	C3	-0.94
T3	C0	-0.91
	C1	-0.91
	C2	-0.96
	C3	-0.91
T4	C0	-0.96
	C1	-0.97
	C2	-0.95
	C3	-
T5	C0	-0.94
	C1	-0.99
	C2	-0.92
	C3	-
T6	C0	-
	C1	-0.91
	C2	-1.00
	C3	-
T7	C0	-0.85

	C1	-0.92
	C2	-0.80
	C3	-0.92
T8	C0	-0.90
	C1	-0.96
	C2	-1.00
	C3	-0.86

S.5. References

1 R. Bermejo-Deval, M. Orazov, R. Gounder, S.-J. Hwang and M. E. Davis, *ACS Catal.*, 2014, **4**, 2288–2297.
2 M. A. Camblor, A. Corma and S. Valencia, *J. Mater. Chem.*, 1998, **8**, 2137–2145.
3 C.-C. Chang, Z. Wang, P. Dornath, H. J. Cho and W. Fan, *RSC Adv.*, 2012, **2**, 10475–10477.
4 J. R. Di Iorio and R. Gounder, *Chem. Mater.*, 2016, **28**, 2236–2247.
5 J. D. Albarracin-Caballero, I. Khurana, J. R. D. Iorio, A. J. Shih, J. E. Schmidt, M. Dusselier, M. E. Davis, A. Yezerets, J. T. Miller, F. H. Ribeiro and R. Gounder, *React. Chem. Eng.*, 2017, **2**, 168–179.
6 J. R. Di Iorio, S. A. Bates, A. A. Verma, W. N. Delgass, F. H. Ribeiro, J. T. Miller and R. Gounder, *Top. Catal.*, 2015, **58**, 424–434.
7 M. J. Cordon, J. W. Harris, J. C. Vega-Vila, J. S. Bates, S. Kaur, M. Gupta, M. E. Witzke, E. C. Wegener, J. T. Miller, D. W. Flaherty, D. D. Hibbitts and R. Gounder, *J. Am. Chem. Soc.*, 2018, **140**, 14244–14266.
8 B. C. Bukowski, J. S. Bates, R. Gounder and J. Greeley, *Angew. Chem. Int. Ed.*, 2019, **58**, 16422–16426.
9 V. J. Cybulskis, J. W. Harris, Y. Zvinevich, F. H. Ribeiro and R. Gounder, *Rev. Sci. Instrum.*, 2016, **87**, 103101.
10 J. Wang, V. F. Kispersky, W. Nicholas Delgass and F. H. Ribeiro, *J. Catal.*, 2012, **289**, 171–178.
11 Ch. Baerlocher and L. B. McCusker, Database of Zeolite Structures, http://www.iza-structure.org/databases/, (accessed October 9, 2017).
12 S. Smidstrup, A. Pedersen, K. Stokbro and H. Jónsson, *J. Chem. Phys.*, 2014, **140**, 214106.
13 B. C. Bukowski, J. S. Bates, R. Gounder and J. Greeley, *J. Catal.*, 2018, **365**, 261–276.
14 M. DeLuca, P. Kravchenko, A. Hoffman and D. Hibbitts, *ACS Catal.*, 2019, **9**, 6444–6460.
15 W. Tang, E. Sanville and G. Henkelman, *J. Phys. Condens. Matter*, 2009, **21**, 084204.
16 H. Chiang and A. Bhan, *J. Catal.*, 2010, **271**, 251–261.
17 A. J. Jones, S. I. Zones and E. Iglesia, *J. Phys. Chem. C*, 2014, **118**, 17787–17800.
18 M. L. Sarazen, E. Doskocil and E. Iglesia, *J. Catal.*, 2016, **344**, 553–569.
19 G. Noh, Z. Shi, S. I. Zones and E. Iglesia, *J. Catal.*, 2018, **368**, 389–410.
20 Y. Zhi, H. Shi, L. Mu, Y. Liu, D. Mei, D. M. Camaioni and J. A. Lercher, *J. Am. Chem. Soc.*, 2015, **137**, 15781–15794.
21 R. J. Madon and M. Boudart, *Ind. Eng. Chem. Fundam.*, 1982, **21**, 438–447.
22 D. Mears, *Ind. Eng. Chem. Process Des. Dev.*, 1971, **10**, 541–547.
23 R. Krishna and J. M. van Baten, *Langmuir*, 2010, **26**, 10854–10867.
24 W. Knaeble and E. Iglesia, *J. Phys. Chem. C*, 2016, **120**, 3371–3389.
25 K. Alexopoulos, M.-S. Lee, Y. Liu, Y. Zhi, Y. Liu, M.-F. Reyniers, G. B. Marin, V.-A. Glezakou, R. Rousseau and J. A. Lercher, *J. Phys. Chem. C*, 2016, **120**, 7172–7182.
26 A. Zecchina, S. Bordiga, G. Spoto, D. Scarano, G. Spanò and F. Geobaldo, *J. Chem. Soc. Faraday Trans.*, 1996, **92**, 4863–4875.
27 G. Piccini and J. Sauer, *J. Chem. Theory Comput.*, 2014, **10**, 2479–2487.
28 G. Piccini, M. Alessio, J. Sauer, Y. Zhi, Y. Liu, R. Kolvenbach, A. Jentys and J. A. Lercher, *J. Phys. Chem. C*, 2015, **119**, 6128–6137.
29 J. S. Bates and R. Gounder, *J. Catal.*, 2018, **365**, 213–226.
30 E. Senderov, I. Halasz and D. H. Olson, *Microporous Mesoporous Mater.*, 2014, **186**, 94–100.

31 H. Koller, C. Schroeder, C. Mück-Lichtenfeld, L. Xu, N. A. Grosso-Giordano, A. Okrut, C.-Y. Chen, S. I. Zones, A. Katz and M. R. Hansen, *Angew. Chem.*, , DOI:10.1002/ange.202001364.
32 S. Brunauer, L. S. Deming, W. E. Deming and E. Teller, *J. Am. Chem. Soc.*, 1940, **62**, 1723–1732.
33 N. Giovambattista, P. G. Debenedetti and P. J. Rossky, *J. Phys. Chem. C*, 2007, **111**, 1323–1332.
34 B. Rotenberg, A. J. Patel and D. Chandler, *J. Am. Chem. Soc.*, 2011, **133**, 20521–20527.
35 J. I. Monroe and M. S. Shell, *Proc. Natl. Acad. Sci.*, 2018, **115**, 8093–8098.
36 A. M. Schrader, J. I. Monroe, R. Sheil, H. A. Dobbs, T. J. Keller, Y. Li, S. Jain, M. S. Shell, J. N. Israelachvili and S. Han, *Proc. Natl. Acad. Sci.*, 2018, 201722263.
37 S. Brunauer, *The Adsorption Of Gases And Vapors Vol I*, Oxford University Press., 1943.
38 H. Pan, J. A. Ritter and P. B. Balbuena, *Langmuir*, 1998, **14**, 6323–6327.
39 D. Wu, X. Guo, H. Sun and A. Navrotsky, *J. Phys. Chem. C*, 2015, **119**, 15428–15433.
40 J. W. Harris, M. J. Cordon, J. R. Di Iorio, J. C. Vega-Vila, F. H. Ribeiro and R. Gounder, *J. Catal.*, 2016, **335**, 141–154.
41 K. Zhang, R. P. Lively, J. D. Noel, M. E. Dose, B. A. McCool, R. R. Chance and W. J. Koros, *Langmuir*, 2012, **28**, 8664–8673.
42 V. Bolis, C. Busco and P. Ugliengo, *J. Phys. Chem. B*, 2006, **110**, 14849–14859.
43 S. Eckstein, P. H. Hintermeier, R. Zhao, E. Baráth, H. Shi, Y. Liu and J. A. Lercher, *Angew. Chem. Int. Ed.*, 2019, **58**, 3450–3455.
44 D. H. Olson, W. O. Haag and W. S. Borghard, *Microporous Mesoporous Mater.*, 2000, **35–36**, 435–446.
45 H.-J. Chun, V. Apaja, A. Clayborne, K. Honkala and J. Greeley, *ACS Catal.*, 2017, **7**, 3869–3882.
46 D. T. Bregante, A. M. Johnson, A. Y. Patel, E. Z. Ayla, M. J. Cordon, B. C. Bukowski, J. Greeley, R. Gounder and D. W. Flaherty, *J. Am. Chem. Soc.*, 2019, **141**, 7302–7319.
47 M. Sovago, R. K. Campen, G. W. H. Wurpel, M. Müller, H. J. Bakker and M. Bonn, *Phys. Rev. Lett.*, , DOI:10.1103/PhysRevLett.100.173901.
48 G. Li, B. Wang and D. E. Resasco, *ACS Catal.*, 2020, **10**, 1294–1309.